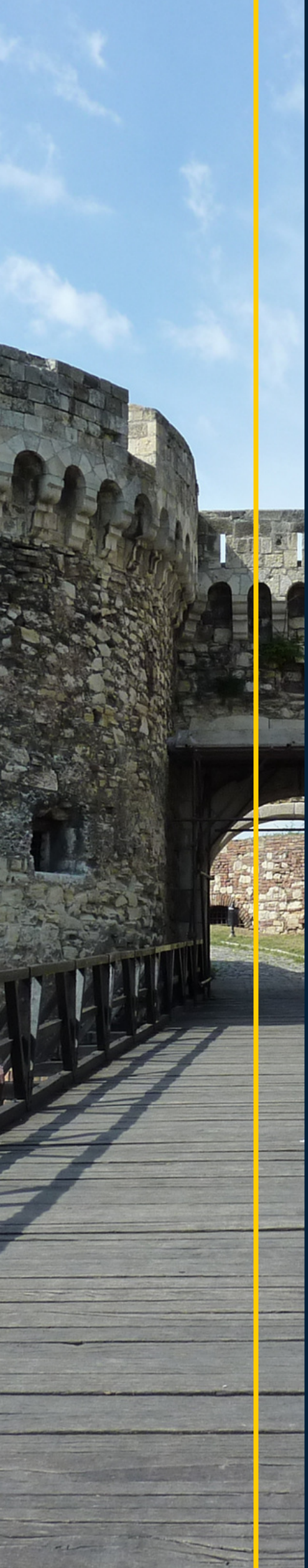

ICENS

6TH INTERNATIONAL CONFERENCE ON ENGINEERING AND NATURAL SCIENCES

BOOK OF PROCEEDINGS

www.icens.eu

October 21, 2020

Organized by

Partners

6th INTERNATIONAL CONFERENCE ON ENGINEERING AND NATURAL SCIENCES (ICENS)

ISBN 978-605-81426-1-9

ISSN 2687-2447

PROCEEDINGS OF THE 6th INTERNATIONAL CONFERENCE ON ENGINEERING AND NATURAL SCIENCES (ICENS) (ICENS 2020) OCTOBER 21 TO 25, 2020 BELGRADE, SERBIA.

Edited by

Prof. Dr. Özer Çınar

Published by:

info@icens.eu
www.icens.eu
www.cnrgroup.eu

CNR Group Laboratuvar ve Arge Hizmetleri Sanayi Ticaret Limited Şirketi Çifte Havuzlar Mah., Eski Londra Asfaltı Cad., Kuluçka Mrk., A1 Blok, 151/1C, Iç Kapı No:1 B-20, Esenler / Istanbul, 34220

ISBN 978-605-81426-1-9

ISSN 2687-2447

SCIENTIFIC COMMITTEE

1. Prof. Dr. Adisa Parić - University of Sarajevo - Bosnia and Herzegovina
2. Prof. Dr. Ahmet Doğan – Yıldız Technical University - Turkey
3. Prof. Dr. Aleksandar Dimitrov - Ss. Cyril and Methodius University - Macedonia
4. Prof. Dr. Alexander Golub - National University of Kyiv-Mohyla Academy - Ukraine
5. Prof. Dr. Alexander Litvinenko - National University of Food Technologies (Kyiv) - Ukraine
6. Prof. Dr. Anita Grozdanov - Ss. Cyril and Methodius University - Macedonia
7. Prof. Dr. Arslan Saral – Yıldız Technical University - Turkey
8. Prof. Dr. Asif Šabanović – International University of Sarajevo - Bosnia and Herzegovina
9. Prof. Dr. Bekir Erol Ak - Harran University - Turkey
10. Prof. Dr. Cem Şensöğüt - Dumlupınar University - Turkey
11. Prof. Dr. Christos Douligeris - University of Erlangen-Nurnberg - Germany
12. Prof. Dr. Dragutin T. Mihailović - University of Novi Sad - Serbia
13. Prof. Dr. Evgeniy Shtefan - National University of Food Technologies (Kyiv) - Ukraine
14. Prof. Dr. Falko Dressler - University of Paderborn - Germany
15. Prof. Dr. Harry Miller – International University of Sarajevo - Bosnia and Herzegovina
16. Prof. Dr. Houssam Toutanji – Western Michigan University - USA
17. Prof. Dr. Ian F. Akyıldız – Georgia Institute of Technology - USA
18. Prof. Dr. İsmail Usta - Marmara University - Turkey
19. Prof. Dr. Kateryna Derevska - National University of Kyiv-Mohyla Academy - Ukraine
20. Prof. Dr. Liljana Gavrilovska - Ss Cyril and Methodius University - Macedonia
21. Prof. Dr. Lukman Thalib - Qatar University - Qatar
22. Prof. Dr. M. Asghar Fazel – University of Environment - Iran
23. Prof. Dr. Mikhailov Volodymyr - Taras Shevchenko National University of Kyiv - Ukraine
24. Prof. Dr. Mykola Glybovets - National University of Kyiv-Mohyla Academy - Ukraine
25. Prof. Dr. Muammer Koç - Hamad bin Khalifa University - Qatar
26. Prof. Dr. Nadia Bilko - National University of Kyiv-Mohyla Academy - Ukraine
27. Prof. Dr. Özer Çınar – Yıldız Technical University - Turkey
28. Prof. Dr. Perica Paunovik - Ss. Cyril and Methodius University - Macedonia
29. Prof. Dr. Rifat Škrijelj – University of Sarajevo - Bosnia and Herzegovina
30. Prof. Dr. Samir Đug - University of Sarajevo - Bosnia and Herzegovina
31. Prof. Dr. Tanju Karanfil – Clemson University - USA
32. Prof. Dr. Ümit Alver – Karadeniz Technical University - Turkey
33. Prof. Dr. Wolfgang Gerstacker - University of Erlangen-Nurnberg - Germany
34. Prof. Dr. Vladyslav Sukhenko - National University of Life and Environmental Sciences of Ukraine (Kyiv) - Ukraine
35. Prof. Dr. Yılmaz Yıldırım - Bülent Ecevit University - Turkey
36. Prof. Dr. Yousef Haik - Hamad bin Khalifa University - Qatar
37. Assoc. Prof. Dr. Alaa Al Hawari - Qatar University - Qatar
38. Assoc. Prof. Dr. Fatih Ungan - Cumhuriyet University - Turkey
39. Assoc. Prof. Dr. Izudin Dzafic - International University of Sarajevo - Bosnia and Herzegovina
40. Assoc. Prof. Dr. Kateryna Syera - National University of Life and Environmental Sciences of Ukraine (Kyiv) - Ukraine
41. Assist. Prof. Dr. Muhamed Hadziabdic - International University of Sarajevo - Bosnia and Herzegovina
42. Assoc. Prof. Dr. Nusret Drešković - University of Sarajevo - Bosnia and Herzegovina
43. Assoc. Prof. Dr. Polina Vakuliuk - National University of Kyiv-Mohyla Academy - Ukraine
44. Assoc. Prof. Dr. Senija Tahirovic - International University of Sarajevo - Bosnia and Herzegovina
45. Assoc. Prof. Dr. Victor Karamushka - National University of Kyiv-Mohyla Academy - Ukraine
46. Assoc. Prof. Dr. Victoria Konovalova - National University of Kyiv-Mohyla Academy - Ukraine
47. Assoc. Prof. Dr. Yuriy Kravchenko - National University of Life and Environmental Sciences of Ukraine (Kyiv) - Ukraine
48. Assist. Prof. Dr. Fatih Taktak - Uşak University - Turkey
49. Assist. Prof. Dr. Fouzi Tabet - German Biomass Research Center - Germany
50. Assist. Prof. Dr. Haris Gavranovic - International University of Sarajevo - Bosnia and Herzegovina
51. Assist. Prof. Dr. Sasan Rabieh - Shahid Beheshti University - Iran
52. Assist. Prof. Dr. Ševkija Okerić - University of Sarajevo - Bosnia and Herzegovina
53. Assist. Prof. Dr. J. Amudhavel - VIT Bhopal University - India
54. Dr. Zsolt Hetesi - National University of Public Service, Budapest - Hungary
55. Dr. Zsolt T. Németh - National University of Public Service, Budapest - Hungary

ORGANIZATION COMMITTEE

Chairman of the Conference

Prof. Dr. Özer Çınar – Yıldız Technical University

Members of the Committee

Prof. Dr. Ümit Alver (Co-Chairman) - Karadeniz Technical University - Turkey
Prof. Dr. Mikhailov Volodymyr - Taras Shevchenko National University of Kyiv - Ukraine
Assoc. Prof. Dr. Kateryna Syera - National University of Life and Environmental Sciences of Ukraine (Kiev) - Ukraine
Assoc. Prof. Dr. Lukman Thalib - Qatar University - Qatar
Assoc. Prof. Dr. Yuriy Kravchenko - National University of Life and Environmental Sciences of Ukraine (Kiev) - Ukraine
Assist. Prof. Dr. Sasan Rabieh - Shahid Beheshti University - Iran
Alma Ligata - Zenith Group - Bosnia and Herzegovina
Ismet Uzun - Zenith Group - Bosnia and Herzegovina
Musa Kose - Zenith Group - Bosnia and Herzegovina

WELCOME TO ICENS 2020

On behalf of the organizing committee, we are pleased to announce that the 6th International Conference on Engineering and Natural Sciences (ICENS 2020) held from October 21 to 25, 2020 in Belgrade, Serbia. ICENS provides an ideal academic platform for researchers to present the latest research findings and describe emerging technologies, and directions in Engineering and Natural Sciences issues. The conference seeks to contribute to presenting novel research results in all aspects of Engineering and Natural Sciences. The conference aims to bring together leading academic scientists, researchers and research scholars to exchange and share their experiences and research results about all aspects of Engineering and Natural Sciences. It also provides the premier interdisciplinary forum for scientists, engineers, and practitioners to present their latest research results, ideas, developments, and applications in all areas of Engineering and Natural Sciences. The conference will bring together leading academic scientists, researchers and scholars in the domain of interest from around the world. The scientific program will focus on current advances in the research, production and use of Engineering and Natural Sciences with particular focus on their role in maintaining academic level in Engineering and Applied Sciences and elevating the science level. The conference's goal will to provide a scientific forum for all international prestige scholars around the world and enable the interactive exchange of state-of-the-art knowledge. The conference will focus on evidence-based benefits proven in clinical trials and scientific experiments.

Best regards,

Prof. Dr.Özer ÇINAR

ICENS 6TH INTERNATIONAL CONFERENCE ON ENGINEERING AND NATURAL SCIENCE
October 21-25 2020 Belgrade

ICENS 6TH INTERNATIONAL CONFERENCE ON ENGINEERING AND NATURAL SCIENCE
October 21-25 2020 Belgrade

Investigation of Live-Bed Scour Around Circular Bridge Piers Under Flood Waves by Using Flow-3D

Firat Gumgum[1], M. Sukru Guney[2]

Abstract

In this study, an experiment concerning live-bed scour around circular bridge pier under unsteady flow conditions and its simulation performed by using the software FLOW3D are presented. Different turbulence models such as LES, RNG and two equations k-ε were tested separately and their effects on scour process were compared to each other, together with experimental findings. It was revealed that the LES turbulence model simulated better the scour around the pier while the RNG turbulence model simulated better both the scour in the wake region and the sediment transport. All these three turbulence models underestimated the scour depths compared to the experimental ones.

Keywords: Live-bed scour, bridge pier, flood waves, flow-3D

1. INTRODUCTION

Local scour around bridge piers was registered as the most important reason for the bridge failures [1]. The mechanism of the local scour plays an important role in the design of the bridge foundations and the determination of the protection measures. There are many theoretical and experimental studies performed to enlighten the mechanism of the local scour, to predict the geometry of the scour hole and to evaluate the safety precautions ([2], [3], [4], [5], [6], [7] etc). Channel bottom slope, grain diameter, grain uniformity, flow characteristics, type and shape of the foundation etc. and the relationships between these parameters can differ significantly and result in numerous combinations. It would be extremely inconvenient to study all these combinations experimentally, and the financial burden would be very heavy. Therefore, it is more convenient to perform 3D numerical analyses with different combinations, as performed by various researchers in recent years.

Local scour is investigated under two headings; clear water scour, without sediment motion in the channel and live-bed scour at which sediment moves in the channel and feeds the scour hole during the scour process. Live-bed scour studies are quite rare compared to those performed in clear water conditions and there are very few live-bed scour investigations performed under unsteady flow conditions.

In this study, an experiment concerning live-bed scour around circular bridge pier under unsteady flow conditions and its simulation performed by using the software FLOW3D are presented. Different turbulence models such as LES, RNG and two equations k-ε were tested separately and their effects on scour process were compared to each other, together with experimental findings.

2. EXPERIMENTAL SETUP

Experiments were carried out in a tilting flume 18.6 m long, 0.8 m wide and 0.75 m deep constructed in the Hydraulic Laboratory of Dokuz Eylul University Civil Engineering Department, within the scope of the project TUBITAK 106M274. The channel bottom slope was equal to 0.006. A schematic view of the flume is given in Fig. 1a.

[1] *Corresponding author: Dicle University Civil Engineering Department, Diyarbakir, Turkey, firat.gumgum@dicle.edu.tr*

[2] *Izmir University of Economics, Civil Engineering Department, Izmir, Turkey, sukru.guney@izmirekonomi.edu.tr*

The circular pier of diameter 4 cm was placed at the 12th meter of the flume. The first 8 m and the last 5 m of the flume were filled with 20 cm thick gas concrete blocks. After the 3rd meter of the flume, the flume was covered with non-rippling sediment having 1.63 mm median diameter (d50) and 1.303 geometric standard deviation (σg) to form a bed 25 cm thick.

Scour depth around the bridge pier was measured by Ultrasonic Velocity Profiler (UVP). Three transducers were located as follows: one at the upstream of the pier (T2) and two at the flanks of the pier (T1 and T3), as shown in Fig. 1b.

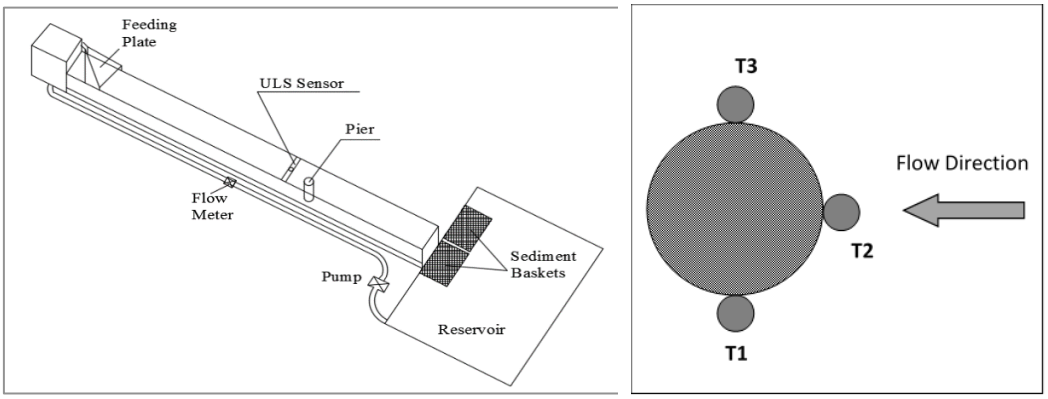

Figure 1. (a) Schematic view of the flume *(b) Location of the UVP transducers*

Flow depths were measured by UltraLab ULS (Ultrasonic Level Sensor) manufactured by General Acoustics. Sediment was fed into the flume manually by means of the sediment feeding plate designed to provide uniform feeding, and collected by means of the baskets located at the end of the flume. Initially, a base flow of 1.5 L/s was conveyed to the flume for 10 minutes to provide a steady state. No scour was observed during this stage, as intended. Then, the triangular hydrograph with peak discharge of 20 L/s was generated. The durations of rising and falling limbs were equal to 3 minutes. The evolution of the scour was recorded by means of a high precision camera. Experiments were repeated to ensure the accuracy of experimental findings.

3. NUMERICAL STUDY

In the numerical model, the last 5.6 meters of the flume was disregarded in order to reduce the number of the mesh cells, hence saving the simulation time. Mesh cell side was taken as 1 cm along the flow and lateral directions and 0.5 cm in the vertical direction. General overview of the flume model is given in Fig. 2. Red zones indicate the concrete blocks, blue zone indicates the packed sediment and cyan layer corresponds to the initial water surface.

Initial conditions (flow depth, velocity etc.) were defined as the initial steady state of the experiment. Simulation was realized by the isosceles triangle shaped hydrograph. LES, RNG and two equations k-ε turbulence models were used during the simulations. Maximum turbulent mixing length was chosen as “dynamically computed” because of time-varied flow depths. Critical Shields parameter was calculated from Shields diagram as 0.038. The frequently used Meyer-Peter & Muller equation was chosen to predict the bed load transport. As suggested in Flow-3D manual, the bed load and entrainment coefficients were taken as 8 and 0.018 respectively [8].

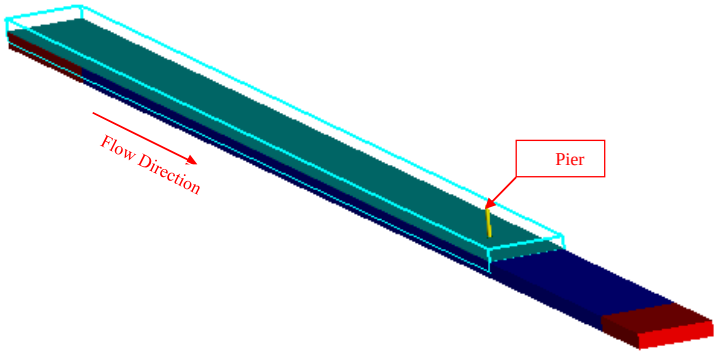

Figure 2. General overview of the flume model

4. RESULTS AND DISCUSSION

During the experiment, water level in the flume began to rise after the base flow of ten minutes. Flow filaments were evidently separated into two directions at the flanks of the pier and wake region began to develop. Two separate scour holes began to form at the flanks of the pier and met in front on the pier a few seconds later. With the increasing discharge, the development of horseshoe vortices enhanced the size of the scour hole rapidly and the scour hole took the shape of a frustum. After the flow velocity reached its critical value, sediment began to move and supply to the scour hole, causing fluctuations in scour depth and scour depth began to decrease during the falling limb. The bed material removed from the scour hole, and was drifted to downstream, 3-4 pier diameters away from pier, by wake vortices.

Similar process was obtained from the simulations. Figs. 3a and 3b represent the velocity fields in the wake region and at surrounding of the pier at peak time, respectively. In Figure 3 a, the wake region with the separation of the flow due to the pier existence can be distinguished. Its boundaries can be seen between the yellow and orange velocity fields. According to the velocity fields in Figure 3 b, downflow and horseshoe vortices seem not to be fully reflected.

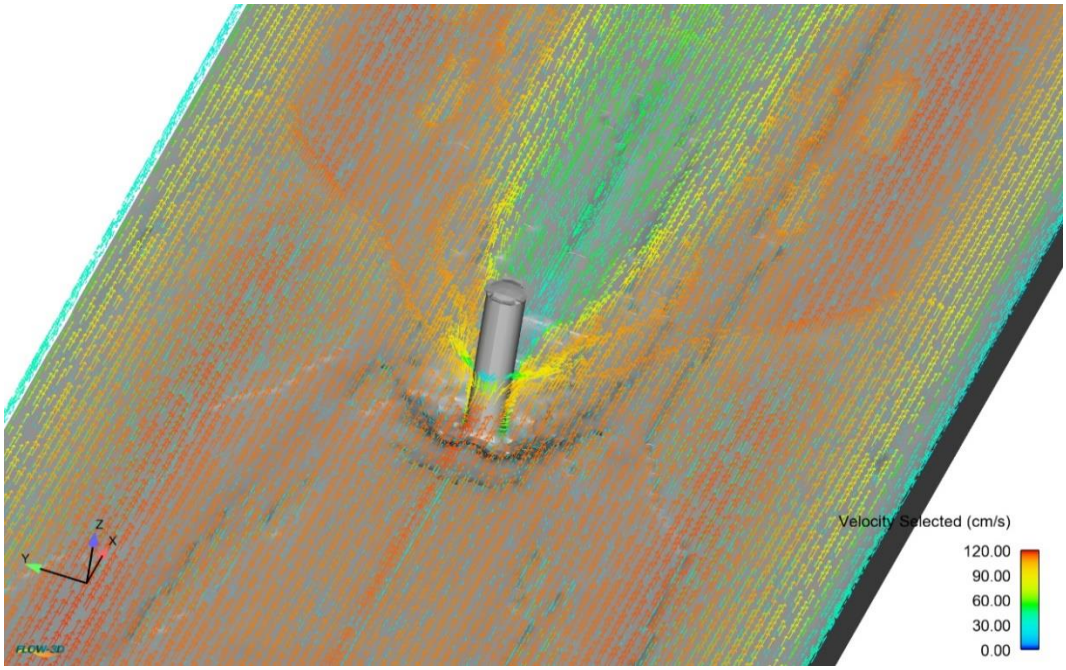

Figure 3. (a) The velocity field at the peak time in the wake region

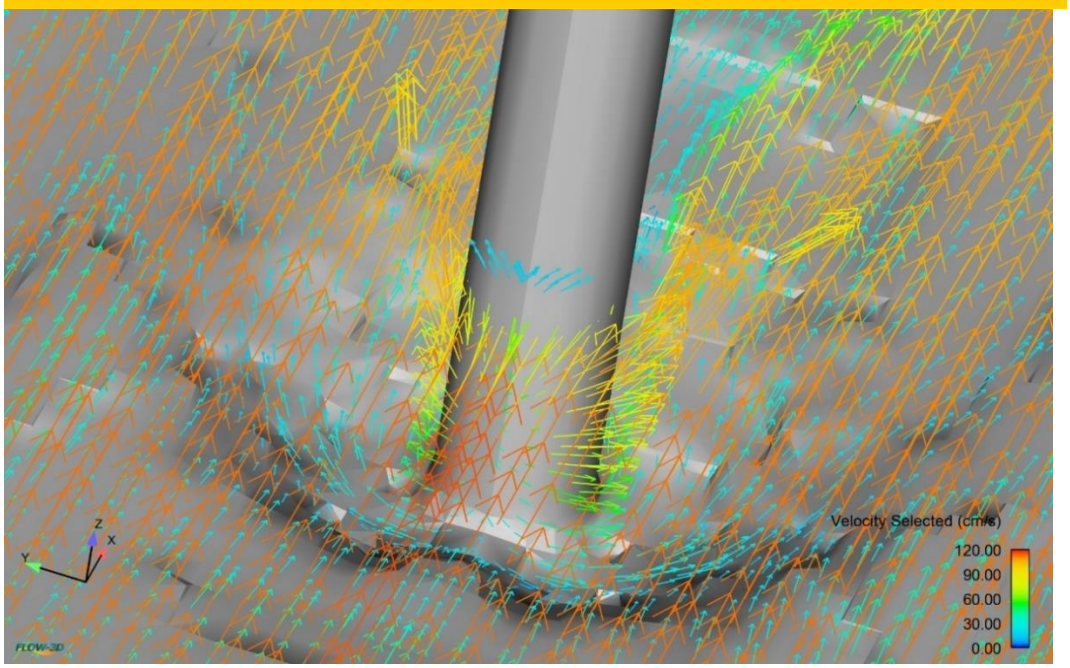

Figure 3. (b) The velocity field at the peak time in the surrounding of the pier

3D pictures of the scour hole were taken for each turbulence model at every 60 seconds. They are given in Figures 4, 5 and 6. for LES, RNG and two equation k-ε turbulence models, respectively.

The picture of scour hole corresponding to the end of the experiment is given in Figure 7.

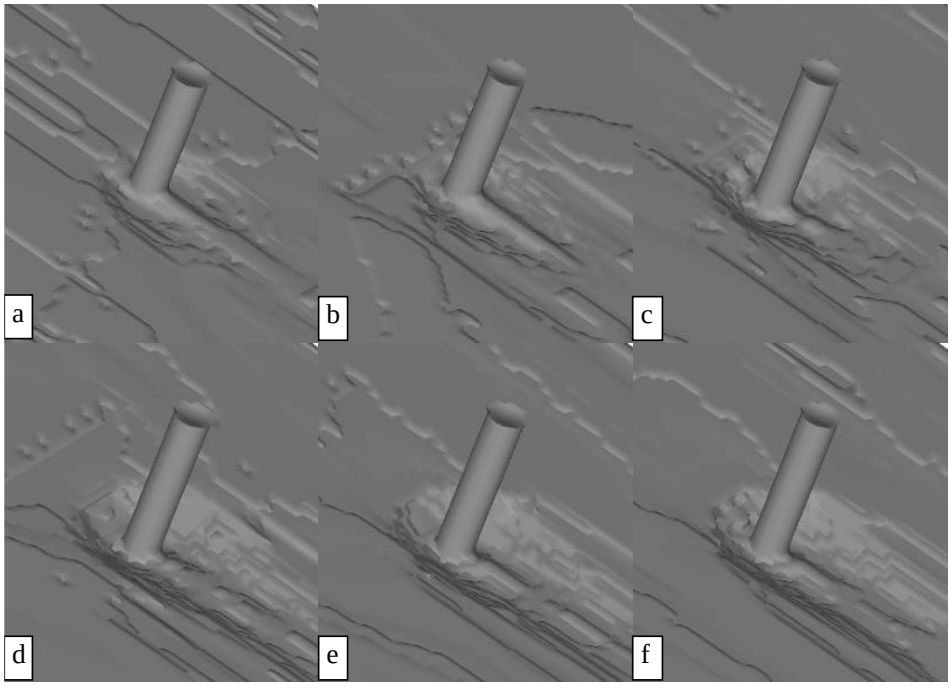

Figure 4. Pictures of the scour hole for LES turbulence model at a) 60 s. b) 120 s. c) 180 s. d) 240 s.

e) 300 s. f) 360 s.

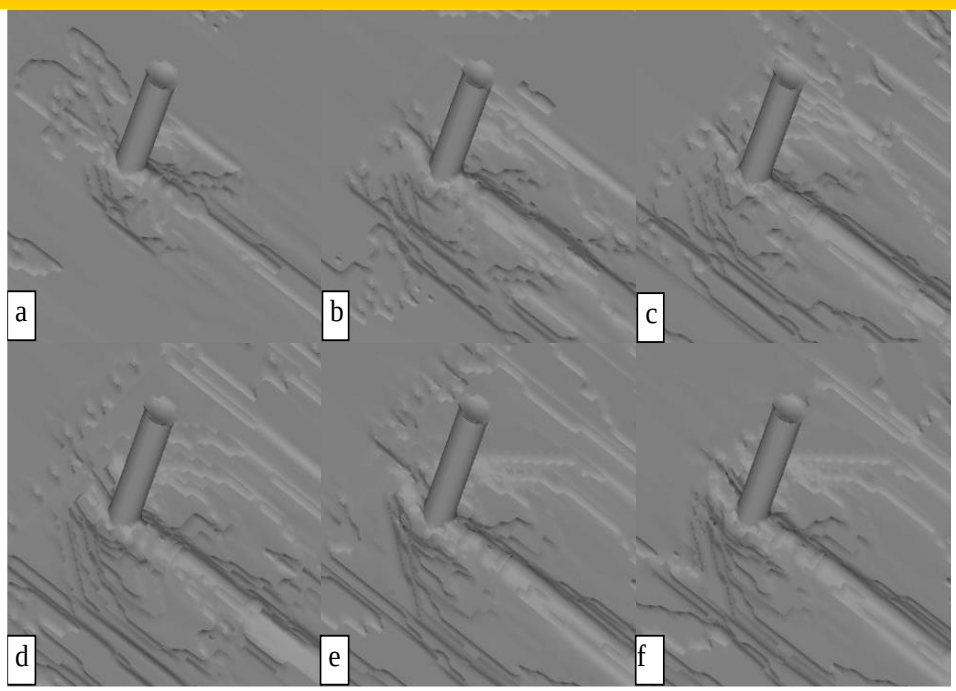

Figure 5. Pictures of the scour hole for RNG turbulence model at a) 60 s. b) 120 s. c) 180 s. d) 240 s. e) 300 s. f) 360 s.

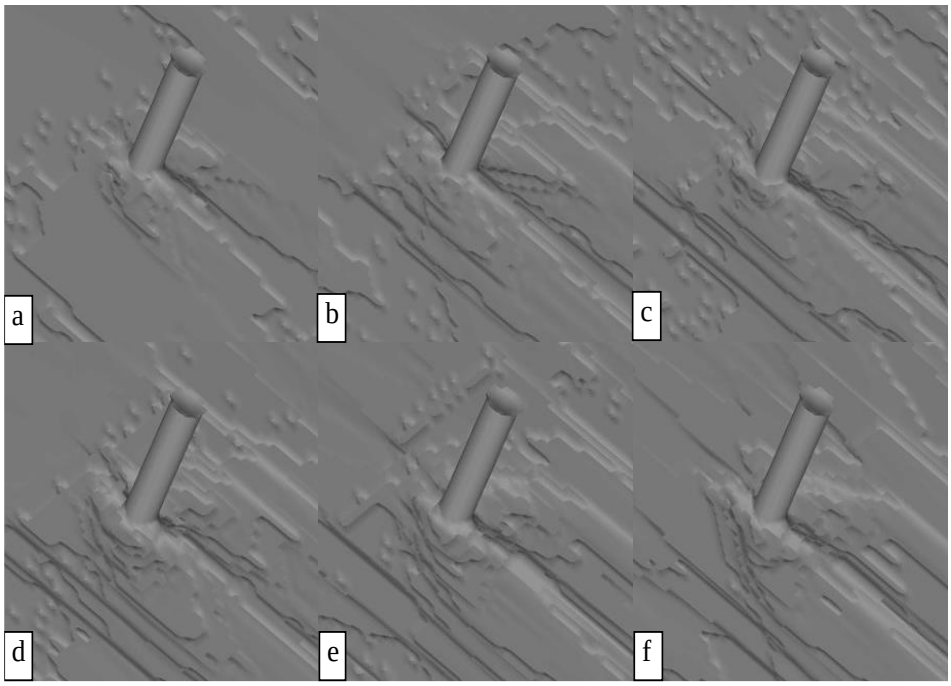

Figure 6. Pictures of the scour hole for k-ε turbulence model at a) 60 s. b) 120 s. c) 180 s. d) 240 s. e) 300 s. f) 360 s.

Figure 7. Picture of the scour hole at the end of the experiment (t=360 s)

It was found that the scour hole obtained by using the LES turbulence model was more similar to that obtained from the experiment. A "linear bump" occurred in front of the pier in all turbulence models but, this fact was not observed during the experiments. The frustum shaped of the scour hole seen in Fig. 7 was not obtained in the used turbulence models, except LES turbulence model at which this configuration appeared between 180 and 240 seconds. This situation caused lower scour depths in front of the pier compared to those at flanks, this fact being contradictory to the experimental results.

Maximum scour depths were observed approximately at the 240th second of the simulations. Figure 8, 9 and 10 show plan views of the scour hole at 240th s of the simulation for LES, RNG and two equations k-ε turbulence models, respectively (units are in centimeters). The LES turbulence model simulated scouring in front of the pier much better than the other turbulence models even if it gave lower scour depths compared to those at flanks. The RNG turbulence model simulated scouring in wake region better than the LES model.

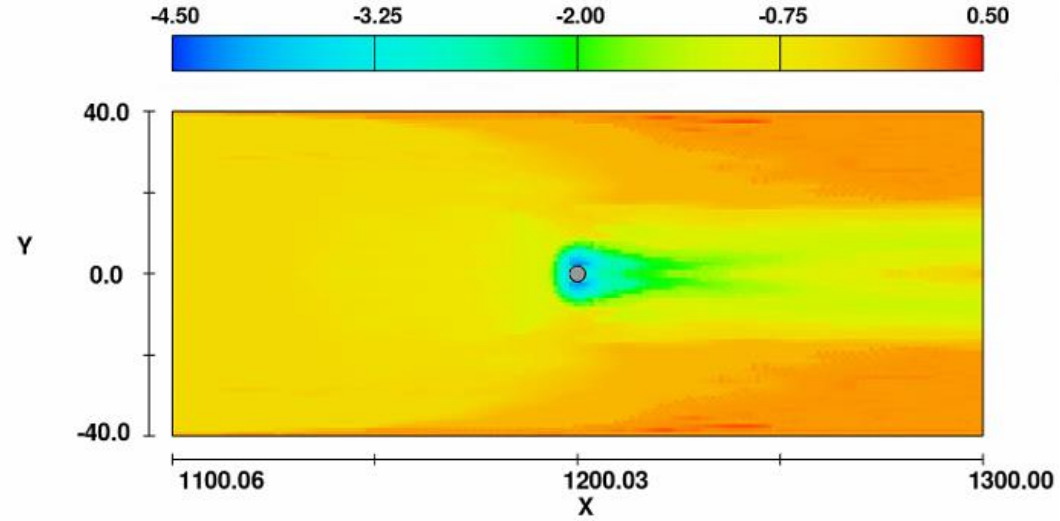

Figure 8. Plan view of scour holes in the case of the turbulence model LES

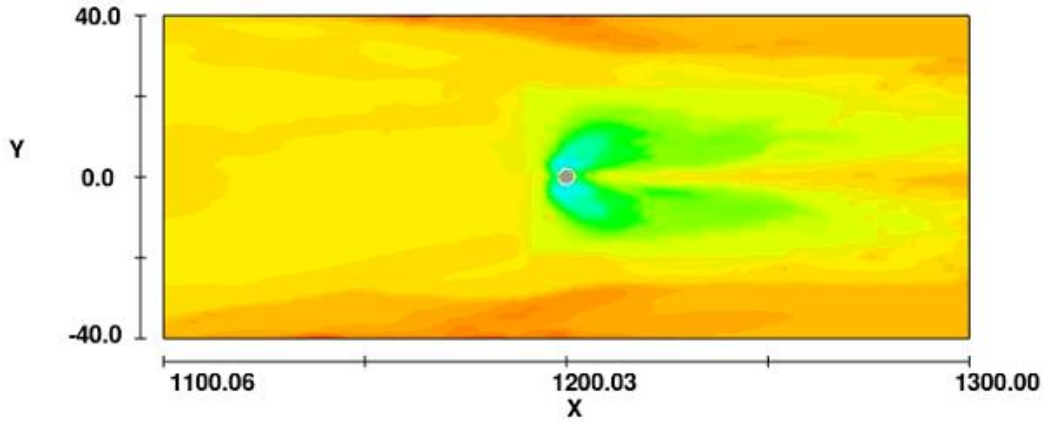

Figure 9. Plan view of scour holes in the case of the turbulence model RNG

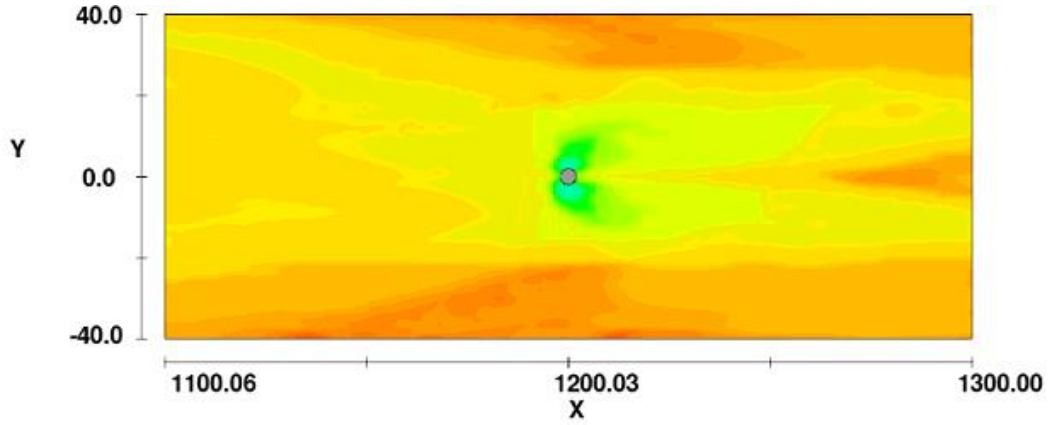

Figure 10. Plan view of scour holes in the case of the turbulence model two equations k-ε

The numerical and experimental time dependent scour depths at flank (T1) and front (T2) are given in Figure 11.

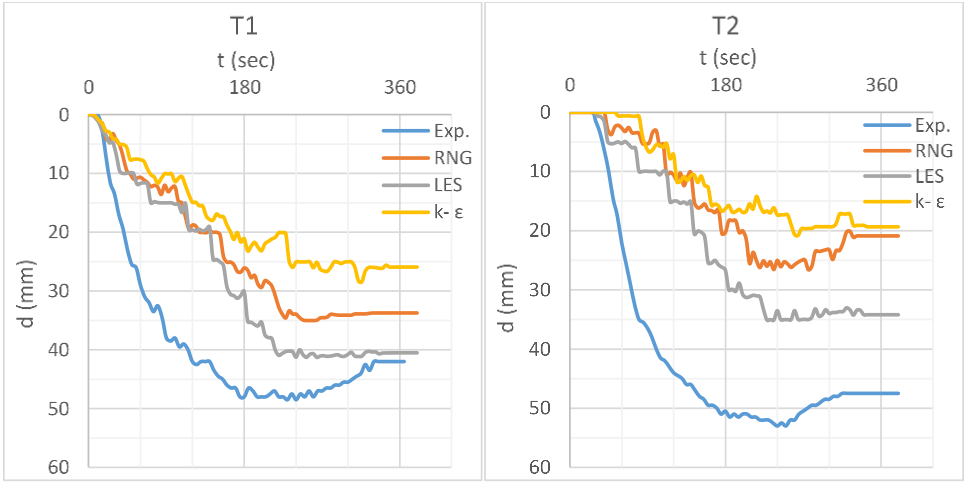

Figure 11. Time-varied numerical scour depths and experimental ones

The time-varied scour depths obtained from the simulations were found to be smaller than the experimental ones.

Scouring was found to be more rapid during the experiments. For example, at flank T1, during the experiments the scour depth of 20 mm was reached approximately at the 40th second, while this value was 115 s, 130 s, and 165 s in the case of the turbulence models LES, RNG and two equations k-ε, respectively.

By contrast with experimental findings, the scour depths at front were found smaller compared to those calculated at flanks.

The turbulence model RNG seems to reflect better the sediment transport, since the final scour depth was found to be smaller than the maximum scour depth. On the other hand, the scour depths calculated by using turbulence model LES are relatively much closer to those obtained from the experiments.

This study is a part of elaborated experimental and numerical investigations. Numerical analyses continue to be performed with various data such as different mesh sizes, coefficients and hydrographs.

REFERENCES

[1]. K. Wardhana, and F.C. Hadipriono, "Analysis of Recent Bridge Failures in the United States," *Journal Of Performance Of Constructed Facilities*, vol. 17:3, pp. 144–150, 2003.
[2]. E.M. Laursen, and A. Toch, "Scour around bridge piers and abutments," Iowa Highway Research Board, Ames, IA, vol. 4, 1956.
[3]. B. W. Melville, "Local scour at bridge sites," Ph.D. thesis, The University of Auckland, Auckland, 1975.
[4]. H. N. C. Breusers, G. Nicollet, and H. W. Shen, "Local scour around cylindrical piers," *Journal of Hydraulic Research*, vol. 15:3, pp. 211-252, 1977.
[5]. S. C. Jain, and E. E. Fischer, "Scour around bridge piers at high flow velocities," *Journal of the Hydraulics Division*, vol. 106:11, pp. 1827-1842, 1980.
[6]. Y. M. Chiew, "Local scour at bridge piers," Ph.D. thesis, The University of Auckland, Auckland, 1984.
[7]. U. C. Kothyari, K. G. Ranga Raju, and R. J. Garde, "Live-bed scour around cylindrical bridge piers," *Journal of Hydraulic Research*, vol. 30:5, pp. 701-715, 1992.
[8]. C. W. Hirt, *Flow-3D user manual version 10*, Flow Science, 2011.

ICENS 6TH INTERNATIONAL CONFERENCE ON ENGINEERING AND NATURAL SCIENCE
October 21-25 2020 Belgrade

Can Controlled Hodgkin − Huxley Neuron Model Quantum Computations?

***Sergey Borisenok*[1]**

Abstract

The dynamical system corresponding to the Hodgkin-Huxley (HH) neuron contains the control parameter, for instance the electrical current or other external signal, stimulating the action potential (outcome) in the axon. Choosing the appropriate shape of the control via speed gradient or alternative algorithms one can keep the system imitating a quantum behavior. The controlled four-dimensional HH system in this case involves the effects similar to the quantum phase contributions to the computational process. We provide a simple example of the HH-based computational algorithm following the quantum paradigm. Our approach can open a novel method for the practical realization of quantum algorithms and develop new perspectives for the computational properties of artificial neural networks.

Keywords: Hodgkin-Huxley neuron, quantum computation

1. INTRODUCTION

The area of quantum informatics covers presently a wide range of computational algorithms based on new 'quantum logic' paradigm. In parallel, the set of classical emulations of quantum algorithms starts to be in the focus of research.

To model quantum computations one need to find a classical system with specific propereties. First of all, it should be able to imitate efficiently effects of the quantum phase contributions. The system must be multi-dimensional in the phase space, and it has to demonstrate the variety of dynamical regimes.

Here we discuss the dynamical system corresponding to the Hodgkin-Huxley (HH) mathematical neuron represented with four ordinary differential equations. Also it contains an one-dimensional control parameter, the electrical current or other similar external signal, stimulating the action potential in the axon.

We provide the simple example of the HH-based computational algorithms following the quantum paradigm. It is the Deutsch – Jozsa quantum procedure for a simple searching problem. We define the 'states' of HH neuron emulating the pure qubit states, and propose a simple measurement procedure of resting or spiking of the following HH neuron to the searching problem in a single algorithmic cycle.

2. QUANTUM COMPUTATIONS

To describe the basic features of quantum computations, let's revive briefly the mathematical approach to the main object: quantum bit (qubit). Sure, its evolution mostly follows von Neumann's equation for the density operator ρ, and it cannot be reduced to the classical description.

Nevertheless, under some simplification we can present the dynamical system describing qubit with the set of real ordinary differential equations. If there is no decay due to the coupling of qubit with the environment, it is represented via three independent variables.

[1]*Corresponding author: Department of Electrical and Electronics Engineering, Faculty of Engineering, Abdullah Gul University, 38080 Kocasinan / Kayseri, Turkey.* sergey.borisenok@agu.edu.tr

2.1. Quantum bits

In the case of 'ideal' qubit (there is no decay) the system can be represented as a set of ordinary differential equations [1]:

$$\begin{aligned} \frac{dx}{dt} &= y; \\ \frac{dy}{dt} &= -x - u \cdot z; \\ \frac{dz}{dt} &= u \cdot y, \end{aligned} \tag{1}$$

where the functions could be expressed via the density operator elements:

$$\begin{aligned} x &= \rho_{12} \exp\{i\omega t\} + \rho_{21} \exp\{-i\omega t\}; \\ y &= i\left[\rho_{12} \exp\{i\omega t\} - \rho_{21} \exp\{-i\omega t\}\right]; \\ z &= \rho_{22} - \rho_{11}. \end{aligned} \tag{2}$$

Here the time is dimensionless, normalized in the units of $\omega = (E_2 - E_1)/\hbar$.

The variables *x* and *y* in (1) corresponds to the phase contribution, the variable z is inversion, i.e. the difference of probabilities to find the qubit in two pure states. The dimensionless parameter *u* plays a role of a quasi-classical external control field.

It is easy to check that for any moment of time: $x^2 + y^2 + z^2 = 1$. Thus, all the evolution of the qubit takes place on the surface of a unity sphere (the 'Bloch sphere').

2.2. Deutsch – Jozsa algorithm

To give an example of a quantum algorithm, let's chose the simple searching problem. Suppose that we get a function f mapping $\{0,1\}^n$ into $\{0,1\}$. The constrain on the function gives us only two options: or the function is a constant: $f(x) = 0$ for all x from $\{0,1\}^n$ or $f(x) = 1$ all x from $\{0,1\}^n$, or it is balanced: the number of inputs 0 for the mapping is equal to the number of inputs 1. We must check if the given function f is a constant.

To do it for the classical approach we need $2^{n-1} - 1$ evaluations. Quantum algorithms, from another hand, can perform it much faster.

The basic solution to this searching problem has been proposed by Deutsch in 1985 and generalized in 1992 in the form of the Deutsch – Jozsa algorithm for an arbitrary positive integer n [2].

The circuit for the Deutsch – Jozsa algorithm is given in Fig.1. It contains three single-qubit Hadamard gates, one two-qubit gate for the function f and one measurement operation. The symbol $\oplus$ stands here for the addition mod 2.

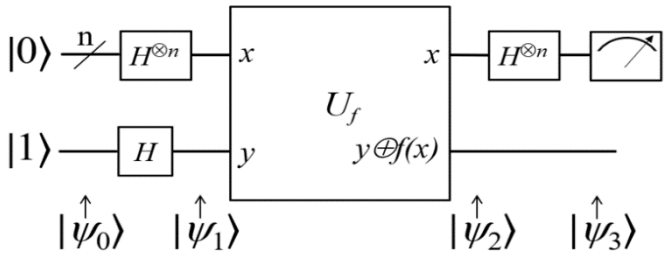

Figure1. The quantum circuit for the Deutsch – Jozsa algorithm; based on [2].

For simplicity we will focus here on the case $n = 1$. Then the result of the measurement is equal to:

$$\left|\text{output}\right\rangle = \frac{1}{2}\left[(1+(-1)^{f(0)\oplus f(1)})\left|0\right\rangle + (1-(-1)^{f(0)\oplus f(1)})\left|1\right\rangle\right]. \tag{3}$$

Eq.(3) solves the problem of searching. Indeed, if $f(0)\oplus f(1)=0$, then the output is $\left|0\right\rangle$, and the function f is constant. If $f(0)\oplus f(1)=1$, then the output is $\left|1\right\rangle$, and the function f is balanced. Due to the so-called quantum phase kick-back effect in the algorithm we need only a single measurement to distinguish between those two cases. The same is valid for the case of n bits. If all n measurement results are $\left|0\right\rangle$, we conclude that the function was constant. Otherwise, if at least one of the measurement outcomes is $\left|1\right\rangle$, we conclude that the function was balanced.

3. CLASSICAL HODGKIN − HUXLEY NEURON

The question now is how to develop the similar paradigm based on the quantum computation and applied it to the classical system of Hodgkin − Huxley neuron.

The mathematical description of HH neuron has been proposed by Alan Lloyd Hodgkin and Andrew Huxley in 1952 as a phenomenological model based on the experiments when the giant axon of the squid has been stimulated by the electrical current.

3.1. ODE model for Hodgkin − Huxley neuron

The Hodgkin-Huxley differential model has the set of four variables: the output membrane action potential $v(t)$ and three ion channels variables $m(t)$, $n(t)$, $h(t)$ related to the probabilities for the membrane gates to be open or closed [3]:

$$\begin{aligned}
&C_M\cdot\frac{dv}{dt} = -g_{Na}m^3h\cdot(v-E_{Na}) - g_K n^4\cdot(v-E_K) - g_{Cl}\cdot(v-E_{Cl}) + I(t);\\
&\frac{dm}{dt} = \alpha_m(v)\cdot(1-m) - \beta_m(v)\cdot m;\\
&\frac{dn}{dt} = \alpha_n(v)\cdot(1-n) - \beta_n(v)\cdot n;\\
&\frac{dh}{dt} = \alpha_h(v)\cdot(1-h) - \beta_h(v)\cdot h.
\end{aligned} \tag{4}$$

The membrane variables m, n, h depend on the action potential v via the non-linear functions:

$$\begin{aligned}
&\alpha_m(v) = \frac{0.1\cdot(25-v)}{\exp\left\{\frac{25-v}{10}\right\}-1};\ \beta_m(v) = 4\cdot\exp\left\{-\frac{v}{18}\right\};\\
&\alpha_n(v) = \frac{0.01\cdot(10-v)}{\exp\left\{\frac{10-v}{10}\right\}-1};\ \beta_n(v) = 0.125\cdot\exp\left\{-\frac{v}{80}\right\};\\
&\alpha_h(v) = 0.07\cdot\exp\left\{-\frac{v}{20}\right\};\ \beta_h(v) = \frac{1}{\exp\left\{\frac{30-v}{10}\right\}+1}.
\end{aligned} \tag{5}$$

The net external current $I(t)$ stimulating the axon is a control parameter in the HH model (4). The set of constants includes the potentials E_{Na} (equilibrium potential at which the net flow of *Na* ions is zero), E_K (equilibrium potential at which the net flow of *K* ions is zero), E_{Cl} (equilibrium potential at which leakage is zero) in mV, the membrane

capacitance C_M and the conductivities g_{Na} (sodium channel conductivity), g_K (potassium channel conductivity), g_{Cl} (leakage channel conductivity) in mS/cm^2:

$$\begin{aligned} g_{Na} &= 120;\ E_{Na} = 115\,; \\ g_K &= 36;\quad E_K = -12\,; \\ g_{Cl} &= 0.3;\ E_{Cl} = 10.36. \end{aligned} \tag{6}$$

The important property of the dynamical system (6) is the variety of regimes: it can demonstrate resting (the neuron does not show a sufficient activity), spiking (the neuron produces a single spike), bursting (the neuron generates series of spikes).
The particular dynamical regime depends on the input current I. For instance, if the current is below a threshold level, the HH neuron stays in resting; if we overcome the threshold level, it generates a spike.

3.2. Linear chain of Hodgkin − Huxley neurons

If we combine few HH neurons in a linear chain, the output action potential of the previous one defines the input of the following cell. We use here our gain model for the transfer of the output signal from k-th neuron via its synapse towards the dendrite/soma input of the l-th neuron [4]:

$$I_l(t) = \alpha \cdot [v_k(t) - v_{\text{rest}}]\,;\ \alpha = \text{const} > 0, \tag{7}$$

with the phenomenological gain constant α. Here v_{rest} is the reference rest potential in the HH neuron.
We use a simple linear chain of two HH neurons. The first cell plays a role of the computational element, while the second one works as a measuring element. For that we define the threshold (tr) level:

$$I_{\text{tr}} = \alpha \cdot (v_{\text{tr}} - v_{\text{rest}})\ . \tag{8}$$

Now the output of the first neuron stimulates the particular regime of the second measuring element. If the first HH neuron produces the acting potential below the threshold level v_{tr}, the second neuron does not spike. If the output action potential of the first neuron v overcomes slightly the threshold level, the second one produces a single spike.

3.3. 'Quantum states' of HH neuron

To imitate the Deutsch algorithm, let's define the 'pure quantum states' for the HH neuron: the resting $|0\rangle$ and the single spiking $|1\rangle$:

$$\begin{aligned} |0\rangle &= 0 \cdot I_{\text{tr}}\,; \\ |1\rangle &= 1 \cdot I_{\text{tr}}\,, \end{aligned} \tag{9}$$

which corresponds to the action potentials:

$$\begin{aligned} v_{|0\rangle} &= v_{\text{rest}} + \frac{0 \cdot I_{\text{tr}}}{\alpha} = v_{\text{rest}}\ ; \\ v_{|1\rangle} &= v_{\text{rest}} + \frac{1 \cdot I_{\text{tr}}}{\alpha} = v_{\text{rest}} + \frac{I_{\text{tr}}}{\alpha}\ . \end{aligned} \tag{10}$$

To unify both cases, let's define the goal potential via the CNOT logical operator over the function f:

$$v_* = v_{\text{rest}} + \text{CNOT}\{f(0), f(1)\} \cdot \frac{I_{\text{tr}}}{\alpha}\ . \tag{11}$$

The symbol * stands here for the potantial v (the output of the first neuron) which should be the goal of our control signal I in (4).

Now suppose that we are able to drive the first neuron towards the goal potential (11). Then it will stimulate the second measuring element with two different options: the second neuron will stay in rest or will generate a single spike. Just based on that we can conclude if the function *f* is constant or not:

$$\begin{aligned} &\text{If } f(0)=f(1), \text{ then } v_* = v_{\text{rest}} = v_{|0\rangle}, \text{ and } f \text{ is constant.} \\ &\text{If } f(0)\neq f(1), \text{ then } v_* = v_{\text{rest}} + \frac{I_{\text{tr}}}{\alpha} = v_{|1\rangle}, \text{ and } f \text{ is balanced.} \end{aligned} \tag{12}$$

In (12) we got the complete HH analog of the Deutsch algorithm.

3.4. Target attractor feedback

The last task is to provide the necessary output (11) of the first neuron. To do it, we can apply different control algorithms based on the gradient approaches [5] or, alternatively, on the construction in the system target attractors, in the manner of 'synergetic' Kolesnikov's algorithm [6].

Here we follow Kolesnikov's approach. To do that, let's define the target function:

$$\psi(t) = v(t) - v_*(t)\,. \tag{13}$$

Minimazing the magnitude of (13) we drive our system towards the target potential (11). The control equation follows the method [6]:

$$T\frac{d\psi(t)}{dt} = -\psi(t)\,. \tag{14}$$

The positive constant *T* defines the typical time scale of the target attractor achivement.

Eq.(14) provides the exponentially convergent dynamics of the trajectories to the neighborhood of the target attractor (13) in the phase space.

Then the control signal *I* in the first HH neuron is restored from the substitution of (13)-(14) into the first equation of the system (4). It becomes:

$$\begin{aligned} I = C_M \cdot \left[\frac{dv_*}{dt} - \frac{1}{T}(v - v_*)\right] + g_{Na} m^3 h \cdot (v - E_{Na}) + \\ + g_K n^4 \cdot (v - E_K) + g_{Cl} \cdot (v - E_{Cl})\,. \end{aligned} \tag{15}$$

The achievability of the goal for an arbitrary stabilization / tracking via target attractor feedback has been proved in [7].

3.5. Finalization of the algorithm

Now we are ready to finalize the HH analog of the Deutsch algorithm. Its sequent scheme is:

$$f \Rightarrow v_* \Rightarrow I \Rightarrow v = v_{|0\rangle} \text{ or } v = v_{|1\rangle}$$

We need to take a sequence of two HH neurons. For the first neuron we apply the control input *I* from (15) based on the goal action potential v_* from (11) defined over the function *f*. The potential *v* produced in the first neuron via the gain transfer (7) comes to the second neuron, i.e. to the measuring element. We need to detect if it stays in the resting or spiking. If we observe the rest, the function *f* is constant. If it spikes, *f* is balanced.

CONCLUSIONS

We provided here the simple example of the HH-based computational algorithms following the quantum paradigm. We proved that the controlled 4-dimensional Hodgkin − Huxley system is capable to imitate the effects similar to the quantum phase contributions to the computational process.

Our control algorithm is robust, it does not depend on the initial state of the HH neuron, and it is stable under the relatively small external perturbation and noise.

Our algorithm involves two HH neurons, the first one works as analog of the whole Deutsch – Jozsa quantum circuit in Fig.1, the second HH elements serves as a measurement device. As in Deutsch – Jozsa's quantum algorithm, we need only a single measurement to solve the searching problem for the function *f*.

Our approach demonstrates a new way for the practical realization of quantum algorithms in classical artificial neural networks. Such ANN must include the neurons with high dimension of their phase space, like in the case of Hodgkin – Huxley elements.

REFERENCES

[1]. A. N. Pechen, S. Borisenok, "Energy transfer in two-level quantum systems via speed gradient-based algorithm", *IFAC-PapersOnLine*, vol 48-11, pp 446-450, 2015.
[2]. P. Aradyamath, N. M. Naghabhushana, R. Ujjinimatad, "Quantum computing concepts with Deutsch Jozsa algorithm", *International Journal of Informatics Visualization*, vol 3, pp 59-68, 2019.
[3]. A. L. Hodgkin, A. F. Huxley, "Currents carried by sodium and potassium ions through the membrane of the giant axon of Loligo", *The Journal of Physiology*, vol 116 (4), pp 449-72, 1952.
[4]. S. Borisenok, O. Catmabacak, Z. Unal, "Control of collective bursting in small Hodgkin-Huxley neuron clusters", *Communications Faculty of Sciences University of Ankara Series A2-A3*, vol 60, pp 21-30, 2018.
[5]. A. L. Fradkov, *Cybernetical Physics: From Control of Chaos to Quantum Control*, Berlin, Heidelberg, Germany: Springer, 2007.
[6]. A. Kolesnikov, *Synergetic Control Methods of Complex Systems*, Moscow, Russia: URSS Publ., 2012.
[7]. S. Borisenok, Z. Unal, "Tracking of arbitrary regimes for spiking and bursting in the Hodgkin-Huxley neuron", *MATTER: International Journal of Science and Technology*, vol 3, pp 560-576, 2017.

ICENS 6TH INTERNATIONAL CONFERENCE ON ENGINEERING AND NATURAL SCIENCE
October 21-25 2020 Belgrade

Target Repeller Feedback Control over the Ergotropy of Quantum Battery

***Sergey Borisenok*[1]**

Abstract

Here we discuss the model of a single-qubit based quantum battery (QB) in the form of quantum oscillator in a Markovian bath environment. For the effective control we apply here Kolesnikov's type feedback algorithm, but we re-formulate it to produce in the system a target repeller. This method makes the effective design of the control fields charging the battery; the corresponding control signals could be restored explicitly from the dynamical equations. Using this novel approach, we investigate the control over the quantum battery ergotropic characteristics of the harmonic oscillator QB. The proposed algorithm could be applied also for different physical realizations of quantum batteries: Dicke QB, spin QB,; and for all working stages of the QB (charging, long time storage and the energy transfer to a consumption center or engine).

Keywords: quantum battery, ergotropy, feedback control

1. INTRODUCTION

Quantum Battery (QB) is a quantum device which is capable to perform its three basic tasks [1]:

- It can be ***charged***, i.e. it can be transferred from its lower energy state to more energetic states. The important fact is that charging / discharging processes are not necessarily unitary, and during this process QB may interact with its environment.
- It can efficiently ***store*** the transferred energy at energy levels and coherence.
- It can ***transfer*** the storage energy to consumption centers.

The schematic diagram of an open Quantum Battery B interacting with the charger A is represented in Fig.1. Each of sub-systems, A and B, are coupled individually into an environment. In addition, one can apply an external control field to charger A [2].

There are different physical realizations of qubit-based QBs: Dicke QB, spin QB, harmonic oscillator QB. Here we will discuss the last one in the form of bosonic ***harmonic oscillator QB***: the sub-system B is composed by N non-mutually interacting elements.

An alternative approach is studying multi-level quantum systems. For instance, when the three-level system is in the ground state, it is equivalent to a bare battery, the intermediate state is regarded as a partially charged battery, and the maximum excited state represents a fully charged battery [3].

The effect of the global driving-field phase on the charging process has been studied in [3] for an open loop control, and it has been found that both the maximum extractable work (ergotropy) and the charging power vary periodically under different control fields, with a period of 2π.

The effective working of a quantum battery is expressed via different basic characteristics: its ergotropy, its charging power, the storage capacity and others. Feedback algorithms could be efficiently applied to control all of them at the different working stages of the QB: the charging, the long time storage and the energy transfer to a consumption center or engine.

[1]*Corresponding author: Department of Electrical and Electronics Engineering, Faculty of Engineering, Abdullah Gul University, 38080 Kocasinan / Kayseri, Turkey. sergey.borisenok@agu.edu.tr*

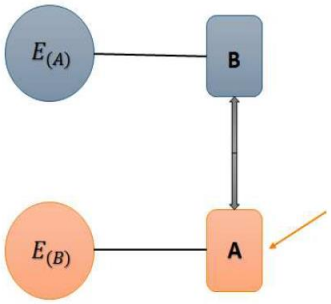

Figure 1. The schematic diagram of an open quantum battery B interacting with the charger A [2].

In this paper we discuss a novel method of target repeller feedback control over the ergotropy of quantum battery.

2. MODEL HAMILTONIAN

For simplicity we discuss here one type of QBs: bosonic quantum battery based on a single qubit. The charger A of such a battery B (see Fig.1) is implemented via the field which controls pumping the energy into the battery. Such a model covers also a energy decay due to the coupling of QB with the environment.

2.1. Ergotropy of quantum battery

One of the most important characteristics of QB is the difference between the useful energy exacted from QB in the state ρ and its energetically lowest accessible state σ_ρ . It could be defined via the battery Hamiltonian H as [4]:

$$W = \mathrm{Tr}(\rho H) - \mathrm{Tr}(\sigma_\rho H) \ . \tag{1}$$

The dynamical characteristics (1) is called the ***ergotropy*** of quantum battery.

2.2. Harmonic oscillator QB

We consider here a single-qubit based QB in the form of quantum oscillator with the density operator ρ in a Markovian bath. Such a system could be described with the Lindblad-type operator equation [5]:

$$\frac{d\rho}{dt} = -i[H_0 + u(t)\hat{Q}, \rho] + \hat{L}[\rho] \ , \tag{2}$$

with the terms based on the corresponding creation-annihilation operators:

$$H_0 = \left(\omega_0 + \frac{1}{2}\right)a^+ a \ ; \quad \hat{Q} = \frac{a^+ + a}{\sqrt{2\omega_0}} \ ; \quad \hat{P} = i\sqrt{\frac{\omega_0}{2}}(a^+ - a) \ . \tag{3}$$

The Lindblad operator here has a form:

$$\hat{L}[\rho] = \gamma \cdot (n(t)+1)\left(2a\rho a^+ - \rho a^+ a - a^+ a\rho\right) + \gamma \cdot n(t)\left(2a^+\rho a - aa^+\rho - \rho aa^+\right) \ . \tag{4}$$

The positive γ plays here a role of coupling constant between the qubit and the bath. There are two control parameters, $u(t)$ and $n(t)$, in the system.

2.3. System of real differential equations

The quantum model (2)-(4) can be re-written in the real representation [6]:

$$\begin{aligned}\frac{dE}{dt} &= 2\gamma\cdot(\omega_0 n(t)-E)-u(t)P\ ;\\ \frac{dQ}{dt} &= P-\gamma\cdot Q\ ;\\ \frac{dP}{dt} &= -\omega_0^2 Q-\gamma\cdot P-u(t)\end{aligned} \tag{5}$$

via the 'quasi-classical' variables

$$E(t)=Tr(H_0\rho)\ ;\ Q(t)=Tr(\hat{Q}\rho)\ ;\ P(t)=Tr(\hat{P}\rho)\ . \tag{6}$$

The ergotropy (1) in the system (5) could be defined as:

$$W(t)=E(t)-E_0\ , \tag{7}$$

where E_0 stands for the lowest accessible passive battery state.

3. CONTROL ALGORITHM

There is a variety of control algorithms applied to QBs [6]: they could be based on Fradkov's speed gradient [7] or, alternatively, Kolesnilov's target attractor feedback [8]. Here we develop a novel method based the approach proposed in [9] for the suppression of epileptiform regime in artificial neural networks.

3.1. Target Repeller Feedback

The Target Repeller Feedback (TRF) approach creates in the system (5) a dynamical target repeller driving the trajectories in the phase space far away from the certain parameter. In our case we apply it for the ergotropy (7) such, that TRF will maximize W exponentially:

$$\frac{dW}{dt}=\frac{1}{T_1}W\ . \tag{8}$$

In the system (5) we have two control parameters, for that reason we will write two control equation, one for the function $E(t)$ via TRF equation (8), another for the function $P(t)$ in the form of Kolesnikov's algorithm [8]:

$$\begin{aligned}\frac{dE}{dt} &= \frac{1}{T_1}(E-E_0)\ ;\\ \frac{dP}{dt} &= -\frac{1}{T_2}(P-P_*)\ .\end{aligned} \tag{9}$$

Here T_1 and T_2 are positive constants.

Eqs (9) provides the solution with the exponential behaviour:

$$\begin{aligned}E(t) &= [E(0)-E_0]\cdot e^{t/T_1}+E_0\ ;\\ P(t) &= P(0)\cdot e^{-t/T_2}+P_*\cdot(1-e^{-t/T_2})\ .\end{aligned} \tag{10}$$

By the substitution of (9) into Eqs (5) we can restore the control signals:

$$u(t) = \frac{P - P_*}{T_2} - \gamma \cdot P - \omega_0^2 Q \; ;$$
$$n(t) = \frac{1}{2\gamma\omega_0}\left[\frac{E - E_0}{T_1} + 2\gamma \cdot E + u(t)P\right]. \tag{11}$$

The functions (11) should provide the exponential achievability of the control goal, i.e. the maximization of the ergotropy (7).

3.2. Achievability of the control goal as $\gamma \to 0$

To analyze the achievability of the control goal, let's study the case of a week coupling between the system and the environment: $\gamma \to 0$. Suppose that:

$$\text{As } t \to \infty \; (t >> T_2): \; P \to P_* \; . \tag{12}$$

Under these conditions the system (5) could be simplified and becomes:

$$\frac{E - E_0}{T_1} = -P_* \cdot u \; ;$$
$$\frac{dQ}{dt} = P_* \; ; \tag{13}$$
$$0 = -\omega_0^2 Q - u_* \; .$$

Here u_* stands for the asymptotic control signal $u(t)$.

Let's assume that the magnitude of the control field $u(t)$ is limited: $|u| \le u_{\max}$, then we can evaluate: $Q = P_* \cdot t$ and $u = -\omega_0 P_* \cdot t$.

Finally it applies the limit for the time:

$$t_{\max} \le \frac{u_{\max}}{\omega_0 P_*} \; . \tag{14}$$

By (13) we end up with the evaluation for the ergotropy:

$$W = -T_1 P_* u = T_1 P_*^2 \omega_0 t \; , \tag{15}$$

such that by (14) finally we get:

$$W_{\max} = T_1 P_* u_{\max} \; . \tag{16}$$

Thus, the value of the ergotropy W as a result of TRF cannot increase infinitely; its upper limit is constrained with the upper limit of the control signal u.

CONCLUSIONS

The algorithm of TRF proposed here has few distinct features:

- It is universal and **does not depend on the initial conditions of the dynamical variables**.
- IT is **robust** and stable under the perturbation of the initial conditions and the relatively small external noise.
- It can be easily extended for a multi-qubit model.

The construction of the repeller in the dynamical system is natural in the frame of Kolesnikov's algorithm. Nevertheless, the construction of the dynamical attractor via the feedback loop could be performed in the frame of any optimal or suboptimal approaches: Pontryagin's optimal control, Fradkov's speed gradient, and others. Pros and cons of different approaches will be a matter of our following research.

The proposed algorithm could be applied also for different physical realizations of quantum batteries: Dicke QB, spin QB,; and for all working stages of the QB (charging, long time storage and the energy transfer to a consumption center or engine).

REFERENCES

[1]. D. Ferraro, M. Campisi, G. M. Andolina, V. Pellegrini, M. Polini, "High-power collective charging of a solid-state quantum battery", *Physical Review Letters*, vol 120(11), pp 117702, 2018.
[2]. F. H. Kamin, F. T. Tabesh, S. Salimi, F. Kheirandish, A. C. Santos, A. C. 2020. "Non-Markovian effects on charging and self-discharging processes of quantum batteries", *New Journal of Physics*, vol 22, pp 083007, 2020.
[3]. F. Dou, Y. Wang, J. Sun, "Closed-loop three-level charged quantum battery", *Europhysics Letters*, vol 131(4), pp 43001, 2020.
[4]. G. Francica, J. Goold, F. Plastina, M. Paternostro, "Daemonic ergotropy: enhanced work extraction from quantum correlations", *npj Quantum Inf.*, vol 3, pp 12, 2017.
[5]. A. Pechen, "Engineering arbitrary pure and mixed quantum states", *Physical Review A*, vol 84, pp 042106, 2011.
[6]. S. Borisenok, "Ergotropy of quantum battery controlled via target attractor feedback", *IOSR Journal of Applied Physics*, vol 12(3), pp 43-47, 2020.
[7]. A. L. Fradkov, *Cybernetical Physics: From Control of Chaos to Quantum Control*, Berlin, Heidelberg, Germany: Springer-Verlag, 2007.
[8]. A. Kolesnikov, *Synergetic Control Methods of Complex Systems*, Moscow, Russia: URSS Publ., 2012.
[9]. S. Borisenok, "Suppressing epileptiform dynamics in small Hodgkin-Huxley neuron clusters via target repeller-attractor feedback", *IOSR Journal of Mathematics*, vol 16, pp 41-47, 2020.

ICENS 6TH INTERNATIONAL CONFERENCE ON ENGINEERING AND NATURAL SCIENCE
October 21-25 2020 Belgrade

Detailed Analysis of Machine Current During Hard Turning of DIN 1.2367 Steel Using CBN

Naime Eren[1], Fatih Hayat[1], Abidin Sahinoglu[2], Mustafa Gunay[3], Halil Eren[4]

Abstract

The mechanization that started after the industrial revolution and the gradual increase in production significantly increased energy consumption. The increase in production has caused the materials used to increase and the durability of these materials to be highly demanded. The hardness of the materials has been increased by the heat treatment applied to the materials and the addition of elements. However, the increasing hardness has emerged as a problem that these materials make it difficult to process and increase their energy consumption. In this study, machine current values were measured to determine the energy consumption in the machining of hardened DIN 1.2367 hot work tool steel. Hard turning experiments were applied with CBN tool at three different values of cutting speed, cutting depth and feed rate. The significance levels of the cutting parameters on the machine flow were determined by applying the analysis of variance. As a result, it has been determined that the current value increases with the increase in the cutting parameter levels, but the energy consumption decreases due to the decrease in the machining time.

Keywords: *DIN 1.2367, hard turning, machine current, CBN*

1. INTRODUCTION

Manufacturing, which is one of the foundations of industrial application areas, has a wide scale and progresses by increasing its development and examination day by day [1]. Nowadays, the most used production method in the industrial field is turning or hard turning. Hard turning is known as a final machining method [1]. In turning; Choosing the right cutting tool, material and correct cutting parameters (feed, cutting speed and depth of cut) is extremely important [2]. Hot work tool steels are an important choice in production lately. High heat resistance and high wear and hardness of these steels are important properties. Their importance is constantly increasing as they are used in production areas such as tool steels, drills, cutting blades, deep drawing dies, punches, cutting dies and extrusion [3]. Traditionally, machining of hardened steel components has been the domain of grinding. Recently, c–BN (cubic boron nitride) tooling has proven to be a viable alternative, providing both environmental and cost benefits. c–BN tools show good performance during machining of hardened steels because of their high hot hardness, low solubility in iron, and good fracture toughness [4]. Parameters such as cutting speed, depth of cut and feed rate are very important to get efficient results in machining processes [5]. By keeping these parameters at an optimum level, it is very important to reduce energy consumption and increase energy efficiency in metal cutting methods. This will not only benefit producers economically, but also improve environmental performance [6]. In order to examine the energy consumption, attention should be paid to the measurement of the current value and its relation to the processing time.

The cases mentioned above are mainly the reasons for the cutting parameters, motor current value in hard turning process. In today's literature, the hard turning process of hot work tool steel materials is still a vital topic in modern manufacturing as the basic research into machinability.

Sahinoglu et al. Conducted hard turning tests on AISI 1040 steel with different hardnesses and examined the effects of cutting parameters and work piece hardness on surface roughness, noise level and power consumption. As a

[1] *Corresponding author: Karabuk University, Engineering Faculty, Department of Metallurgical and Materials Engineering, 78050, Karabuk/Turkey, naime.coskun@hotmail.com.*

[2] *Manisa Celal Bayar University, Technical Sciences Vocational School, Department of Mechanical and Metal Technologies, 45140, Manisa/Turkey.*

[3] *Karabuk University, Engineering Faculty, Department of Mechanical Engineering, 78050, Karabuk/Turkey.*

[4] *Cankiri Karatekin University, Cerkes Vocational School, Department of Materials and Materials Processing Technologies, 18100, Cankiri/Turkey.*

result, it showed that an increase in the feed rate value results in an increase in surface roughness, noise level and power consumption values. They stated that the amount of feed is the most effective processing parameter affecting power consumption [7]. Valera at al. researched an experimental study of power consumption and roughness characteristics of surface generated in turning operation of EN-31 alloy steel with TiN+Al2O3+TiCN coated tungsten carbide tool under different cutting parameters. The experimental setup includes five different spindle speed keeping feed rate of 0.08 mm/rev and depth of cut of 0.4 mm constant, five different feed rate keeping spindle speed of 710 rpm and depth of cut of 0.4 mm constant and five different depth of cut keeping feed rate of 0.08 mm/rev and spindle speed of 710 rpm constant. As results, the minimum power consumption of 15 watt and maximum power consumption of 495 watt was observed. Power consumption is observed to be increased when speed, feed rate and depth of cut is increased. Hence, cutting speed is observed as a critical cutting parameter, which improves surface finish, when it is increased in value. More investigation on EN 31 alloy steel is possible with further design of experimentation [8]. Bagaber et al., at this study aims to optimize machining parameters, including power consumption and the traditional machining responses of surface roughness and tool wear. Stainless steel was turned with an uncoated carbide tool under dry conditions. A multi-objective optimization method of Response surface methodology was employed to optimize machining parameters. The significant contribution of parameters was determined on the basis of compound desirability value, and optimal levels of the parameters were identified. A confirmation test was conducted to validate results. This combination of parameters resulted in the minimum power consumption of 14.94% and decreased surface roughness and tool wear by 4.71% and 13.98%, respectively. Therefore, this method also effectively reduces the effects and costs of the machining process [9]. Bhushan, at this paper presents the findings of experimental investigations into the effects of cutting speed, feed rate, depth of cut and nose radius in CNC turning of 7075 Al alloy 15 wt% SiC (particle size 20–40 μm) composite. Design of experiment techniques, i.e. response surface methodology (RSM) has been used to accomplish the objective of the experimental study. The machining parameters such as cutting speed, feed rate, depth of cut and nose radius are optimized by multi-response considerations namely power consumption and tool life. Confirmation test is also conducted to validate the test result. It is clearly shown that the multi-responses in the machining process are improved through this approach. Thus, the application of desirability function analysis in response surface methodology proves to be an effective tool for optimizing the machining parameters of 7075 Al alloy 15 wt% SiC (20–40 μm) composite. Result of this research work show that when turning is be carried out at values of machining parameters obtained by multi response optimization through desirability analysis route this will reduce power consumption by13.55% and increase tool life by 22.12% [10].

2. MATERIAL AND METHOD

In this experimental study, DIN 1.2367 material was used to examine the hard turning process. The chemical structure of the material is shown in table 1.

Table 1. Chemical composition (% by weight)

C	Si	Mn	S	P	Cr	Mo	V
0.40	0,50	0,40	0.02	0.01	5.10	3.10	0.50

The material was first heated by heat treatment at 900 ºC for 2 hours in order to reach a hardness value of 55 HRC. It was then suddenly cooled in oil. In order to remove the stresses in the cooled materials, it was kept at 300 ºC for 1 hour and cooling was performed in air. In order to understand whether the materials hardened homogeneously or not, 1 mm of sawdust was removed from the materials surfaces. Then the hardness values were measured at different points. As a result of the measurements, a hardness value of +/- 1 HRC was observed, which proved that a homogeneous hardening process was realized.

In order to prevent vibrations that may occur, the length of the work piece is adjusted to 3 times its diameter and the work piece is connected between the chuck and the center. The part is provided to rotate rigidly and without leakage. The low depths of cut in finishing turning processes necessitate the minimization of possible run-outs. Since the hardness of the materials causes high forces to occur even at low depths of cut, care has been taken to ensure that the chuck and tailstock hydraulic pressures are close to 40 bars while connecting the work piece. After the run-out on the work piece is controlled with the breaker clock, the run-out that may occur is minimized by removing 0.2 mm of sawdust on the surface.

Each experimental study was distinguished from the others by opening 2 mm wide grooves on the work piece surface. While determining the cutting parameters, firstly, tool catalog values were taken into consideration.

Afterwards, since it is a finish turning process and the surface quality is high, the cutting parameters were determined by considering the literature studies. Cutting parameters are shown in table 2.

Table 2. Cutting parameters

Factors	Level 1	Level 2	Level 3
Depth of cut (a) (mm)	0.10	0.15	0.20
Cutting speed (V) (m / min)	175	200	225
Feed rate (f) (mm / rev)	0.06	0.12	0.18

It has been paid attention that the ratio between cutting parameters is close to each other. Because while the effect rate is high for a cutting parameter that is too far in each other, the effect rate is very low for a cutting parameter that is very close to each other. After selecting the feed rate, cutting speed, depth of cut as wide as possible; the compatibility of the machine tool, cutting tool and work piece trio was tested by conducting preliminary experiments.

As cutting tool, 7125 grade CBN insert (code DCGW11T304S01020F) from Sandvik Coromant company was used. And a tool holder coded SDLCR2525M11 with 95 ° approach angle is used for this tool. In order to make the tools and the tool holder as rigid as possible, they are tightened at the recommended values and the tool holder distance is fastened as short as possible. The high tensile strength in hard materials makes it necessary not only to prefer low feed and depth of cut, but also to be rigid enough in the tool, tool holder and chuck and tailstock connection. Also, the machine tool used in the experiments is a CNC lathe with 20 HP power and 4000 rpm speed manufactured by TEZMAKSAN.

The devices used in the measurement processes were calibrated and calculated by taking the arithmetic average of three different values. UNI-T UT 201 model clamp meter is used for current value. The current flowing through one phase is taken, this value is multiplied by the voltage and time, and the power consumption required for a certain amount of metal removal is calculated. The technical characteristics of the clamp meter used in the machining experiments are shown table 3.

Table 3 The technical characteristics

Jaw Opening (mm)	28
Read	1999
Resolution (digit)	31/2
DC / AC Voltage (V)	600
DC Voltage Range (V)	0,2-2-20-200±[%0,8+1]
AC Voltage Range (V)	2-20-200±[%1,2+5]
AC Current Range (A)	2-20-200-400±[%1,5+5]
Resistance Range (MΩ)	20
Resistance Range (Ω)	200-2k-20-200-2M-20M±[%1+2]

3. RESULTS AND DISCUSSION

3.1. Evaluation of Motor Current

Current value is the most important indicator of energy consumption in the machine tool. Figure 1 shows the effects of cutting depth (a), cutting speed (V) and feed amounts (f) on motor current value.

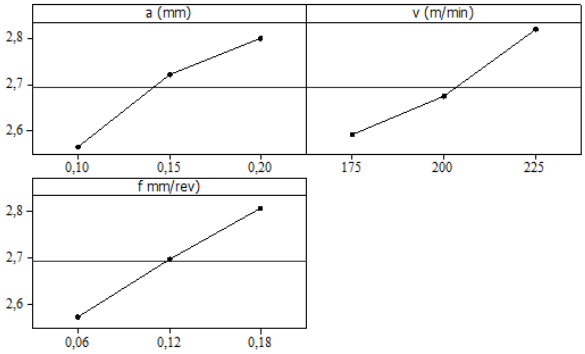

Figure 1. Graph of main effects for motor current value

Figure 2 shows the effects of the feed amount and depth of cut on the motor current value in three dimensions.

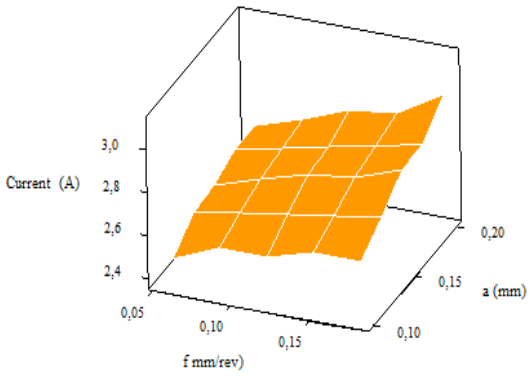

Figure 2. The effects of feed, f (mm / rev) and depth of cut, a (mm) on motor current value (A)

The current value increases with increasing feed, cutting speed and depth of cut. The increasing amount of progress causes the instantaneous current value to increase. Similarly, the increase in depth of cut caused the load amount on the machine tool to increase and the current value to increase.

3.2. Surface Response Regression: Current (A) - a (mm); v (m / min); f (mm / rev)

Analysis was done using coded units. Estimated regression coefficients for current value are shown in table 4.

Table 4. Estimated regression coefficients (A) for current value

S	PRESS	R-Sq	R-Sq (Pred)	R-Sq (Adj)
0,0152467	0,00989127	99,49 %	98,73 %	99,22 %

Table 5 shows the variance analysis for the motor current value and table 6 shows the coefficients.

Table 5 Variance analysis for motor current value (A)

Source	DF	Seq SS	Adj SS	Adj MS	F	P
Regression	9	0,774478	0,774478	0,086053	370,18	0,000
Linear	3	0,732783	0,732783	0,244261	1050,76	0,000
a (mm)	1	0,247339	0,247339	0,247339	1064,00	0,000
v (m/min)	1	0,235756	0,235756	0,235756	1014,17	0,000
f mm/rev)	1	0,249689	0,249689	0,249689	1074,11	0,000
Square	3	0,015928	0,015928	0,005309	22,84	0,000
a (mm)*a (mm)	1	0,009335	0,009335	0,009335	40,16	0,000
v (m/min)*v (m/min)	1	0,006230	0,006230	0,006230	26,80	0,000
f mm/rev)*f mm/rev)	1	0,000363	0,000363	0,000363	1,56	0,228
Interaction	3	0,025767	0,025767	0,008589	36,95	0,000
a (mm)*v (m/min)	1	0,000033	0,000033	0,000033	0,14	0,710
a (mm)*f mm/rev)	1	0,019200	0,019200	0,019200	82,59	0,000
v (m/min)*f mm/rev)	1	0,006533	0,006533	0,006533	28,10	0,000
Residual Error	17	0,003952	0,003952	0,000232		
Total	26	0,778430				

Table 6. Coefficients

Term	Coef.
Constant	3,45037
a (mm)	5,74444
v (m/min)	-0,0177111
f mm/rev)	-2,62963
a (mm)*a (mm)	-15,7778
v (m/min)*v (m/min)	5,15556E-05
f mm/rev)*f mm/rev)	-2,16049
a (mm)*v (m/min)	-0,00133333
a (mm)*f mm/rev)	13,3333
v (m/min)*f mm/rev)	0,0155556

As a result of the multiple regression analysis applied to the motor current (A) value obtained from hard turning experiments, the mathematical modeling of the motor current value is shown in equation 1.

Motor Current model for cutting tool;

$$\text{Current} = 3{,}45037 + 5{,}74444\times a - 0{,}0177111\times V - 2{,}62963\times f - 15{,}7778\times a2 + 5{,}15556E\text{-}05\times V2 - 2{,}16049\times f2 - 0{,}00133333\times a\times V + 13{,}3333\times a\times f + 0{,}0155556\times V\times f \quad (1)$$

Since the motor current value is an indicator of the power consumption and the instantaneous load on the machine, it has an important place. It is useful to know how the cutting parameters affect the motor current rating.

Motor current value increases with increasing amount of advance. Because the load on the team increases per unit time. This situation is also seen in the increase in the instantaneous chip cross section. This is an indicator of increasing cutting forces as the amount of feed increases. It is also known that the instantaneous current value is an indicator instead of the shear forces, which are expensive and inconvenient to measure. Choosing a low depth of cut in this experimental study ensures that the amount of load is low. Therefore, a small increase is observed in the flow value with the increasing amount of advance. The small range of this change in current value is effective in not choosing very wide cutting variables. Because the turning process performed is a finish turning. Low depth of cut and low feed rates are preferred.

It increases the current value a little with the increase in cutting speed. Because the increase in the number of revolutions causes an increase in the current consumed by the motor. It is known that cutting forces decrease with increasing cutting speed. Despite this, although the cutting forces decreased a little, the current value increased a little because the engine speed increased.

4. CONCLUSIONS

In this study, the interactions between current value and cutting parameters during hard turning on hardened hot work tool steel were investigated using experimental and statistical analysis. The results obtained are summarized below.

- Although the instantaneous current value increases with increasing cutting parameters, the total power consumption decreases.
- Another important parameter on total power consumption is the processing time.
- Increasing the cutting parameters is effective in shortening the processing time.
- In general, as the cutting parameters increased, the current value increased. However, the increase in the current value caused a decrease in power consumption. The main reason for this is that the increasing current value reduces the processing time. This causes a decrease in power consumption.

REFERENCES

[1]. Ozkul, "Investigation of machinability of tool steel materials with traditional and modern processing methods," Industrial Technology Education thesis, Gazi University Institute of Science, Ankara, Turkey, May. 2012.
[2]. Seremet, "Experimental analysis of the effect of vibration on surface roughness when turning the AISI 4140 molding steel with ceramic cutting tools," M. Eng. thesis, Duzce University Institute of Science, Duzce, Turkey, Aug. 2019.
[3]. C. Onur, B. Inem, "An investigation on AISI W1 and L1 steels for optimum toughness properties at low temperature (120 °C) treatment," *J. Fac. Eng. Arch. Gazi Univ.*, vol. 18,no. 1, pp. 109-124, 1999.
[4]. J. Rech, A. Moisan, "Surface integrity in finish hard turning of case-hardened steels," *International Journal of Machine Tools & Manufacture*, vol. 43, pp. 543-550, 2003.
[5]. I. Cakmak, Y. Turgut, "Investigation of the Effect of Chip Breaker Form on Surface Roughness and Cutting Forces in AISI 1040 Steel Milling," *G.U. J. Sci., Part C*, vol. 7(2), pp. 482-494, 2019.
[6]. M.P. Sealy, Z.Y. Liu, D. Zhang, Y.B. Guo, Z.Q. Liu, "Energy consumption and modeling in precision hard milling," *Journal of Cleaner Production*, vol. 135, pp. 1591-1601, 2016.
[7]. A. Sahinoglu, M. Rafighi, "Optimization of cutting parameters with respect to roughness for machining of hardened AISI 1040 steel," Material Testing, vol. 62(1), pp. 85-95, Jan. 2020.
[8]. H.Y. Valera, S.N. Bhavsar, "Experimental Investigation of Surface Roughness and Power Consumption in Turning Operation of EN 31 Alloy Steel," *Procedia Technology*, vol. 14, pp. 528-534, 2014.
[9]. S.A. Bagaber, A.R. Yusoff, "Multi-objective optimization of cutting parameters to minimize power consumption in dry turning of stainless steel 316" *Journal of Cleaner Production*, vol. 157, pp. 30-46, 2017.
[10]. R.K. Bhushan, "Optimization of cutting parameters for minimizing power consumption and maximizing tool life during machining of Al alloy SiC particle composites," *Journal of Cleaner Production*, vol. 39, pp. 242-254, 2013.

ICENS 6TH INTERNATIONAL CONFERENCE ON ENGINEERING AND NATURAL SCIENCE
October 21-25 2020 Belgrade

Modelling of Surface Roughness in Machining of The Hardened X38CrMoV5-3 Steel by CBN Insert

Naime Eren[1], Fatih Hayat[1]

Abstract

The damage to the environment is increasing day by day with the increasing industrialization and raw material consumption. Therefore, the use of more lasting materials in the industry can take to prevent this increase has gained more importance. In addition, the surface quality of many machine components used in industry affects their working life. In this context, surface quality criteria such as surface roughness and micro hardness are modeled according to the cutting parameters or processing conditions are optimized. In this study, the change of surface roughness in the machining of X38CrMoV5-3 hot work tool steel hardened using CBN tool was analyzed. The effects of cutting speed, depth of cut and feed rate on the surface roughness were evaluated by analysis of variance. In addition, the mathematical modeling of Ra was performed by applying the response surface methodology for average surface roughness (Ra). Among the cutting parameters, it was seen that the most effective parameter on the surface roughness was the feed rate. According to the developed quadratic regression model, a strong relationship was found between the cutting parameters and the surface roughness with the regression coefficient (R^2= 97.87%).

Keywords: *Hard turning, X38CrMoV5-3, surface roughness, modeling*

1. INTRODUCTION

Production methods are developing and diversifying in order to supply various requirements. During the manufacturing process, it is very important to choose the right parameters and to determine the best method to meet the targets. For this reason, it is the basic necessity of production to process at the right time, place and with data [1]. Machining stands out as the most expensive method among many production methods. In cases where competition is high, mass production, quality and economy parameters come to the fore in order to perform machining [2]. For these reasons, the material to be processed, cutting tool and cutting data should be selected very well and bad conditions that may occur during cutting should be eliminated [2]. Tool steels are generally subjected to hardening process, depending on their end use areas. Most of the steels that have been hardened are final finishing processes. This means that the cutting depths are less. Some parameters in the finishing (final finishing) processes have an important place in production. These are tolerance, size and surface quality, and the surface shape created by the machining activity and its characteristics. Results such as high production capacity, a good finishing surface, and full optimization of machining factors, tool life, low cutting forces, power consumption and dimensional accuracy are obtained with traditional manufacturing methods [3]. Recently, c - BN (cubic boron nitride) tools have been used for machining tool steels. c - BN tools perform well in machining hardened steels. This is because of their high hot hardness, low solubility in iron and good fracture toughness values [4].

The conditions mentioned above are mainly the causes of the surface roughness and quality cutting parameters in hard turning. In today's literature, basic research into the surface roughness of hot work tool steel with traditional or non-traditional machining is still a vital issue in modern manufacturing.

Jena et al. investigated the effects of different cutting parameters on the surface roughness in hard turning of AISI 4340 steel. As a result, HSLA steel surface finish provided roughness at 1.6 micron and is comparable to cylindrical grinding. Surface roughness is mainly affected by the axial advance amount [5]. Subbaiah et al.

[1] *Corresponding author: Karabuk University, Engineering Faculty, Department of Metallurgical and Materials Engineering, 78050, Karabuk/Turkey, naime.coskun@hotmail.com.*

investigated the effect of work piece hardness on surface roughness, cutting force and tool wear while evaluating the performance of the wiper ceramic cutting tip. As a result of the studies, it has been stated that the work piece hardness has a significant statistical effect on the surface roughness, cutting force and tool wear. The feed is the main cutting parameter that affects Ra and shows its effect on both tool wear and thrust. Work piece hardness (H) is the most important parameter affecting tool wear. According to the multiple optimization method; Work piece hardness of 45 HRC, cutting speed of 220 rpm, feed rate of 0.070 mm / rev and depth of cut of 0.18 mm were suggested as the best machining properties in terms of production time and cost [6]. Narayanan et al. aimed to maximize the metal removal rate (MRR) and minimize the surface roughness (Ra) by selecting the optimum turning parameters. As a result of the study, it has been reported that the most effective parameter on MRR is the depth of cut, and the parameter affecting the surface roughness of the material most is the feed rate [7]. Sahinoglu et al. investigated the effect of cutting parameters on surface roughness, vibration, sound intensity and current in the turning of AISI 4140 steel. They stated that the feed rate has the most important effect on the output parameters and this is followed by the cutting depth, while the higher the feed rate and the cutting depth, the higher the vibration, sound intensity, surface roughness and current values. As a result, they stated that the feed rate has the most important effect on the output parameters and this is followed by the cutting depth, while they stated that as the feed rate and cutting depth increase, the vibration, sound intensity, surface roughness and current values also increase [8]. Ambhore et al. investigated the effect of varying cutting parameters (cutting speed, feed rate and depth of cut) on surface roughness and vibration signals when turning hardened AISI52100 steel. The results revealed that the cutting conditions had a significant effect on the vibration signals. The acceleration amplitude Vx, Vy and Vz increases with increasing cutting speed and depth of cut. The vibration amplitude Vx, Vy and Vz initially increases as the advance amount increases, and the vibration amplitude decreases with the increase in the forward amount. While the surface roughness is greatly affected by the feed rate and subsequent cutting speed, it is less affected by the depth of cut [9]. Raj et al. used a minimal coolant application technique in this study that minimizes the use of coolant in hard turning (6-8 ml / min). Soybean oil-based emulsion has been used to make the hard turning process environmentally friendly. The oil is prepared by adding additives to increase the desired properties of the oil for hard turning. The reaction surface methodology was used for optimization of cutting parameters and estimation of surface roughness. Surface roughness was evaluated as the prediction parameter. As a result of the study, the surface roughness increased as the feed rate and depth of cut increased [10].

2. MATERIAL AND METHOD

In this experimental study, X38CrMoV5-3 material was used to examine the hard turning process. The chemical structure of the material is shown in table 1.

Table 1. Chemical composition (% by weight)

C	Si	Mn	S	P	Cr	Mo	V
0.40	0,50	0,40	0.02	0.01	5.10	3.10	0.50

The material was first heated by heat treatment at 900 ºC for 2 hours in order to reach a hardness value of 55 HRC. It was then suddenly cooled in oil. In order to remove the stresses in the cooled materials, it was kept at 300 ºC for 1 hour and cooling was performed in air. In order to understand whether the materials hardened homogeneously or not, 1 mm of sawdust was removed from the materials surfaces. Then the hardness values were measured at different points. As a result of the measurements, a hardness value of +/- 1 HRC was observed, which proved that a homogeneous hardening process was realized.

In order to prevent vibrations that may occur, the length of the work piece is adjusted to 3 times its diameter and the work piece is connected between the chuck and the center. The part is provided to rotate rigidly and without leakage. The low depths of cut in finishing turning processes necessitate the minimization of possible run-outs. Since the hardness of the materials causes high forces to occur even at low depths of cut, care has been taken to ensure that the chuck and tailstock hydraulic pressures are close to 40 bars while connecting the work piece. After the run-out on the work piece is controlled with the breaker clock, the run-out that may occur is minimized by removing 0.2 mm of sawdust on the surface.

Each experimental study was distinguished from the others by opening 2 mm wide grooves on the work piece surface. While determining the cutting parameters, firstly, tool catalog values were taken into consideration.

Afterwards, since it is a finish turning process and the surface quality is high, the cutting parameters were determined by considering the literature studies. Cutting parameters are shown in table 2.

Table 2. Cutting parameters

Factors	Level 1	Level 2	Level 3
Depth of cut (a) (mm)	0.10	0.15	0.20
Cutting speed (V) (m / min)	175	200	225
Feed rate (f) (mm / rev)	0.06	0.12	0.18

It has been paid attention that the ratio between cutting parameters is close to each other. Because while the effect rate is high for a cutting parameter that is too far in each other, the effect rate is very low for a cutting parameter that is very close to each other. After selecting the feed rate, cutting speed, depth of cut as wide as possible; the compatibility of the machine tool, cutting tool and work piece trio was tested by conducting preliminary experiments.

As cutting tool, 7125 grade CBN insert (code DCGW11T304S01020F) from Sandvik Coromant company was used. And a tool holder coded SDLCR2525M11 with 95 ° approach angle is used for this tool. In order to make the tools and the tool holder as rigid as possible, they are tightened at the recommended values and the tool holder distance is fastened as short as possible. The high tensile strength in hard materials makes it necessary not only to prefer low feed and depth of cut, but also to be rigid enough in the tool, tool holder and chuck and tailstock connection. Also, the machine tool used in the experiments is a CNC lathe with 20 HP power and 4000 rpm speed manufactured by TEZMAKSAN.

The devices used in the measurement processes were calibrated and calculated by taking the arithmetic average of three different values. During the measurement process, care has been taken to ensure that the tracer tip is perpendicular to the cutting marks and parallel to the rotation axis. Surface roughness measurement was made after the material reached room temperature. The samples to be measured were thoroughly cleaned with air. Mitutoyo Surftest SJ-201 roughness measuring device was used to measure the surface roughness value.

3. RESULTS AND DISCUSSION

3.1. Evaluation of Surface Roughness

Figure 1 shows the effects of cutting depth (a), cutting speed (V) and feed rates (f) on the surface roughness.

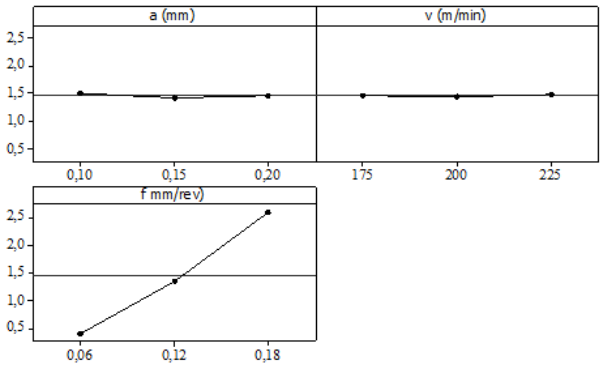

Figure 1. Graph of main effects for surface roughness

Among the cutting parameters, it is seen that the most effective parameter on the average roughness value is the feed rate. The depth of the channels on the cylindrical surface increases with the increasing amount of feed. Therefore, surface roughness values made parallel to the axis of progress also increase. Hard turning is a finish

turning process. It is aimed to obtain low surface roughness values. Therefore, it is preferred that the values of the feed amounts are low.

It appears that the cutting speed and depth of cut do not have a significant effect on the surface roughness value. While one of the most important indicators of surface quality is the surface roughness value, besides this, ovality and the formation of the white layer on the surface is undesirable. The ovality prevents the work pieces from working properly. White layer formation causes residual stresses on the surface. This layer reduces the strength of the work piece. It causes the wear resistance to decrease. Cutting speed and depth of cut have a big influence on both ovality and white layer formation. For surface quality, only low surface roughness value will not be sufficient. Low depth of cut and high cutting speeds should be preferred in order to improve other machinability properties such as ovality and white layer that affect the surface quality.

Figure 2 shows the effects of feed rate and cutting speed on the surface roughness value in three dimensions.

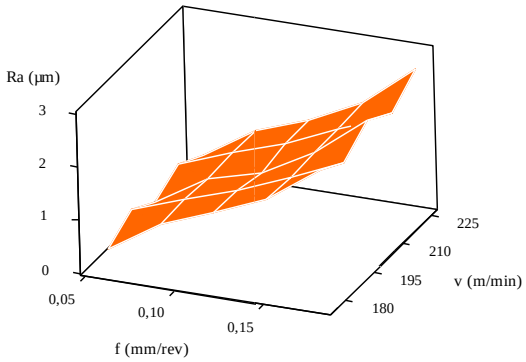

Figure 2. The effects of feed, f (mm / rev) and cutting speed, V (m / min) values on surface roughness, Ra (µm) value

The surface roughness increased with the increasing feed rate. It is seen that the cutting speed does not have a significant effect on the surface roughness value.

3.2. Surface Response Regression: Current (A) - a (mm); v (m / min); f (mm / rev)

Analysis was done using coded units. Estimated regression coefficients for surface roughness are shown in table 3.

Table 3. Estimated regression coefficients for surface roughness (µm)

S	PRESS	R-Sq	R-Sq (Pred)	R-Sq (Adj)
0,0880013	0,339870	99,40 %	98,45 %	99,08 %

Table 4 shows the variance analysis for the surface roughness and table 5 shows the coefficients.

Table 4. Variance analysis for surface roughness (µm)

Source	DF	Seq SS	Adj SS	Adj MS	F	P
Regression	9	21,8074	21,8074	2,4230	312,88	0,000
Linear	3	21,6163	21,6163	7,2054	930,43	0,000
a (mm)	1	0,0113	0,0112	0,0112	1,45	0,245
v (m/min)	1	0,0007	0,0007	0,0007	0,09	0,772
f mm/rev)	1	21,6044	21,6044	21,6044	2789,74	0,000

Square	3	0,1509	0,1509	0,0503	6,49	0,004
a (mm)*a (mm)	1	0,0196	0,0196	0,0196	2,54	0,130
v (m/min)*v (m/min)	1	0,0099	0,0099	0,0099	1,27	0,275
f mm/rev)*f mm/rev)	1	0,1214	0,1214	0,1214	15,67	0,001
Interaction	3	0,0402	0,0402	0,0134	1,73	0,199
a (mm)*v (m/min)	1	0,0147	0,0147	0,0147	1,90	0,186
a (mm)*f mm/rev)	1	0,0012	0,0012	0,0012	0,15	0,699
v (m/min)*f mm/rev)	1	0,0243	0,0243	0,0243	3,14	0,094
Residual Error	17	0,1317	0,1317	0,0077		
Total	26	21,9390				

Table 5. Coefficients

Term	**Coef.**
Constant	2,75259
a (mm)	-2,16667
v (m/min)	-0,0251111
f mm/rev)	2,27778
a (mm)*a (mm)	22,8889
v (m/min)*v (m/min)	6,48889E-05
f mm/rev)*f mm/rev)	39,5062
a (mm)*v (m/min)	-0,0280000
a (mm)*f mm/rev)	3,33333
v (m/min)*f mm/rev)	0,0300000

As a result of the multiple regression analysis applied to the Ra value obtained from hard turning experiments, the mathematical modeling of the surface roughness is shown in the equation 1.

Surface Roughness model for cutting tool;

$$Ra = 2{,}75259 - 2{,}16667\times a - 0{,}0251111\times V + 2{,}27778\times f + 22{,}8889\times a2 + 6{,}48889E\text{-}05\times V2 + 39{,}5062 \times f2 - 0{,}0280000\times a\times V + 3{,}33333\times a\times f + 0{,}0300000\times V\times f \quad (1)$$

As a finish turning process, the most important machinability parameter in hard turning is the surface roughness value. The surface roughness value is desired to be close to 0.3 microns, which is considered as the grinding quality. Such a low surface roughness value ensures efficient operation of the machine. The low friction ensures long machine life. Therefore, it is an important subject of study.

As the amount of advancement increased, the surface roughness increased. Because the increase in the amount of feed has increased the depth of the helix canals on the surface. The depth in the helix channels caused an increase in the surface roughness value. In other words, with the increase in the amount of progress, the waiting time of the tool on the surface shortened. This situation increased the difference between the height and depressions on the surface from which the chip was removed. Thus, the surface roughness value has increased.

Increasing depth of cut did not seem to have much of an effect on surface roughness. Low depths of cut are preferred in the finishing turning process. The rigidity of the material is high. Therefore, the material does not deflect in the axial direction. In addition, due to the lack of a high cutting force, no high vibration occurred. Therefore, there was no significant difference in roughness values. This is why rigid benches are preferred, especially in finishing turning processes. In finishing turning, the precision of the machine should not be impaired. When the rigidity deteriorates due to abrasions on the machine, the roughness value increases with the depth of cut.

Similar to the increase in cutting speed, there was no significant change in roughness. Because the increasing number of revolutions did not create a significant vibration on the bench. In this case, the roughness values did not deviate. Even with increasing cutting speed, decreasing cutting forces and decreasing BUE Formation provide a better cutting. This is the reason why low depth of cut and high cutting speed are preferred especially in new machines. Due to the rigidity of the machine, it does not lose its rigidity with increasing speed (cutting

speed). Pressure decreases with increasing speed. The decrease in the cutting pressure causes the cutting force to decrease. This provides a better cut. Therefore, high cutting speed and low depth of cut are preferred on new or rigid machine tools.

4. CONCLUSIONS

In this study, the interactions between surface roughness and cutting parameters during hard turning on hardened hot work tool steel were investigated using experimental and statistical analysis. The results obtained are summarized below.

- It has been observed that when tools suitable for hard turning are processed on suitable benches, a surface in grinding quality is obtained.
- The most effective parameter on the surface roughness value is the feed rate. Low feed rates are preferred for a low surface roughness value.
- Increasing depth of cut did not seem to have much of an effect on surface roughness.
- Similar to the increase in cutting speed, there was no significant change in roughness.

ACKNOWLEDGMENT

We would like to thank Assist. Prof. Dr Abidin Sahinoglu for his support during the study process.

REFERENCES

[1]. Ozkul, "Investigation of machinability of tool steel materials with traditional and modern processing methods," Industrial Technology Education thesis, Gazi University Institute of Science, Ankara, Turkey, May. 2012.
[2]. Seremet, "Experimental analysis of the effect of vibration on surface roughness when turning the AISI 4140 molding steel with ceramic cutting tools," M. Eng. thesis, Duzce University Institute of Science, Duzce, Turkey, Aug. 2019.
[3]. Kacal, "Investigation of the machinability properties at turning of heat treated Bohler K340 cold work tool steel," Advanced Technologies thesis, Kutahya Dumlupinar University Institute of Science, Kutahya, Turkey, Jun. 2018.
[4]. J. Rech, A. Moisan, "Surface integrity in finish hard turning of case-hardened steels," *International Journal of Machine Tools & Manufacture*, vol. 43, pp. 543-550, 2003.
[5]. J. Jena, A. Panda, A.K. Behera, P.C. Jena, "Modeling and Optimization of Surface Roughness in Hard Turning of AISI 4340 Steel with Coated Ceramic Tool," in *Proc. ICEMIT'17*, 2017, Vol. 2, p. 151-160.
[6]. V.K. Subbaiah, Ch. Raju, R.S. Pawade, Ch. Suresh, "Machinability investigation with Wiper Ceramic Insert and Optimization during the Hard Turning of AISI 4340 Steel," in *Proc. ICAMME'18*, 2019, Vol. 18(1), p. 445-454.
[7]. N.S. Narayanan, N. Baskar, M. Ganesan, "Multi Objective Optimization of machining parameters for Hard Turning OHNS/AISI H13 material Using Genetic Algorithm," in *Proc. IMME'17*, 2018, paper 5.2.2, p. 6897-6905.
[8]. A. Sahinoglu, M. Rafighi, "Investigation of Vibration, Sound Intensity, Machine Current and Surface Roughness Values of AISI 4140 During Machining on the Lathe," *Arabian Journal for Science and Engineering*, vol. 45, pp. 765-778, 2020.
[9]. N. Ambhore, D. Kamble, S. Chinchanikar, "Evaluation of Cutting Tool Vibration and Surface Roughness in Hard Turning of AISI 52100 Steel: An Experimental and ANN Approach," *Journal of Vibration Engineering & Technologies*, vol. 8, pp. 455-462, 2020.
[10]. A. Raj, L.D. Wins, A.S. Varadarajan, "Optimization of cutting parameters and prediction of surface roughness during hard turning of H13 steel with minimal vegetable oil based cutting fluid application using response surface methodology," in *Proc. ICONAMMA'18*, 2019, paper 01.20.23, p. 517.

ICENS 6TH INTERNATIONAL CONFERENCE ON ENGINEERING AND NATURAL SCIENCE
October 21-25 2020 Belgrade

Comparison of Power Line Communication Infrastructures

Bugrahan Uzun[1], Okan Ozgonenel[2]

Abstract

Today, the development of technology and the increase in the number of people, the industrialization and the needs of people increase the importance of electricity consumption and thus the importance of transmission lines. It is very important to bring the consumer with energy through transmission lines, the continuity of this energy and the safety of the consumer. Since the systems used are very large and interconnected, the likelihood of errors is as high. And the response given by these systems is very important both for human health and to ensure energy continuity. The wish to quickly avoid mistakes has brought about the need to communicate and send information.

In this paper, better advantageous communication method is investigated by comparing powerline communication methods. Pros and cons of PLC method and wireless communication methods are compared. After choosing PLC as the communication method, noise, channel impedance and signal weakening problems that have negative effects of data transmission over the transmission line are examined. AMS, SCADA, PRIME, G3 methods were compared. Modulation methods that may be suitable for transmission line communication are compared. Transmission line communication system simulation is designed with BPSK modulation method. The carrier signal, which is at very high frequencies compared to the 50Hz frequency network signal transmitted over the transmission line, is modulated with the BPSK signal. The information signal to be transmitted is sent via BPSK modulation over the transmission line. At the transmission line output, the demodulation process is applied and the information signal at the input is read at the output. PSIM is used for computer simulations and performance curves are evaluated over different PLC modulation techniques.

Keywords: *Power Line Communication, Distribution Lines, Transmission Lines, Power Quality*

1. INTRODUCTION

Rapid increase of technological developments in our country today, provides the infrastructure for studies on the use, security and analysis of powerlines. In our age there is a need for fast communication, apart from the need for a house or device where only electricity was transmitted. This situation creates an environment for a faultless, continuous and efficient energy to reach the consumer. In addition to technological developments, the increased day by day. Besides, the need for electrical energy in all areas, especially the production sector, service sector and telecommunication sector, is increasing day by day.

The use and dissemination of radio frequencies have played a major role in the development of communication. The advantages and disadvantages of two different communication methods, wired and wireless, have been examined and applied according to the area of use and purpose. Information exchange over energy transmission lines, which have a low cost effect in wired communication, emerged in the 1800s with the studies of the scientists of the period and has reached to the present day.

The data signal to be transmitted in the exchange of information over the powerline is superimposed with the help of high-frequency carrier signals and applied to the energy transmission line. The signal transmitted over the transmission line is then filtered with the help of filters and the information signal is seen on the receiver

[1]*Corresponding author: Ondokuz Mayis University, Department of Electrical and Electronics Engineering, 55270, Atakum/Samsun, Turkey.* *bugrauzun55@hotmail.com*
[2] *Ondokuz Mayis University, Department of Electrical and Electronics Engineering, 55270, Atakum/Samsun, Turkey.* *okanoz@omu.edu.tr*

side. By this way, communication takes place. Since the transmission line cabling had already been done, one of the biggest advantages of the communication system over the energy transmission line is that it is an economical method since there is no need for wiring.

2. PLC NEGATIVE EFFECTS

The main problems of powerline communication are noise, channel impedance and signal reduction. Information exchange for powerlines has a destructive channel effect. Changing impedance and noise cause the impact of communication to be questioned and to lose its importance. Therefore, it is required to propose a new solution to the three-way relationship depending on time, speed and signal level. Noise, channel impedance and signal weakening are examined below.

2.1. Noise

Powerline communication or any type of communication, with the help of signs sent and received information between the receiver-transmitter is available. These systems act according to the command sent with the help of signs. Differences that may occur on the sent signmay cause the system to run incorrectly. Noise is one of these differences. When the signal and noise come together, the negative effects it creates will prevent the power line communication from working properly.

Depending on the size of the noise, the disruptive effect on the sinusoidal wave increases. Increasing the disruptive effect is undesirable. It damages the functioning of the communication system. The effect of noise should be reduced as much as possible. When we apply 5- times to sinusoidal wave in MATLAB program, the changes that occur to the sign are seen in Figure 1 and Figure 2.

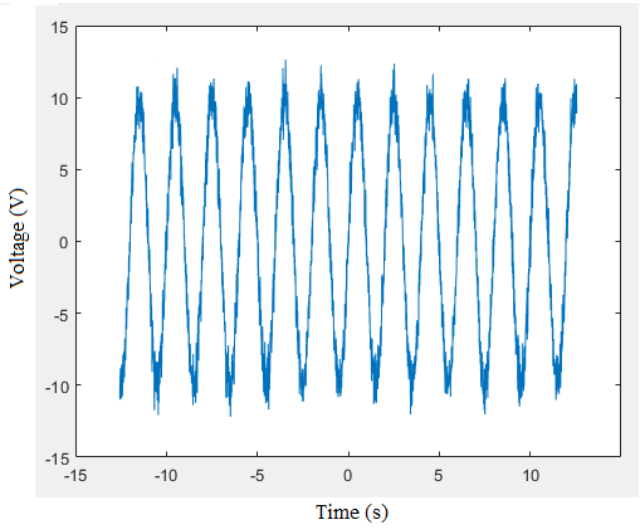

Figure 1. One way noiseless

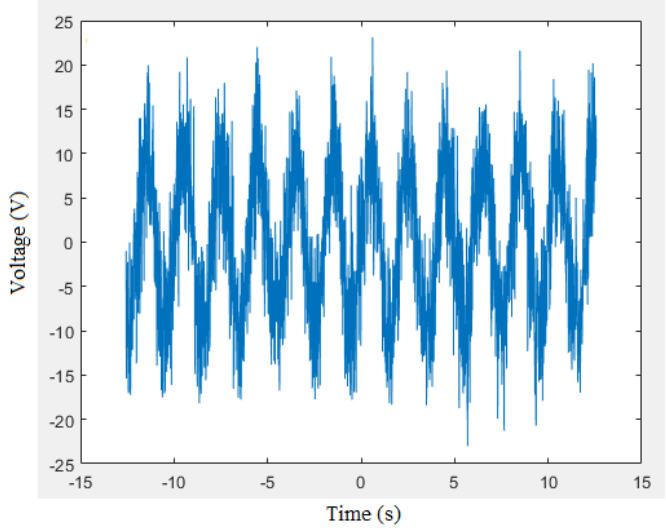

Figure 2 One way 5 times noise

As a result of the application in MATLAB program, the effect of the sinusoidal wave was observed by increasing the noise ratio. As the noise increased, as expected, there were distortions in our mark. The louder the noise, the more distortion on the signal. In the exchange of information, the system is more confused. This can lead to security weakness.

2.2. Channel Impedance

The electricity grid is quite complex and brings together many systems simultaneously. The imbalance in channel impedance caused by system-connected loads and distribution elements makes it difficult to exchange information. The imbalance that comes to the challenge in the channel impedance negatively affects the signal strength in the output. This causes afailed communication environment between the informational and the receiver. In order to investigate the effect of channel impedance disorder on the sign, in urban and industrial areas, CENELEC in Turkey, B, a series of measurements between 10 and 170 kHz bands C and D were obtained. Based on these measurements, 3-17 Ω in rural areas, 1-17 Ω in urban areas and 1-21 Ω in industrial areas were determined . in addition, signal weakening in these bands was found to be 4-30 dB when looking at phase-neutral, phase-earth and neutral-earth measurements for different power lines. The output ports and modem output impedance and power line input impedance must be mapped appropriately for the transfer of power between the power line and IHH. For an efficient modem design, the power line impedance must be known. Power line impedance varies according to the location of the power lines. Time impedance depends on many factors, including loads on transmission lines,day or night power leps. Therefore, bands, sign levels and procedures have been determined in Europe and CENELEC, EN-50,065-1 has emerged.

2.3. Signal Reduction

On the transmission line, there may be differences between the signal sent from the input and the signal received from the output, and deterioration of the signal quality may occur. The main causes of disturbances on the power line are as follows.

- Transmission Stage Type
- Transmission Speed
- Communication Distance

The reasons for distortion of the transmission are as follows.

- Signal Weakening
- Restricted Bandwidth
- Delay Corruption
- Noise

Signal reduction occurs by decreasing signal strength depending on communication distance. Solution can be provided by using signal booster or repeater. This change in signal level can be shown as in equation (1).

$$dB = 10log\left(\frac{Signal\ Output\ Power}{Signal\ Input\ Power}\right) \quad (1)$$

If we talk about the effect of noise on the signal, the most important criterion is the SNR shown in equation (2). The following formula is used to understand how much the sign is weakened. Signal reduction is 100 dB per kilometer for LV lines and 10 dB per kilometer for MV lines. The more signal reduction is seen in Low Voltage networks. By using repeaters at distances less than 1 km, signal reduction is prevented.

$$SNR(dB) = 10log\left(\frac{Signal\ Power}{Noise\ Power}\right) \quad (2)$$

3. QPSK-BPSK MODULATION METHODS AND SIMULATION

The process of changing the information mark to be forwarded according to the transmission environment is called "Modulation". A low-frequency information mark to be transmitted over the power line needs a high-frequency carrier signal. The effect of frequency on transmission occurs in long-distance transmission of information.

Digital superimposition techniques are based on switching logic. Depending on the information sign to be transmitted, information transmission is provided by switching which carrier will be on and which carrier will be closed. The conversion of information expressed as a number into an analog sign is called "Numerical Modulation".

3.1. QPSK Modulation

QPSK modulation is a type of numerical modulation. PSK enters the modulation class. The process of transmitting the logic1 and logic0 information given by the 2-bit information signal to be transmitted at the input with the help of four different and high frequency carrier signals with 90 ° phase difference between them is called QPSK modulation. The carrier phase angles connected to the information sign bits are included in Table 1.

Table 1. QPSK Data Signal Bits and Carrier Signal Phase Angels

BIT	PHASE
00	45°
01	135°
10	225°
11	315°

The four carrier signs with 90 ° phase difference between them are high frequency sinus signs named as 00, 01, 10, 11 as seen in Figure 3.

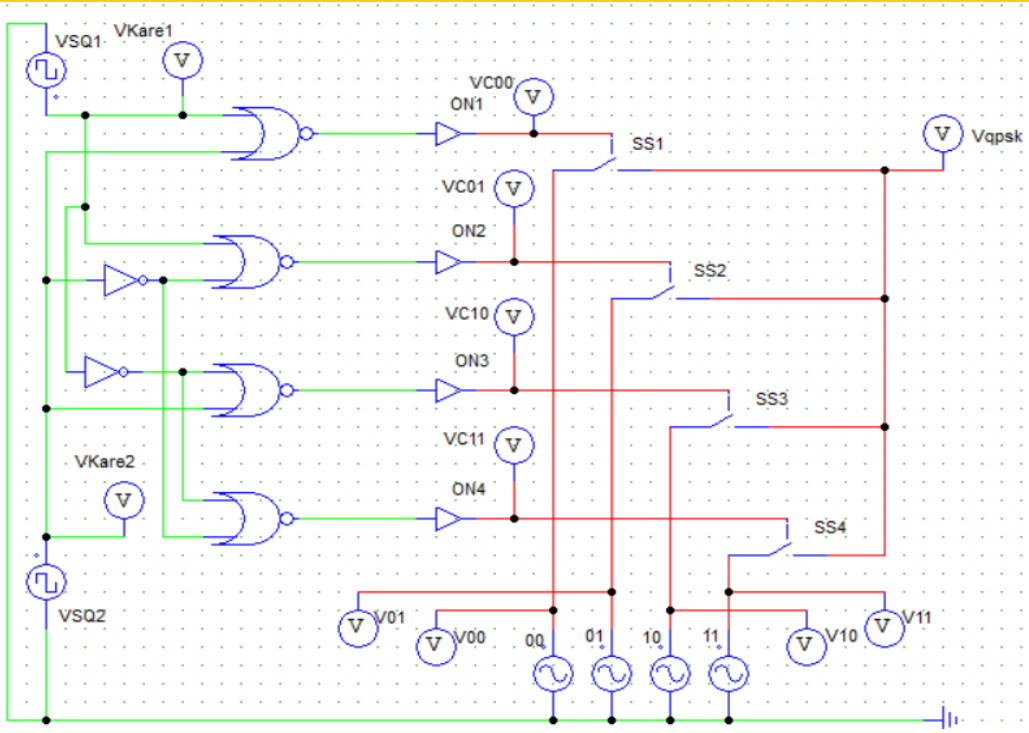

Figure 3. QPSK Modulation Circuit on PSIM

The carrier signal chart simulated in the PSIM program is as follows.

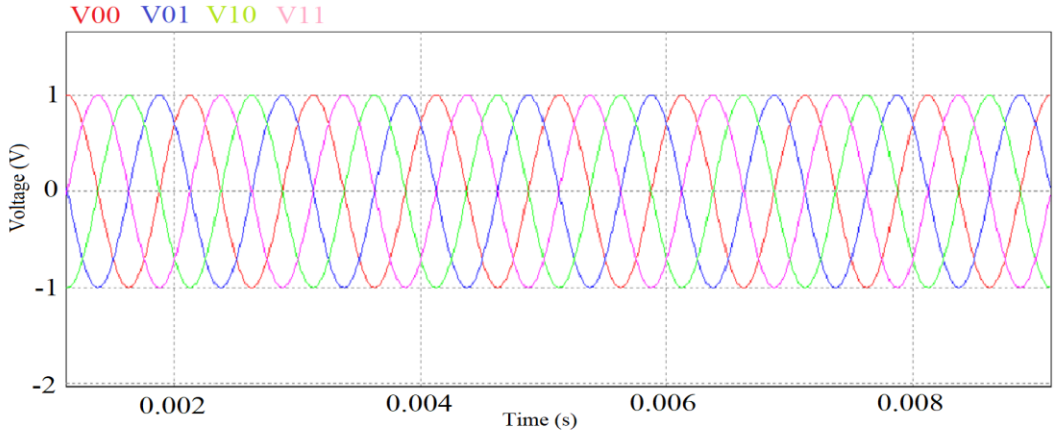

Figure 4. 90° Phase Angel High Frequency 4 Carrier Signal on PSIM

Depending on the 1 or 0 status of the information to be ed, only one of the carrier signs is turned on and the others are closed, with the help of switching the mark from 1 to 0 and 0 to 1 of the mark coming out of 2 different square waves. Thus, only one superimposed sign is seen. In Figure 3, this switching is provided with the help of ON and SS elements, and the Vqpsk signal is seen in Figure 5.

As seen in Figure 3, four different carriers are activated and deactivated according to the 1 and 0 states of the elements Vkare1 and Vkare2. The open-closed state of the carriers switched by square waves is shown in Figure 4. When examined in certain time frame intervals, only one carrier is active for each second interval. Information transmission is carried out by that carrier for the time intervals during which carriers are active.

This is how Vqpsk is working for the modulation method. Table 2 and Figure 5 has a QPSK modular output mark.

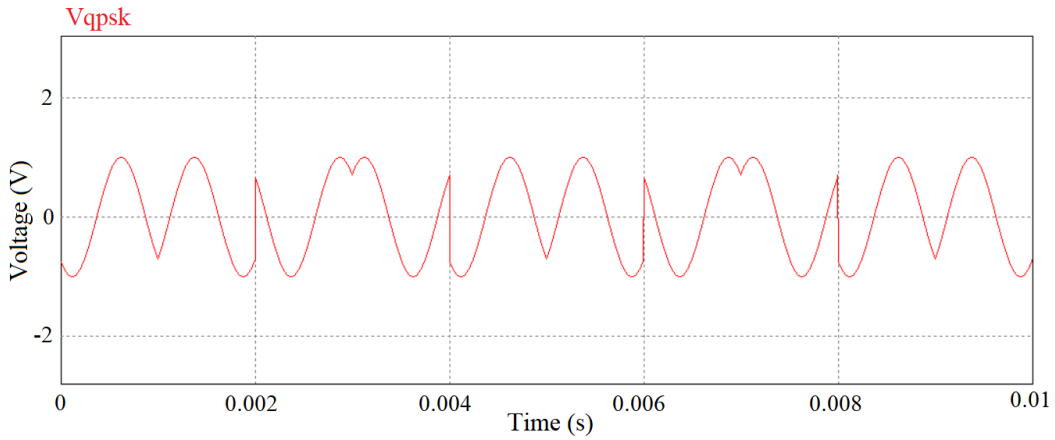

Figure 5. QPSK Modulation Output Signal on PSIM

4. BPSK MODULATED POWER LINE COMMUNICATION SIMULATION

We will carry out the data transmission with BPSK modulation with the circuits we have built on PSIM. BPSK, which is treated with switching logic, will be provided by in and out of the open-closed state of carriers with different phase angle and the same frequency. Thus, continuity will be provided in the information mark to be transmitted and a healthy communication will be made.

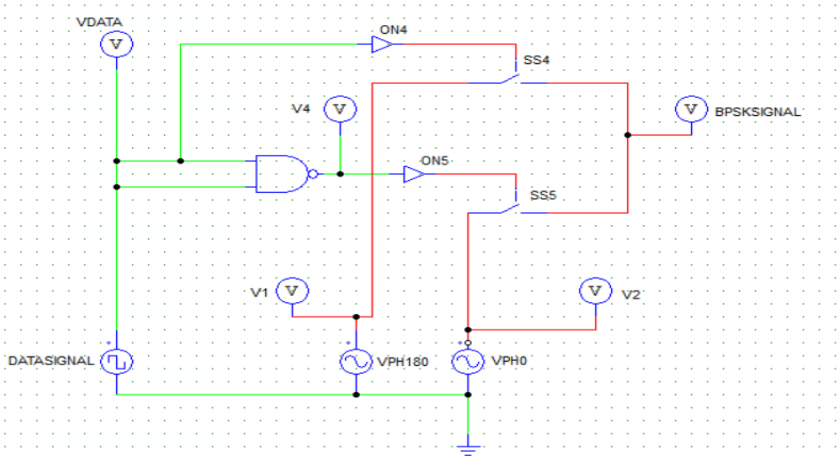

Figure 6. BPSK Modulation Circuit on PSIM

The data signal to be transmitted in the circuit above has a frequency of 1 Volt and 100 Hz. The VPH180 is a carrier signal with a phase angle of 10000 Hz 180°. Our other carrier signal is the VPH0, a carrier signal with a phase angle of 10000 Hz0°. With the NAND gate in the circuit, the data signal creates the modular signal by switching according to the status of 1 and 0.

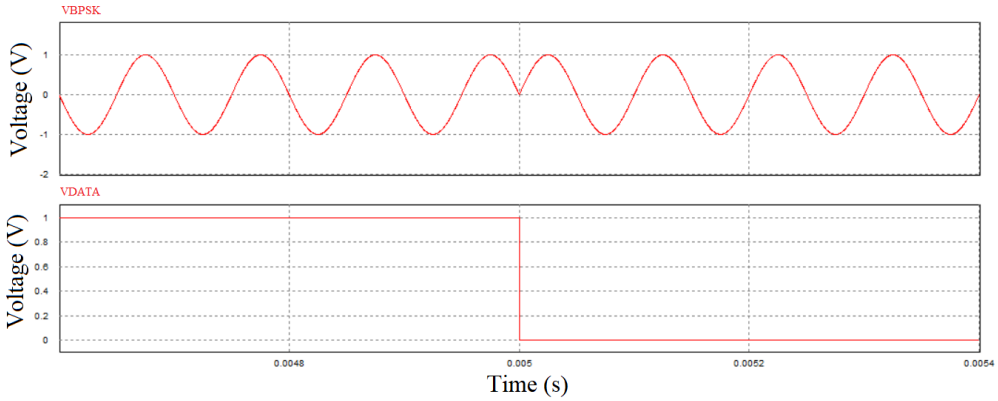

Figure 7. Data Signal and BPSK Modulated Signal

The combination of 2FKA superimposed data signal and grid signal is applied to the transmission line. The shape of the signal passing over the Vihson voltage probe after its transmission over the transmission line is as follows.

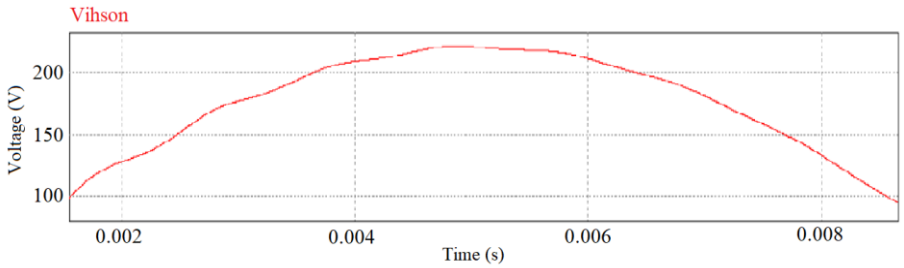

Figure 8. Power Line Output Signal

Since the BPSK signal is a very high frequency sign, it shows faster and shorter changes on a 220 Volt and 50 Hz grid signal. Therefore, it is observed that it creates small fluctuations on the network signal. The data signal is transmitted over the power line after BPSK modulation. However, the system cannot detect the function of the signal and does not work because the signal that appear from the power line output is over-boarded. For this reason, the superimposed signal at the exit of the transmission line must go through the decomposition process and return to the square wave format. Thus, the system continues to run by getting the correct input-output information. BPSK sign demodulation circuit is as follows.

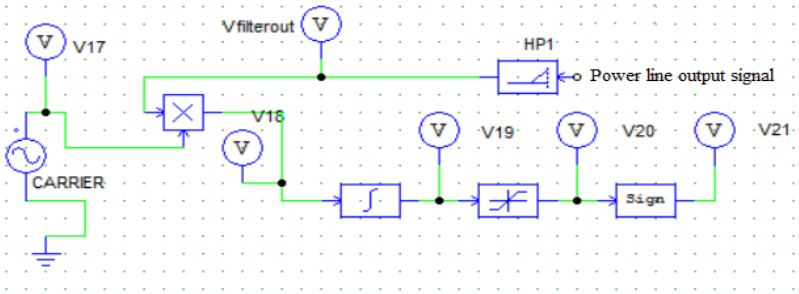

Figure 9. BPSK Demodulation Circuit

The signal from the power line is filtered with the help of a high pass filter. Then, the separation process is completed by taking integral and derivative functions of the mark combined with the carrier signal, respectively. At the beginning of the circuit, the desired square wave, at the end of the circuit with the demodulation process will find its own form.

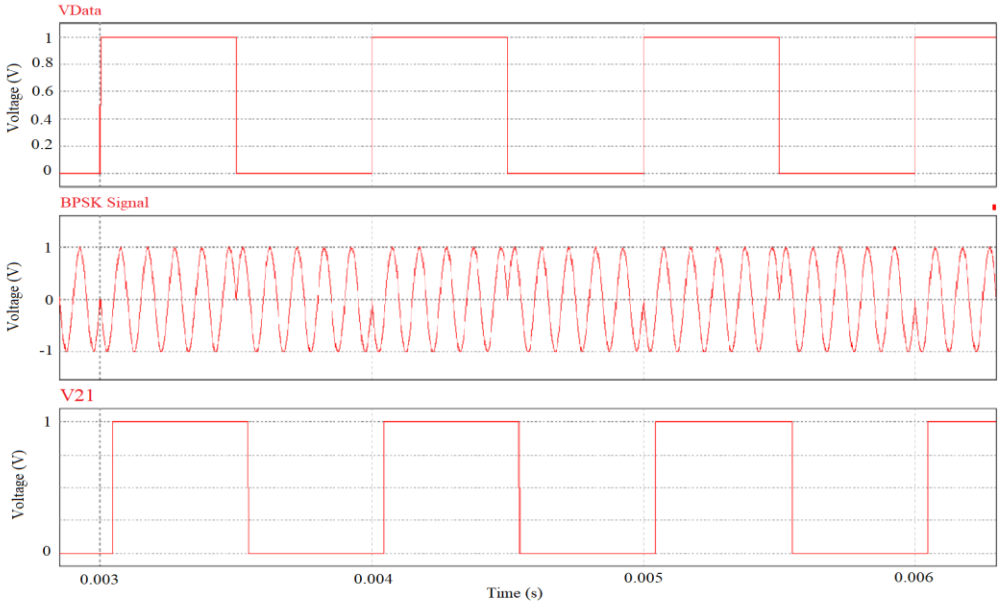

Figure 10. Input Data Signal, BPSK Signal and Output Data Signal

5. RESULT AND DISCUSSION

In this study, studies on power line communication, application areas, negative effects that may be encountered during transmission and thrust techniques have been examined. In this context, simulation studies that can set an example for power line communication have been done. For this purpose, the advantages and disadvantages of IHH applications compared to each other were compared. Transmission line communication applications are separated according to many characteristics. The pros and cons of AMS, SCADA, PRIME and G3 power line communication methods are examined below.

AMS is a remote meter reading application. With AMS, consumption values on the counter can be read remotely. If we look at the pros, personnel expenses have been reduced with this application. Reading consumer consumption values is done more accurately without allowing human error. Missing fugitives can be tracked. Cons, on the other hand, cannot provide control along the power line. It cannot analyze the entire power line system between the source and the consumer. It cannot predetermine the interruptions that may be caused by line protection elements and provide an instant solution. It cannot offer improvement by matching and comparing the information received from the meters with each other. It cannot locate fault. It cannot keep records because it cannot detect malfunctions.

The SCADA system is a central inspection and information collection application in which complex system transmission lines are managed from a single center. It can switch on and off remotely. In case of line failure, it can control the feeding of the transmission line from a different place. It can instantly monitor all consumers and feeders along the power transmission line. The malfunction can be located. It can keep track of where and when the fault occurred. When we examine these features, it can be seen that the SCADA system is much superior to the AMS system.

G3 and PRIME have more developed features than SCADA and AMS. Scada is an energy monitoring system. Compared to SCADA, G3 and PRIME are superior because it works based on PLC. It can make more detailed power line analysis. It can create and apply different solution scenarios according to the failure situations that may ocur.

G3 power line communication system emerged after the PRIME system. G3, one of the new technologies of the last period, has similar features to PRIME. Remote on-off and line fault location detection. It is able to control all systems along the power line by doing network analysis. It can prepare different consumer feeding scenarios depending on the on-off situations of the protection elements for each failure situation. G3

transmission speed is slower than PRIME. More G3s are preferred for long-distance transmissions as a plus of noise resistance. PRIME has more transport channels than G3. G3 uses the IPv6 package. PRIME uses the IPv4 package. Therefore, G3, which uses an IPv6 package, provides a more secure network environment than prime. The G3 can find up to 36 different transport channels, while PRIME can have 96 different transport channels. This allows larger data to be sent through different channels in terms of data submission. In terms of noise resistance, the G3 is more advanced. The G3 system has more noise resistance than the PRIME system. This provides a win for communication over long distances. G3 is more stable than PRIME. The priority in the powerline is to maintain the communication more stable. Therefore, G3 is more preferred than PRIME.

REFERENCES

[1]. Chariag, D., Guezgouz, D., Raingeaud, Y., Lebunetel, C., "Channel Modeling and Periodic Impulsive Noise Analysis in Indoor Power Line", IEEE, 2011
[2]. Achaichia, P., Le Bot, M., Siohan, P., "Potential Impact of the CENELEC Spectral Mask on Broadband PLC Networks", IEEE, 2013
[3]. Al-Mawali, S., Al-Qahtani, S., Hussain, M., "Adaptive Power Loading of OFBC-Based Power Line Communications Impaired by Impulsive Noise", IEEE, 2010
[4]. Adeyemi, A., Emanuel, O., "An Agent-Based Adaptive BPSK/QPSK Modulation for Rice-Longnormal Channel", IEEE, 2007
[5]. Chehri, A., "A Low Complexity Turbo Equalizer for Power-Line Communication with Applications to Smart Grid Networks", IEEE, 2019
[6]. H. Meng, S. Chen, Y. Guan, C. Law, P. So, E. Gunawan, et al., "Modeling of transfer characteristics for the broadband power line communication channel", *IEEE Trans. Power Del.*, vol. 19, no. 3, pp. 1057-1064, Jul. 2004
[7]. Sharma, A., Majumdar, S., Naugarhiya, A., Acharya, B., Majumder, S., Verma, S., "VERILOG Based Simulation of ASK, FSK, PSK, QPSK digital Modulation techniques", I-SMAC, 2017
[8]. Ustun Ercan, S., Ozgonenel, O., W. P. Thomas, D. "Power line communication channel for smart grid", Smart Grids and Cities Congress and Fair (ICSG) 2018 6th International Istanbul, pp. 208-212, 2011
[9]. Yadav, P., Saini, L., "Powerline FSK Communication Using Signal Wire Technique", IEEE, 2017
[10]. Washiro, T., "Applications of RFID Over Power Line for Smart Grid", IEEE, 2012
[11]. Zheng, X., Tao, Y., "Analysis on using transmission lines travelling wave fault location based on fault information system", IEEE, 2011

ICENS 6TH INTERNATIONAL CONFERENCE ON ENGINEERING AND NATURAL SCIENCE
October 21-25 2020 Belgrade

Forecasting Automobile Sales using Winters Method Optimized by Genetic Algorithm

Mustafa Ahmet Beyazit Ocaktan[1], Aslan Deniz Karaoglan[2]

Abstract

The Winters method is a multi-factor demand forecasting method used when time series data show trend, seasonality and level (shift). In demand forecasting methods that use exponential smoothing like the Winters method, the estimation of smoothing parameters and initial values is a basic requirement. In this study, it is aimed to optimize the Winters smoothing parameters with genetic algorithm (GA), and thus, to improve the forecasting performance. This problem was modelled as a multi-objective continuous optimization problem by means of regression, and then GA is applied to calculate the optimum parameter values to perform prediction with good accuracy. In the modeling phase, the regression models between the factors (winters parameters) and the responses (mean absolute percentage error - MAPE, mean absolute deviation - MAD, sum of squared error - SSE, mean squared error - MSE, and root mean squared error - RMSE) are derived, and then GA is applied to minimize the sum of weighted responses. Preliminary experiments were done on various Winters parameters by using Minitab-16. Also the mathematical modeling is performed by using Minitab-16 and then the GA optimization is performed by using Matlab. The developed method was applied on the vehicle sales data of an automobile manufacturer, and the reliability of the proposed method was tested. This study has two motivations: (i) testing the effectiveness of Winters method for car sales forecast problem, and (ii) investigate how the performance of the Winters method has changed with the use of GA. The results show that the optimization by using GA with selected weighted responses can be successfully applied to optimize the Winters parameters and significantly improves the method's forecasting performance.

Keywords: Automobile Sales, Forecasting, Winters Method, Regression, Genetic Algorithm, Optimization.

1. INTRODUCTION

When the automotive industry is evaluated in terms of the economic results it creates, it is accepted as a leading industry branch in the development of the country's economies. Especially in addition to the main industry, the economic liveliness caused by countless sub-industry organizations and distributor dealers has provided the automotive industry with a wide range of development plans for many countries. Rapid development in the automobile industry in the past quarter century; while causing the production capacities of automobile companies to expand blindly, brought the question of how much demand will be received from its suppliers. Incorrect sales forecast means inaccurate capacity planning, which means inefficient use of limited production resources. Accurate forecasting of car sales is crucial in creating strategies for car manufacturers and distributors. It also has a certain impact on the healthy development of countries' car market. Automobile demand shows an increasing trend over time with population growth and socio-cultural effects. In addition, it may increase or decrease seasonally in certain periods of the year. Besides these two effects; further downward or upward shifts in demand can be observed as a result of the effects of price discounts, price increases, introducing new models to the market, etc. As a result of these very different effects, besides the trend, seasonality and sliding effects, a complex data set emerges with the effect of many socio-economic or social-cultural factors that cannot participate in the model. Based on this complex data, it is a difficult mathematical and statistical problem to make automobile sales forecasts for future periods. When the literature is examined, many studies are presented for the solution of this complex forecasting problem. Jun & Qing [1] used back

[1] *Balikesir University, Department of Industrial Engineering, 10145, Cagis Campus/Balikesir, Turkey, ocaktan@balikesir.edu.tr*

[2] *Corresponding author: Balikesir University, Department of Industrial Engineering, 10145, Cagis Campus/Balikesir, Turkey, deniz@balikesir.edu.tr*

propagation neural network (BPNN) to forecast the automobile sales. They used GA to optimize the parameters of BPNN. Fantazzini & Toktamysova [2] proposed multivariate nonlinear models to forecast monthly car sales data using economic variables and Google online search data of ten car brands in Germany. Vahabi *et al.* [3] proposed a sales forecasting model in Iran automotive industry (for Saipa group) using adaptive neuro-fuzzy inference system and GA. Gao *et al.* [4] proposed a hybrid method (HPA) based on particle swarm optimization (PSO) and ant colony optimization (ACO) to forecast automobile sales of China. They used mean absolute error as the performance criteria. Fleurke [5] presented an ensemble forecast method that is based on averaging the outcomes of several forecasting methods such as exponential smoothing, autoregressive integrated moving average, artificial neural networks (ANN), vector auto regression, theta, random forest, generalized linear model, naive seasonal. Chen *et al.* [6] presented a study on sales forecast of R brand car. They collected the related online reviews data, through the natural language processing and the text emotion model. Ceylan *et al.* [7] presented a study on modeling and forecasting car ownership in Turkey. They used various factors such as gasoline price (GP), car price, gross domestic product (GDP) per capita, and number of employees and performed mathematical modeling using multiple nonlinear regression analysis. Kaya *et al.* [8] performed automobile sales forecasting for Turkey using ANN, ARIMA, and time series decomposition.

This paper provides some useful information about forecasting automobile sales to the related readers. There are many studies in the literature about the effective forecast of automobile sales. In this study, different from the studies in the literature, automobile sales forecast has been made with the Winters method. By this way, it is aimed to show to the reader that the effectiveness of the Winters method. Winters method is an effective method for performing forecasts on time series. The method has 3 parameters, each of which takes continuous values in the range of 0-1 (alpha, gamma, delta). However, there are numerous combinations of these parameters and the values chosen for the parameters seriously affect the method's estimation performance. Therefore, we have optimized the parameters of the Winters method by using GA.

In the related literature, Winters method optimized with GA is used in the following studies to perform forecasts on the given time series data. Azmi [9] used the GA to determine the parameters in the estimation of monthly tourist arrivals with the Winters method, and aimed to minimize only the mean absolute percentage error (MAPE) criterion. Eusébio *et al.* [10] used the binary GA to determine the parameters with the metaheuristic approach in the Holt-Winters electricity short-term load forecast, and aimed to minimize only the mean squared error (MSE) criterion. In a similar study, Akpinar & Yaz [11] used the GA to determine the parameters in the electrical load estimation with the Winters method, and aimed to minimize only MAD error criterion. Peng *et al.* [12] used GA using the sharing function between individuals in the group, and thereby reducing the likelihood of selecting similar individuals in the population for parameter determination in the predicting expressway subsidence with the Holt-Winters model. In this study, it is also aimed to minimize the mean absolute deviation (MAD) criterion. In the literature, no other study using Winters optimized with GA is used to model and make an effective estimation of a complex dataset showing different oscillations in all directions under the influence of many external factors such as automobile sales forecast problem. This is the novelty of this work.

In this study, Winters sales forecasts were made with Minitab statistical package program for many different alpha, gamma, delta parameter combinations (factors). Mean absolute percentage error (MAPE), mean absolute deviation (MAD), sum of squared error (SSE), mean squared error (MSE), and root mean squared error (RMSE) outputs are calculated as performance criteria (responses) that show how close the estimates are to the observed forecast values. The relationship between these inputs and outputs are modeled by regression equations. These regression equations are used to optimize the parameters of Winters method with GA to find the combination of inputs that gives the best forecast performance. Selected performance criteria affect the optimization results and forecast performance of Winters method. Whichever optimization method is chosen, the performance criteria selected and the way they are combined affect the Winters parameter values found after the optimization and the accuracy of the forecasts made with these parameter values. In the optimization phase with GA, we used multi-objective optimization and we combined several error criteria under the fitness function of GA by weighting them. The aim of this study is to show readers which performance criteria are effective to increase the effectiveness of the Winters method and how to optimize parameter optimization using one of the nature-inspired algorithms, the GA.

This study has 2 different motivations. The first motivation is to test the effectiveness of Winters method for automobile sales forecast problem, instead of using regression models (between sales and economic indicators) or time series regression for the sales that are widely presented in the literature. In the literature, single error criteria (MAD, MAPE, or MSE) were widely used in studies in which winters parameters were determined by GA. In this study we used 5 different performance criteria by combining them. The second motivation is to

show the reader how the performance of the Winters method has changed with the use of a nature-inspired heuristic such as GA to provide a large number of performance criteria together (minimization of MAD, MAPE, SSE, MSE, and RMSE). For this purpose, Winters method was employed to forecast the number of Fiat brand automobile sales in Turkey between 2011 and 2020 years. A dataset that includes number of commercial vehicle sales of Fiat brand held in Turkey constitute the data set for this study.

2. MATERIALS AND METHODS

2.1. Winters Method

Winters method is an exponential smoothing method commonly used for estimating time series data that includes level (shift), trend and seasonality. The origin of the method is Winters [13], but it is an extension of Holt [14]. Winters method requires the estimation of three smoothing weights for level, trend and seasonality portions of the data, and therefore the method is considered as a three-parameter forecasting method. In exponential smoothing methods, smoothing parameters are generally estimated based on the first part of the time series data, and what the parameters will directly affect the quality of the forecasting. There are many search methods in the literature to determine these parameters to minimize the forecast error.

Winters method is used when data shows level, trend and seasonality. There are two main models in time series: additive and multiplicative. In the additive model, different components affect the time series as additive and in the multiplicative model proportionally. According to whether the time series model is additive or multiplicative, the model underlying the Winters method is given as follow:

$$x_t = (a + bt) I_t + \varepsilon_t \quad \text{(multiplicative model)} \tag{1}$$

$$x_t = a + bt + I_t + \varepsilon_t \quad \text{(additive model)} \tag{2}$$

where x_t is time series data for the period t; a, level; b, linear trend; I_t, seasonality index for the period t and ε_t, forecast error (mean= 0 and variance=σ^2). Updating equations for the multicaptive model are given below [15]:

$$L_t = \alpha \frac{x_t}{I_{t-P}} + (1-\alpha)(L_{t-1} + b_{t-1}) \tag{3}$$

$$b_t = \gamma (L_t - L_{t-1}) + (1-\gamma) b_{t-1} \tag{4}$$

$$I_t = \Delta \frac{x_t}{F_t} + (1-\Delta) I_{t-P} \tag{5}$$

where L, b_t and I_t indicate average level, trend and seasonality forecasts respectively; α, γ, ∇, smoothing parameters; P, the number of seasons. The term (x_t / I_{t-P}) in Equation (3) shows the forecast of the seasonally adjusted current value in the period t. The $(L_t - L_{t-1})$ difference in Equation (4) provides an estimate of the current trend in the period t, and The term (x_t / F_t) in Equation (5) provides a seasonal factor estimate based on the last observation value. The forecast for the next period is $f_{t+1} = (L_t + b_t) I_{t+1-P}$. The forecast of more than one period can be determined from Equation (6) given below:

$$f_{t+r} = (L_t + r b_t) I_{t+r-P}, \qquad 1 \le \mathrm{r} \le \mathrm{P} \tag{6}$$

Forecast error measurements of MAD, MAPE, SSE, MSE, and RMSE are used in this study for performance criteria. The formulas of these measurements are as in Equations (7-11), respectively [15, 16]:

$$MAD = \frac{1}{\mathrm{n}} \sum_{t=1}^{\mathrm{n}} |x_t - \hat{x}_t| \tag{7}$$

$$MAPE = 100\frac{1}{n}\sum_{t=1}^{n}\frac{|x_t - \hat{x}_t|}{x_t} \quad (8$$

$$MSE = \frac{1}{n}\sum_{t=1}^{n}(x_t - \hat{x}_t)^2 \quad (9)$$

$$SSE = \sum_{t=1}^{n}(x_t - \hat{x}_t)^2 \quad (10)$$

$$RMSE = \sqrt{\frac{1}{n}\sum_{t=1}^{n}(x_t - \hat{x}_t)^2} \quad (11)$$

Where $\hat{x}_t$ indicates forecast of the observation value for period t; $x_t - \hat{x}_t$, forecast error realized for period t; n, number of forecast. In this study, forecast error measurements of MAD, MAPE, SSE, MSE, and RMSE used as performance criteria in Winters model are obtained from regression equations. In the following section, regression modeling will be detailed.

2.2. Regression Modelling

In this study, performance criteria (MAD, MAPE, SSE, MSE, and RMSE) observed against different combinations of alpha, gamma and delta parameters (factors) were calculated with the Minitab statistical analysis program. Then, regression equations were established showing the mathematical relationship between these factors and the performance criteria measured as response, and then GA realized to minimize these responses by using the generated regression equations. After several modelling and simulation phases it is considered to use general full quadratic regression model. Equation (12) represents the general full quadratic regression model [17]:

$$Y_t = \beta_0 + \sum_{i=1}^{n}\beta_i X_{it} + \sum_{i=1}^{n}\beta_{ii} X_{it}^2 + \sum_{i<j}^{n}\beta_{ij} X_{it}X_{jt} + e_t \quad (12)$$

In this model, Y_t is the response value observed at time t, X_{it}'s are the i^{th} factor at time t. Terms β are the regression coefficients. e_t is the prediction error that is observed at time t (Silver 1998). The matrix notation for this model is given in Equation (13) [17]:

$$Y = \beta X + \varepsilon \quad (13)$$

Y is a vector that is composed of the observed responses. X represents the input matrix and ε is the matrix of residuals. Coefficients of the regression equation are given in β vector and calculated by using the Equation (14) [17].

$$\beta = (X^T X)^{-1}(X^T Y) \quad (14)$$

Coefficient of determination (R^2) measures the ability of the factors in the regression equation to explain the change in the response. It is calculated as given by Equation (15) [17].

$$R^2 = \frac{\beta^T X^T Y - n\overline{Y}^2}{Y^T Y - n\overline{Y}^2} \quad (15)$$

R^2 is expected to be closer to 1 (100%). This means the factors those are used in regression model is sufficient and there is no need to use additional factors in the model. If the R^2 is big enough, then in the next stage the significance of the regression equation is determined by analysis of variance (ANOVA) [17].

2.3. Genetic Algorithm

GA is a search and optimization technique and was developed by Holand in 1975 [18]. The method mimics the evolutionary mechanism in nature according to natural selection and genetic principles. It works according to probability rules and only needs the purpose function GA investigates, but not all, of the solution area, so that an effective search results in a much shorter time. In the first stage of GA, chromosomes are developed for possible solutions. Chromosome set is the population of generation. The operators of GA are selection, crossover and mutation. Chromosomes in a generation evolve toward the next generation by these operators. There are many applications of GA such as transportation, scheduling, vehicle routing and etc.

The problem in this study is to determine the best combination of alpha, beta and gamma by GA. The alpha, beta and gamma variables that are desired to be optimized are continuous. Haupt & Haupt [19] states that the continuous GA is inherently faster than the binary GA, because the chromosomes do not have to be decoded prior to the evaluation of the cost function. Therefore, in this study continuous GA was used instead of binary GA due to its advantage of requiring less storage.

There are GA solutions that give minimization of a single error criterion (MAD, MAPE or MSE) as the objective function in the literature. Unlike the literature, the objective function in this study is the minimization of the sum of the properly weighted and normalized error criteria (MAD, MAPE, SSE, MSE, RMSE). The problem includes 5 constraints on 3 parameters to be optimized. Another aspect of this study that is different from the studies in the literature is that it obtains the performance criteria values depending on the factors namely alpha, delta and gamma. In the algorithm, performance criteria regression equations created from dataset are used to calculate the fitness function. Weights required for the fitness function of each chromosome are customized. Chromosome consists of alpha, gamma and delta values (chromosome= [α, γ, Δ]).

RESULTS AND DISCUSSIONS

In this paper we aimed to optimize the parameters (alpha, gamma, delta) of Winters method using GA. For this purpose; 5 different responses are selected as the performance criteria. These are the MAD, MAPE, SSE, MSE, and RMSE. Commercial vehicle sales of Fiat brand held in Turkey constitute the data set for this study. For this purpose, 109-month data were used (data for January 2011-September 2019) [20]. Data for the first 105 months were used for modeling; and data for the last 4 months were used for testing the model. In the first stage; an experimental design is conducted to calculate the responses. For this purpose; all the combinations of the factor levels (totally 240 combinations) given in Table 1 is modelled by Winters method using Minitab statistical package program (Minitab-16) and the responses are obtained.

Table 1. Factor levels of Winters method

Parameter	Symbol	Abbreviation	Factor level			
			Min	Max	Step Size	Number of levels
Alpha (level)	a	X_1	0.15	0.40	0.05	6
Gamma (trend)	b	X_2	0.00	0.04	0.01	5
Delta (seasonal)	I_t	X_3	0.00	0.035	0.005	8

In the Minitab simulations, seasonal length is selected as 60; and 4 forecasts are performed. In the second stage, regression models are calculated for the responses (MAD, MAPE, SSE, MSE, and RMSE) by using the Equations given under Section (2.2). Alpha, gamma, and delta are the factors of the regression equations. Aim is to determine the mathematical relation between the selected Winters parameters, and the observed error. Equation (16-20) shows the second-order regression equations:

$$\text{MAD} = 555.4444047619 - 1002.5321428572X_1 + 514.2638888889X_2 + 84.3990929705X_3 + 1408.2142857143X_1^2 - 729.1666666666X_2^2 - 79.3650793651X_3^2 - 715X_1X_2 + 16.3265306123X_1X_3 - 162.6984126984X_2X_3 \quad (16)$$

$$\text{MAPE} = 21.1627380952 - 42.2119047619X_1 - 2.0972222222X_2 - 6.4546485261X_3 + 53.5714285714X_1^2 + 44.6428571429X_2^2 + 182.5396825397X_3^2 + 2.1428571429X_1X_2 + 19.8639455782X_1X_3 + 19.8412698413X_2X_3 \quad (17)$$

$$\text{SSE} = 412875.165035518 - 1867225.07325863X_1 - 21686505.95696X_2 - 1470133.27844118X_3 + 3261578.84129872X_1^2 + 179341468.656222X_2^2 + 1607248.87417706X_3^2 + 94561498.9136115X_1X_2 + 4538553.84243567X_1X_3 + 36724171.5379833X_2X_3 \quad (18)$$

$$\text{MSE} = 103218.79125888 - 466806.268314656X_1 - 5421626.48923999X_2 - 367533.319610296X_3 + 815394.71032468X_1^2 + 44835367.1640556X_2^2 + 401812.218544265X_3^2 + 23640374.7284029X_1X_2 + 1134638.46060892X_1X_3 + 9181042.88449582X_2X_3 \quad (19)$$

$$\text{RMSE} = 237.1964685211 - 445.6712732510X_1 - 5880.8755460544X_2 - 513.4379831825X_3 + 994.6786448327X_1^2 + 42044.2250876962X_2^2 + 619.8831366164X_3^2 + 32121.7060515705X_1X_2 + 1611.7862747305X_1X_3 + 12896.9070539505X_2X_3 \quad (20)$$

The R^2 statistics (R^2, R^2-Prediction, R^2-Adjusted) for the given regression models (16-20) are calculated via Minitab and presented in Table 2.

Table 2. R^2 values for the regression models

Response	R^2 (%)	R^2(predicted) (%)	R^2(adj) (%)
MAPE	97.12	96.90	97.00
MAD	99.09	99.00	99.06
SSE	95.06	94.43	94.87
MSE	95.06	94.43	94.87
RMSE	87.72	86.20	87.24

According to Table 2, the regression models have good R^2 values. In other words, the factors namely alpha, gamma, and delta are sufficient for modeling the mentioned responses (there is no need to add additional factors to the models). In the next stage, significance of the model is tested with ANOVA. The results of ANOVA for the 95% confidence level and degrees of freedom with *m-1*= 9 and *N-m*=230 are summarized in Table 3.

Table 3. Summarized ANOVA results for the regression models

Response	F_0 *vs* $F_{0.05,9,230}$	P-Value vs α=0.05	Result
MAD	2789.03 > 1.88	0.000 < 0.05	Model Significant
MAPE	861.04 > 1.88	0.000 < 0.05	Model Significant
SSE	492.02 > 1.88	0.000 < 0.05	Model Significant
MSE	492.02 > 1.88	0.000 < 0.05	Model Significant
RMSE	182.50 > 1.88	0.000 < 0.05	Model Significant

If the $F_0 > F_{0.05,9,230}$ or if the p<0.05 (for 95% confidence level), the alternative hypothesis (H_1) is true, then means the regression model is significant and can be used for optimization. In the third stage, the optimization is performed to optimize these regression equations using the GA which is coded in MATLAB (R2016a). The results were obtained by running the coded GA on a PC (Intel Core i5 - 2.4 GHz processor, 4 GB RAM). In the GA, we use the population size 20, the crossover rate 0.50 and the mutation rate 0.20, 100000 iterations. In this study, the crossing method, in which Haupt & Haupt [19] combines the extrapolation method with a crossing method, is used.

Table 4. Weights and bounds for the responses

Response	Goal	Weight	Importance
MAPE	Minimum	1	6
MAD	Minimum	1	5
SSE	Minimum	4	1
MSE	Minimum	6	2
RMSE	Minimum	5	3

According to the constraints given in Table 4; four different optimizations are performed to find the optimum combination of alpha, gamma, and delta: *(i)* Response Surface Methodology (RSM); *(ii)* GA –with equal weights for the responses *(iii)* GA- with customized weights for the responses, *(iv)* Winter method with Minitab default values. Also to determine the effect of the selected performance criteria on the performance of the Winters method; these optimizations are performed for MAD and MAPE (which are widely used by Minitab) at the first stage (Table 5) and then the same optimizations are performed for all 5 responses (Table 6). In Table 5, although the optimization was made only according to MAPE, MAD, and SSE; also, the MSE, and RMSE were calculated again using optimum alpha, gamma and delta for the sales forecasts and presented to give the reader an idea. In *GA-with customized weights* for 3 responses, the weights of objective function are as w_1 = 0.05 for MAD, w_2 = 0.10 for SSE and w_3 = 0.85 for MAPE.

Table 5. Multi-objective optimization results for 3 responses (MAPE, MAD, SSE)

		RSM	GA –with equal weights	GA- with customized weights	Winter - with Minitab default values
Predicted Optimum Winters Parameters	Alpha(level)	0.3453	0.3464	0.2790	0.2
	Gamma(trend)	0	0.000052	0.000002	0.2
	Delta(seasonal)	0	0.000032	0.0350	0.2
Forecasts for 4 months	Observed Sales				
1	1554	1486.72	1485.85	**1520.774**	1254.09
2	2238	2333.16	**2331.67**	2392.043	1903.47
3	4836	4501.21	4498.16	**4623.761**	3545.43
4	1039	906.23	905.57	**932.3782**	687.49

Responses used for Optimization				
MAPE	**13**	**13**	14	16
MAD	**380**	**380**	390	478
SSE	143288	145358	**81247**	1990998
Responses those are not used for optimization				
MSE	35822	36339	**20312**	497750
RMSE	189	191	**143**	706

According to Table 5, RSM gives better results for MAPE and MAD, while GA-with customized weights gives good result for SSE. MSE and RMSE are not yet included in the study at this stage (their values were calculated to give the reader an idea). When estimation values are examined on a monthly basis instead of total average errors; while *GA-with customized weights* forecast the 1st, 3rd and 4th month sales closest, *GA-with equal weights* estimated the 2nd month's sales closest. *RSM* and *Winters - with Minitab default values* estimates are more distant than expected values in terms of months. Sales forecasts and estimation errors, which are considered good, are marked in bold in Table 5.

Then according to the motivation mentioned in the introduction part, MSE and RMSE are also added to the optimization process (to the fitness function of GA). The optimization results for 5 responses are presented in Table 6. In *GA-with customized weights* for 5 responses, the weights of objective function are as w_1=0.05 for MAD, w_2=0.05 for SSE, w_3=0.15 for MAPE, w_4= 0.20 for MSE, and w5 =0.55 for RMSE.

Table 6. Multi-objective optimization results for 5 responses

		RSM	GA –with equal weights	GA- with customized weights	Winter - with Minitab default values
Predicted Optimum	Alpha(level)	0.2914	0.3077492	0.249162732	0.2
Winters Parameters	Gamma(trend)	0	0.00000041	0.0000145251	0.2
	Delta(seasonal)	0.0124	0.0023	0.03499732	0.2
Forecasts for 4 months	Observed Sales				
1	1554	1520.14	1511.499	**1549.34**	1254.09
2	2238	2387.81	**2372.656**	2436.73	1903.47
3	4836	4610.38	4578.553	**4710.06**	3545.43
4	1039	928.83	921.995	**949.84**	687.49
Responses used for Optimization					
MAPE		14	**13**	14	16
MAD		386	**383**	396	478
SSE		86634	99908	**63325**	1990998
MSE		21659	24977	**15831**	497750
RMSE		147	158	**126**	706

As can be seen in Table 6, the error measurements of the forecasts obtained by *GA-with customized weights* (MAPE = 13, MAD= 383, SSE = 633325, MSE = 15831, and RMSE = 126) are the lowest responses. MAPE value (13) and MAD value (383) measured only by *GA-with equal weights* is slightly lower than MAD value (396) measured by *GA-with customized weights*. However, overall performance of *GA-with customized weights* is better than other methods, considering SSE, MSE and RMSE. When estimation values are examined on a monthly basis instead of total average errors; *GA-with customized weights* forecast gives the closest result in 3 out of 4 months. When the results given in Table 6 are compared with the results in Table 5, it is clearly observed that by considering the 5 responses instead of 3, the forecasts of 4 months seem to have become even closer to the observed sales. The Winter - with Minitab default values method has the worst performance in all error criteria compared to other methods. It was observed that alpha=0.249162732, gamma=0.0000145251, delta=0.03499732 determined by *GA-with customized weights* are the approximate optimum parameters for all the Responses. The Minitab Winters plot obtained with approximate optimum parameters is given in Figure 1.

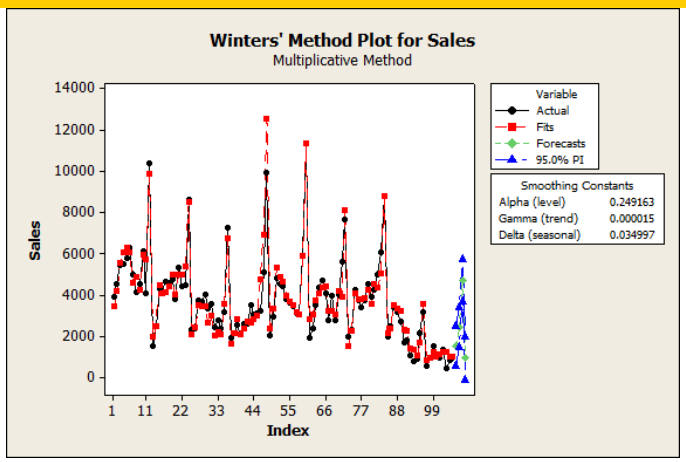

Figure 1 Minitab Winters plot of GA (with customized weights) optimization result for 5 responses

These results indicate that the GA algorithm has a good prediction performance. Especially GA with the customized weights gives good prediction performance for the Winters method.

CONCLUSION

In this paper, we have studied on the problem of the effective forecasting for automobile sales. There are many studies in the literature about the effective forecast of automobile sales. However, there is no other study using Winters optimized with GA is used to model. Motivation is to test the effectiveness of Winters method for car sales forecast problem, and to show the reader how the performance of the Winters method has changed with the use of a nature-inspired heuristic such as GA to provide a large number of performance criteria together. This problem was modeled as a multi-objective and continuous optimization problem by using regression. Then GA with weighted objectives was designed to solve the problem. Preliminary experiments were done on various Winters parameters using Minitab-16. Then the mathematical relation between the winter parameters and the performance criteria related with forecast errors are determined. The designed GA is used to find the optimum Winters parameters to optimize the prediction performance of the model. Regression modelling provided us an mathematical relationship which enabled us to optimize the problem with GA. Optimum factor levels for Winters method calculated as 0.249162732, 0.0000145251, 0.03499732 for alpha, gamma, and delta, respectively. The results of the forecasts for 4 months (Table 6) confirmed these findings. We can conclude that this paper succeeded to model the relation between the Winters parameters and the performance criteria; and also succeeded to calculate the optimum levels of these parameters effectively using the *GA-with customized weights* for objective. Finally by using these parameter levels, we were able to make accurate predictions at the end.

REFERENCES

[1]. T. Jun, and W. Qing, "Optimize BP neural network structure on car sales forecasts based on genetic algorithm," in Proceedings of the international industrial informatics and computer engineering conference (IIICEC 2015), Xi'an, Shaanxi, China, 10–11 January 2015, pp.75–79.

[2]. D. Fantazzini and Z. Toktamysova, "Forecasting German car sales using google data and multivariate models," International Journal of Production Economics, vol. 170, pp. 97–135, 2015.

[3]. A. Vahabi, S. Seyyedi, and M. Alborzi, "A sales forecasting model in automotive industry using adaptive neuro-fuzzy inference system (ANFIS) and genetic algorithm (GA)," International Journal of Advanced Computer Science and Applications, vol. 7, pp. 24-30, 2016.

[4.] J. Gao, Y. Xie, F. Gu, W. Xiao, J. Hu, and W. Yu, "A hybrid optimization approach to forecast automobile sales of China," Advances in Mechanical Engineering, vol. 9, pp. 1-10, 2017.

[5]. S. Fleurke, "Forecasting automobile sales using an ensemble of methods," WSEAS Transactions on Systems, vol. 16, pp. 329-337, 2017.

[6]. Y. Chen, M. Yao, and J. Zhang, "Research on auto sales forecast based on online reviews-take R brand automobile as an example," in 15th International Conference on Service Systems and Service Management (ICSSSM), July 21-22, Zhejiang, China, 2018.

[7]. H. Ceylan, O. Baskan, and C. Ozan, "Modeling and forecasting car ownership based on socio-economic and demographic indicators in Turkey," TEMA – Journal of Land Use, Mobility and Environmet, Special Issue 2018 - Urban Travel Behavior in the Middle East and North Africa, 2018.

[8]. A. Kaya, G. Kaya, and F. Cebi, "Forecasting automobile sales in Turkey with artificial neural networks," International Journal of Business Analytics, vol. 6, Special Issue: SI, pp. 50-60, 2019.
[9]. N. I. L. B. M. Azmi, "Parameters estimation of Holt-Winter method using genetic algorithm," Faculty of Science Universiti Teknologi Malaysia, Msc. Thesis, 2013.
[10]. E. Eusébio, C. I. Camus, and C. Curvelo, "Metaheuristic approach to the Holt-Winters optimal short term load forecast," Renewable Energy and Power Quality Control, vol. 1, pp. 708-713, 2015.
[11]. M. Akpinar and M. Yaz, "Electrical load forecasting using genetic algorithm based holt-winters exponential smoothing method," Sakarya University Journal of Computer and Information Sciences, vol. 2, pp 108-123, 2019.
[12]. S. Peng, S Qin, and G. Li, "Predicting expressway subsidence based on niching genetic algorithm and Holt–Winters model," Arabian Journal of Geosciences, vol. 12, pp. 354, 2019.
[13]. P. R. Winters, "Forecasting sales by exponentially weighted moving averages," Management Science, vol. 6, pp. 324-342, 1960.
[14]. C. C. Holt, "Forecasting seasonals and trends by exponentially weighted moving averages," ONR Memorandum, vol. 52, 1957.
[15]. E. A. Silver, D. F. Pyke, and R. Peterson, Inventory management and production planning and scheduling. New York: John Wiley & Sons, 1998.
[16]. A. D. Karaoglan and M. A. B. Ocaktan, "Winters metodunun parametrelerinin yanit yuzey yontemi ile optimizasyonu ve bir uygulama (Eng. Translation: Optimization of Parameters of Winters Method with Response Surface Method and an Application)," 13. Uretim Arastirmalari Sempozyumu - UAS 2013 (13th Production Research Symposium), pp. 946-954, Article No:1771356, 2013.
[17]. D.C. Montgomery, *Design and analysis of experiments*, 8th ed. New Jersey-NJ: John Wiley & Sons., 2013.
[18]. J. H. Holland, *Adaptation in natural and artificial systems*, Ann Arbor : University of Michigan Press, 1975.
[19]. R. Haupt and S. E. Haupt, *Practical genetic algorithms*, New Jersey: John Wiley &Sons, 2004.
[20]. Passenger Car and Light Commercial Vehicle Retail Sales Reports, ODD (Automotive Distributers' Association), Available: http://www.odd.org.tr/web_2837_2/neuralnetwork.aspx?type=35

BIOGRAPHY

Mustafa Ahmet Beyazit Ocaktan received a diploma degree in industrial engineering from Balikesir University in 1998 (Turkey) and Ph.D. in industrial engineering from Sakarya University in 2012 (Turkey). His research interests are simulation, applied statistics, and optimization. He is an assistant professor at Balikesir University (Turkey), Department of Industrial Engineering.

Aslan Deniz Karaoglan received a diploma degree in industrial engineering from Gazi University in 2001 (Turkey) and Ph.D. in industrial engineering from Dokuz Eylul University in 2010 (Turkey). His research interests are design of experiments, applied statistics, and optimization. He is an associate professor at Balikesir University (Turkey), Department of Industrial Engineering.

ICENS 6TH INTERNATIONAL CONFERENCE ON ENGINEERING AND NATURAL SCIENCE
October 21-25 2020 Belgrade

Why Is Pomegranate Molasses Important?

***Rabia Serpil Gunhan*[1]**

Abstract

As the awareness of healthy life develops, the importance of functional foods increases. One of these foods is pomegranate molasses. It is noteworthy that the production and consumption in the Middle East and the world is increasing day by day. Pomegranate mollasses is obtained by pressing the pomegranate fruit and thickening the pomegranate juice in the open or under vacuum by heat treatment. It is a durable product because of high acidity and water soluble dry matter. It is used in soups, salads and special dishes (lahmacun, doner, meatball etc.). It has a high medical and nutritional value. It is a powerful antioxidant and rich in anthocyanins and other phenolic compounds. It has antitumoral, antimicrobial, anti-inflammatory and antidiabetic properties. With the increasing demand in recent years, it has been observed that the quality of pomegranate molasses has decreased and additives such as glucose syrup, date syrup and lemon salt have been added. Especially in pomegranate molasses produced by traditional method, there are problems such as high temperature in open boiler and not paying attention to packaging. The purpose of this review is to emphasize the importance of pomegranate molasses, to point out its difference with pomegranate sour sauce and to draw attention to the production of high quality pomegranate molasses.

Keywords: Pomegranate Molasses, Pomegranate Sour Sauces

1. INTRODUCTION

The cultural history of Pomegranate (Punica granatum L.) is quite old. It is stated that it dates back to BC 3000 years ago. It is an important fruit of Mediterranean countries with subtropical and tropical climates. It is mainly cultivated in Iran, Afghanistan, India, USA, Mediterranean countries (Tunisia, Turkey, Egypt, Spain, and Morocco) and to some extent China, Japan, and Russia ([13], [27]-[12]). In Turkey according to TUIK data pomegranate production are made about 300 thousand hectares in the area. Pomegranate is a product that grows in many regions of our country, especially in the Aegean and Mediterranean regions. Approximately 1/3 of our pomegranate production is exported ([5]).

Pomegranates are usually consumed fresh; however they are also a source of juice and molasses. Although rough information is obtained about the history of pomegranate from prehistoric times, we do not know exactly how long pomegranate molasses is in our lives. Turkey is one of the world's main pomegranate producing countries and produces the concentrated pomegranate juice known as pomegranate molasses or pomegranate syrup obtained from sour pomegranate species ([10]). Pomegranate molasses give flavor especially to salads and appetizers. It is used in dishes such as Mualle (a very demanding meal unique to Hatay), stuffed peppers, stuffed grape leaves, chicken and meatballs as the main ingredient of direct food. Although it seems easy to produce, it is actually quite troublesome. 1 kg of pomegranate molasses is obtained from approximately 10-15 kg of pomegranate ([2]-[8]).

Pomegranate syrup is a sour food product obtained by pressing the pomegranate fruit, clarifying the obtained pomegranate juice and concentrating it in the open or under vacuum in accordance with the technique and consumed with the aim of flavoring foods ([2]). Pomegranate is a rich source of many
valuable substances, such as tannins, (e.g., punicalagins, punicalins, proanthocyanidins), anthocyanins, phenolic acids (e.g., gallic acid, ellagic acid) and organic acids (e.g., malic acid). These substances have high antioxidant activity and have been correlated with health benefits against cancer, cardiovascular, and other diseases ([12]).

Since the pomegranate juice is concentrated in the production of pomegranate syrup, its nutritional value is quite high, there are more phenolic compounds and mineral substances than pomegranate juice. It is a

[1] *Corresponding author: Konya Technical University, Vocational High School of Technical Sciences, Department of Food Technology, Konya, Turkey. rsgunhan@ktun.edu.tr*

storehouse of vitamins and energy, in addition it has high antibacterial and antioxidant effects because of containing phenolic compounds so it is beneficial in the treatment and prevention of many diseases([1], [4], [13], [35]-[37]

In this study, it was aimed to draw attention to the importance of pomegranate molasses, the differences between pomegranate molasses and pomegranate sauce, and the adulteration of pomegranate molasses.

2. METHODS OF POMEGRANATE MOLASSES PRODUCTION

The pomegranate molasses is produced by both industrial and traditional methods. The pomegranate juice is concentrated simply by boiling, without additives like sugar or others for traditional production of pomegranate molasses. On the other hand, the industrial ones may contain pomegranate juice concentrate, glucose, citric acid, antioxidant agents, coloring agents, and some preservatives as declared on the labels ([10]). Pomegranate molasses according to TSE ([36]); It is defined as "it is a sour food product obtained by pressing the pomegranate fruit, clarifying the obtained pomegranate juice and thickening it in the open or under vacuum in accordance with its technique and produced to flavor the foods." ([4]). According to Turkish Standards Institute pomegranate molasses should be free of sediment, fruit particles and sucrose. Whereas, people want bitter taste and sourness in pomegranate molasses. Therefore, it is not recommended to clarify the pomegranate juice. In the production of natural pomegranate molasses, a residue forms in the bottle and this residue is the condensated polyphenols ([1]).

The production steps of the traditional method of pomegranate molasses are washing, sorting, granulation, pressing, boiling (evaporation), cooling, removing of the solid phase and bottling respectively. This product is boiled in open boilers until its brix value becomes 35-50% and pomegranate molasses is obtained ([3]-[16]). In commercial production, there are pasteurization of pomegranate juice, enzyme addition, clarification, filtration, evaporation stages ([35])

Unlike pomegranate molasses, pomegranate sour souce contains glucose syrup, water, pomegranate flavor, acidity regulator (citric acid), coloring and preservative ([7]).

Table 1. General characteristics of pomegranate molasses ([36])

Features		Limits
Water soluble dry matter, at least	68.0%	
Titratable acidity, not less than		7.5%
pH value		3.0
Hydroxymethyl furfural (HMF), (mg / kg)		50
No Sucrose		
No Preservatives		
No Artificial Dye stuffs		

3. THE QUALITY OF POMEGRANATE MOLASSES

Factors such as pomegranate variety, production method, method differences, heat treatment parameters, storage conditions directly affect the quality of pomegranate molasses. Physicochemical properties such as pH, dry matter, viscosity, bioactive compound level, HMF level, whether there is glucose and antioxidant activity are analyzed in the quality assessment of pomegranate molasses.

3.1. Pomegranate variety

The composition of pomogranate and pomogranate juice apart from the juice preparation methods is influenced by cultivar, growing conditions, climate, maturity and storage conditions ([31], [32], [26]-[19]). Pomegranates which have red grains and sour are selected especially to obtain pomegranate juice or pomegranate molasses ([33])

The contents of the pomegranate plant may vary according to the soil structure, climatic conditions, the time and amount of the plant to benefit from sunlight, the time of harvest, the storage conditions after harvest,

cultural practices, etc. This situation causes the antioxidant and antibacterial effects of pomegranate molasses products to differ ([34]).

3.2. Production methos differences

Uncontrolled heat treatment in parallel with the application of heat treatment under open boiler or vacuum negatively affects phenolic compounds, anthocyanins, HMF load in pomegranate molasses ([22], [21], [20], [18]-[1]).

The method differences in the production of concentrated pomegranate juice directly affect the quality of pomegranate molasses. Apaydin ([19]) investigated the importance of clarification step during the production of concentrated pomegranete juice and observed that the production without clarification has more total phenolic substances (39%) and more antioxidant activity (25%) compared to clarificated ones and no significant change of total phenolic level in concentrated pomegranete juice samples during the storage. Maskan ([21]) investigated the effect of various heating methods (microwave, rotary vacuum and atmospheric heating) to produce concentrated pomegranate juice. He reported that the severity of colour loss was higher in rotary vacuum heating process than the others and microwave energy could be used in production of pomegranate juice concentrate successfully. Dhumal et al.([22]) used different concentration techniques like atmospheric heating, microwave heating and rotary vacuum evaporation to produce the pomegranate juice concentrate. They reported that different heating methods influence the physicochemical constituents, sensorial properties and microbial population of concentrated pomegranate juice. They stated that vacuum evaporation give great benefits and the best colour in final product and vacuum concentration and microwave energy could be used in production of pomegranate juice concentrate successfully.

Unlike pomegranate molasses, pomegranate sour souce contains glucose syrup, water, pomegranate flavor, acidity regulator (citric acid), coloring and preservative ([7]). Food fraud is a serious ethical and economic problem affecting the food industry. Darra et al. ([14]) highlighted that date syrup was a potential raw material to adulterate commercial pomegranate molasses. They used UV/VIS spectroscopy, HPLC and ATR-FTIR method to determine the adulteration with date syrup and citric acid in the pomegranate molasses. They remarked that some of the commercialized pomegranate molasses in the Middle East area are adulterated with cheaper date syrup. Kamal et al.([13]) had developed successfully a new method that was simple, reliable and reproducible for the quality control of various formulations containing pomegranate. They reported that the matrix solid phase dispersion extraction methodology and HPLC method could be used successfully for the quantification of vitamin C, gallic acid, rutin and gallic acid in pomegranate molasses samples. Ergin ([4]) stated that some pomegranate molasses do not comply with the standards because of wrong practices and hygiene deficiencies during production and bottling in traditional production and using additives such as glucose / fructose syrup, synthetic antioxidant in commercial production.

3.3. Hydroxy Methyl Furfural (HMF)

HMF is an indicator of quality loss in most foods containing carbohydrates due to excessive heat treatment and improper storage conditions. HMF is known as an indicator of overheating, spoilage and possible adulteration with sugar or syrup. HMF is found in high levels in most foods, especially in caramel products (9.5 g / kg), dried fruits, wines, balsamic vinegars, molasses and pomegranate syrups. In high concentrations, Hydroxymethylfurfural (HMF) is known to have cytotoxic, genotoxic, nephrotoxic, mutagenic and carcinogenic effects ([7]). Orak ([20]) reported that the high temperature and long evaporation time of traditional method of pomegranate molasses destroy anthocyanin pigments and cause to increasing the level of HMF in concentrated pomegranate juices. Metin ([7]) determined HMF level of different brands of pomegranate molasses and pomegranate sour sauces saled in Turkey as 91.1 - 11485.7mg / kg and 41 - 151.9 mg / kg respectively. It is stated that the difference in HMF level in the products may be caused by the difference of pomegranate species, applied heat treatment technique, size and duration, and storage conditions. Hepsag et al. ([6]) determined quality parameters such as pH, water-soluble dry matter, titratable acidity, total dry matter, HMF, color analysis in home-type traditional pomegranate molasses produced from pomegranate varieties developed in the Osmaniye Region. The level of HMF were found to be in between 143.23 ile 530.68 mg/L. They stated that traditional home-type pomegranate syrups pose health problems because of their high HMF values. Onsekizoglu ([24]) used osmotic distillation and membrane distillation + osmotic distillation methods in the production of pomegranate juice. He stated that HMF formation was low in the pomegranate juice concentrates obtained by these methods

3.4. Bioactive components of pomegranate molasses

Pomegranate juice contains significant phenolic substances. The substances that give the pomegranate color from pink to purple are anthocyanin group substances. Pomegranate juice carries a distinctive bitter flavor. This bitter flavor is caused by various polyphenolic substances and especially tannins. These substances are also the cause of cloudiness of pomegranate juice ([23]-[26]). Incedayi et al.([26]) investigated the chemical components which are important for health in different brands of pomegranate molasses.They reported that pomegranate molasses is rich in phenolics if it is produced correctly. The total amount of phenolic matter was found as 3246 µg gallic acid equivalent / mL in pomegranate juice and 9870 µg in pomegranate syrup.

Manufacturing of pomegranate juice causes relevant changes on the bioactive compounds [12]). It was stated that the heat treatment application in traditional pomegranate syrup production at high temperatures and long-term causes reduction of the anthocyanin pigments ([20]). Various factors including the temperature of processing and storage, the chemical nature of antosiyonin, pH, ascorbic acid, hydrogen peroxide, sugars, light and metals affect the stability of antosiyanin in pomegranate juice. ([18]). Phenolic compounds such as anthocyanins, ellagic and gallic acids are remarkably decreasing during juice processing line, especially after pasteurization, clarification and filtration processes ([17]- [18]). Akyildiz et al. ([17]) reported that processing stages were caused to lose 26, 45 and 41 % of concentrations of ellagic acid, cy-3,5-diglu and gallic acid according to the initial contents. Ozkan ([28]) determined that the anthocyanins from pomegranate juices was sensitive to hydrogen peroxide and added ascorbic acid increased the stability of anthocyanins in pomegranate juice.

3.5. Bioactivities and health benefits

Anthocyanins, ellagic acid derivatives, and hydrolyzable tannins are responsible for the high antioxidant activity of pomegranate juice. The high antioxidant activity in the pomegranate juices are correlated significantly to the total polyphenol and anthocyanin contents ([11]). Pomegranate juice has high antioxidant activity. This activity is associated with the flavonoid content of pomegranate ([29]). Yildiz et al. ([9]) determined that pomegranate molasses had high phenolic content, antioxidant and antimicrobial activity and indicated that pomegranate sour sauce was a potent antioxidant food and potential value as a functional food ingredient.

The phytochemicals found in pomegranate are predominantly polyphenols, including flavonoids (anthocyanins, catechins and other complex flavonoids) and hydrolyzable tannins (punicalin, pedunculagin, punicalagin, gallagic and ellagic acid esters of glucose), which account for 92% of its antioxidant activity ([9]). Pomegranate phytochemicals are effective in prevention of various types of cancers, various cardiovascular diseases, in the treatment for trauma haemorrhage, ulcers, infections, diarrhoea and dysentery ([13]- [9]). Ellagic acid in pomegranate is the most important bioactive compound on human health. It has antioxidant, anticarcinogenic, antiestrogenic and antimutagenic effects ([27]). According to Mounayer et al. ([25]), pomegranate molasses possesses a powerful antioxidant activity and a weight loss effect in mice. They reported that pomegranate molasses at low doses in the beverage of mice is able to resist weight gain, induce the loss of fat stores, decrease tissue necrosis, and protect against deleterious effects of free radicals ([25]).

Antioxidant activity of different brands of commercial pomegranate molasses was determined by Incedayi et al. ([26]) as between 0-46.31%. Orak ([20]) compared the antioxidant levels of pomegranate juice and traditional pomegranate molasses and reported that the antioxidant activity of pomegranate extract (85.91%) was higher than that of pomegranate juice (79.06%). In the same study, pomegranate molasses was found to decrease the glucose and fructose levels and increase the potassium and magnesium ratios. The total amount of phenolic substance was found in pomegranate juice and in pomegranate molasses as 3246 µg gallic acid equivalent / mL and 9870 µg gallic acid equivalent / mL respectively.

Karabiyikli and Kisla ([10]) investigated the antimicrobial effect of traditional pomegranate sour sauce and commercial pomegranate molasses on microflora of some green vegetables and burgul salad at different application times. They reported that traditional pomegranate molasses have more effective than the commercial pomegranate sauces on antimicrobial effect because of the differences of raw material and production methods. Gokoglu et al. ([15]) investigated the effects of pomegranate sauce on the quality of marinated anchovy. Anchovy had marinated with acetic acid, salt, sunflower oil and pomegranate sauce. They demonstrated that pomegranate juice concentrate affected quality and shelf life of marinated fish, finding that pomegranate sauce showed better oxidative stability and pomegranate sauce gived a special taste.

As highlighted by Faour-Klingbeil and Todd ([30]), Pomegranate molasses had a great potential to enhance the microbial safety, especially *Salmonella enterica serovar Typhimurium LT2 (S. typhimurium*), of parsley and salad vegetables as a food condiment. Kisla and Karabiyikli ([8]) determined the minimum inhibitory concentrations (MICs) of both traditional and commercial sour pomegranate sauce samples on *Staphylococcus aureus* (ATCC 25923) and *Escherichia coli* O157 :H7 (ATCC 43895) and indicated that the traditional products showed more antimicrobial effect on the pathogens than the industrial products. It has been stated that the industrial products may contain glucose, glucose syrup, citric acid, antioxidant agents, coloring agents, some preservatives and these additives caused decreasing of the concentrations of antimicrobial compounds.

4. CONCLUSION

Since pomegranate syrup is a functional food, its production and consumption should be encouraged. In this context, correct production processes and consumer awareness gain particular importance. If the correct production technique is applied, pomegranate molasses is a very beneficial product for human health and has a high nutritional value. Especially being rich in phenolic content also increases the antioxidant activity of the product. In the production of traditional pomegranate syrup, production and bottling must be applied correctly and adequate attention should be given to hygiene. In industrial production, negativities such as additives, glucose / fructose syrup, antioxidant addition should not be allowed. It should be checked more frequently whether there is adulteration in pomegranate molasses and the consumer should be informed about consuming the right product. So pomegranate molasses is a product that should be included more in our diet.

REFERENCES

[1]. F.S. Eyigun, ' Hicaz Nar cesidine ait narlardan elde edilen nar eksilerinin ozelliklerinin belirlenmesi uzerine bir arastirma', Yuksek lisans tezi , Cukurova Universitesi, Fen Bilimleri Enstitusu, Gida Muhendisligi Anabilim Dali, Turkiye, 2012.

[2]. T. Baysal ve O. Tastan, *Nar urunleri ve uretimi*, In book: Nar Saglikta Yildiz Publisher: Gece Kitapligi, 2018.

[3]. Bilgin C., 2017. Eksinin en tatli hali nar eksisi, Available: https://www.gidagundemi.com/makale/eksinin-en-tatli-hali-nar-eksisi-m228.html

[4]. S.O. Ergin, 'Nar Meyvesi (Punica granatum L.) ile Farkli Nar Urunlerinin Antioksidan Ozellikleri', *Akademik Gida* 17(2), 243-251, 2019.

[5]. Anonim, 2019, Nar Raporu, https://zmo.org.tr/genel/bizden_detay.php?kod=32164&tipi=17&sube=0

[6]. F. Hepsag, M. Ferliaslan , O. Duran , S. Okur ve Y. Yildiz, 'Osmaniye Ilinde Geleneksel Ev Yapimi Uretilen Nar Eksilerinin Kalite Ozelliklerinin Belirlenmesi Uzerine Bir Arastirma,' *Batman Universitesi Yasam Bilimleri Dergisi* 9(2), 95-107, 2019.

[7]. Z. Metin, 'Ankara piyasasinda satisa sunulan nar eksisi, nar eksisi sosu ve uzum pekmezlerinin hidroksimetilfurfural duzeyinin saptanmasi', Yuksek Lisans Tezi, Hacettepe Universitesi, Saglik Bilimleri Enstitusu, Turkiye, 2014.

[8]. D. Kisla and Karabiyikli S., 'Antimicrobial Effect of Sour Pomegranate Sauce on *Escherichia coli* O157 : H7 and *Staphylococcus aureus.' Journal of Food Science*. Vol. 78, Nr. 5., 2013.

[9]. Yildiz H, Sengul M, Cetin B, Karatas N, Ercisli S, Okcu Z, Dzubur A. and Hadziabulic S., 'Antioksidant and antimikrobial activities of pomegranate (Punica Granatum L.) sour sauce extracts,' Compt. rend. Acad. bulg. Sci., 67, No 1, 2014.

[10]. Karabiyikli S and D. Kisla, 'Inhibitory effect of sour pomegranate sauces on some green vegetables and kisir', *International Journal of Food Microbiology* 155, 211–216, 2012.

[11]. Z. Kalaycioglu and F.B. Erim, 'Total phenolic contents, antioxidant activities, and bioactive ingredients of juices from pomegranate cultivars worldwide', *Food Chemistry*, 221, 496–507, 2017.

[12]. N. Nuncio-Jáuregui, A. Calín-Sánchez, L. Vázquez-Araújo , A.J. Pérez-López, M.J. Frutos-Fernández and A.A. Carbonell-Barrachina, *Processing Pomegranates for Juice and Impact on Bioactive Components*, editor: Victor R. Preedy, Processing and Impact on Active Components in Food, Chapter 76, 629-636, 2015. **http://dx.doi.org/10.1016/B978-0-12-404699-3.00076-7**

[13]. Y.T. Kamal, P. Alam, S.I. Alqasoumi, A.I. Foudah, M.H. Alqarni and H.S. Yusufoglu, 'Investigation of antioxidant compounds in commercial pomegranate molasses products using matrix-solid phase dispersion extraction coupled with HPLC', *Saudi Pharmaceutical Journal* 26 , 839–844, 2018.

[14]. N. Darra, H.N. Rajha, F. Saleh, R. Al-Oweini, R.G. Marounand and N. Louka, 'Food fraud detection in commercial pomegranate molasses syrups by UV-VIS spectroscopy, ATR-FTIR spectroscopy and HPLC methods', *Food Control* 78, 132-137, 2017.

[15]. N. Gokoglu, O.K. Topuz and P. Yerlikaya, 'Effects of pomegranate sauce on quality of marinated anchovy during refrigerated storage', *LWT - Food Science and Technology*, 42, 113–118, 2019.

[16]. H. Vardin ve M. Abbasoglu, 'Nar eksisi ve narin diger degerlendirme olanaklari,' *Geleneksel Gidalar Sempozyumu* bildirileri, 2004, 165-169.

[17]. Akyildiz, E. Karaca, E. Agcam, B. Dundar and N.I. Cinkir, 'Changes in quality attributes during production steps and frozen-storage of pomegranate juice concentrate,' *Journal of Food Composition and Analysis*, 92;103548, 2020.

[18]. O. Turfan, M. Turkyilmaz, O. Yemis and M. Ozkan, 'Anthocyanin and colour changes during processing of pomegranate (Punica granatum L., cv. Hicaznar) juice from sacs and whole fruit', *Food Chem*. 129, 1644–1651, 2011.
[19]. E. Apaydin, 'Nar suyu konsantresi uretimi ve depolama surecinde antioksidan aktivitedeki degisimler', Yuksek lisans tezi, Ankara Universitesi, Fen Bilimleri Enstitusu, Gida Muhendisligi Anabilim Dali,Turkiye, 2008.
[20]. H. Orak, 'Evaluation of antioxidant activity, colour and some nutritional characteristics of pomegranate (*Punica granatum* L.) juice and its sour concentrate processed by conventional evaporation', *International Journal of Food Sciences and Nutrition*, 60(1): 1-11, 2008.
[21]. M. Maskan, 'Production of pomegranate (Punica granatum L.) juice concentrate by various heating methods: colour degradation and kinetics', *Journal of Food Engineering*,72; 218–224, 2006.
[22]. S.S. Dhumal, A.R. Karale, T.A. More, C.A. Nimbalkar, U.D. Chavan and S.B. Adhav, 'Preparation of Pomegranate Juice Concentrate by Various Heating Methods and Appraisal of Its Physicochemical Characteristics', *Beverage and Food World*, 42(5), 25-30, 2015.
[23]. T. Oztan, 'Mor havuc, konsantresi, salgam suyu, nar suyu ve nar eksisi urunlerinde antioksidan aktivitesi tayini ve fenolik madde profilinin belirlenmesi', Yuksek lisans tezi, Istanbul Teknik Universitesi, Fen Bilimleri Enstitusu, Turkiye, Yuksek lisans tezi, 2006.
[24]. P. Onsekizoglu, 'Production of high quality clarified pomegranate juice concentrate by membrane processes', *Journal of Membrane Science*, 442, 264- 271, 2013.
[25]. A.C. Mounayar, A.R. Nemr, P. Yared, S. Khairallah and R. Chahine, 'Antioxidant and Weight Loss Effects of Pomegranate Molasses', *Journal of Applied Pharmaceutical Science*, 02 (06) : 45-50, 2012.
[26]. B. Incedayi, C.E. Tamer and O.U. Copur, 'A research on the composition of pomegranate molasses'. Journal of Agricultural Faculty of Uludag University, 24(2), 37-47, 2010.
[27]. M. Simsek and A. Ikinci, 'Narin (*Punica granatum* L.) Insan Sagligina Etkileri', *Harran Tarim ve Gida Bilimleri Dergisi*, 21(4): 494-506, 2017.
[28]. M. Ozkan, 'Degradation of anthocyanins in sour cherry and pomegranate juices by hydrogen peroxide in the presence of added ascorbic acid', *Food Chemistry*, 78, 499–504, 2002.
[29]. B. Cerda, R. Llorach, J.J. Ceron, J.C. Espin and T. Tomas-Barberan, 'Evaluation of the bioavailability and metabolism in the rat of punicalagin, an antioxidant polyphenol from pomegranate juice', *Eur. J. Nutr., 42*, 18–30, 2003.
[30]. D. Faour-Klingbeil and E.C.D. Todd, 'The inhibitory effect of traditional pomegranate molasses on S. typhimurium growth on parsley leaves and in mixed salad vegetables', *J Food Saf.*, 38;e12469, 2018. https://doi.org/10.1111/jfs.12469
[31]. Topalavic, M. Knezevica, A. Gacnic and M.M. Petkovsek, 'Detailed chemical composition of juice from autochthonous pomegranate genotypes (*Punica granatum* L.) grown in different locations in Montenegro', *Food Chemistry*, 330; 127261, 2020.
[32]. D.Y. Turgut ve A.C. Seydim, 'Akdeniz Bolgesi'nde yetistirilen bazi Nar (*Punica granatum* L.) cesit ve genotiplerinin organik asit ve seker kompozisyonu' , *Akademik Ziraaat Dergisi*, 2(1):35-42, 2013.
[33]. Ikinci ve H. Vardin, 'Nar meyvesi ve narin degerlendirilme sekilleri', *Tarim Turk*, 19(4), 2009.
[34]. N. Erbil ve M. Arslan, 'Geleneksel Yontemlerle Uretilen Nar Eksisinin Antibakteriyel ve Antimutajenik Etki Potansiyeli', *Erzincan Unv Fen Bilimleri Derg*., 12(2), 957-965, 2019.
[35]. S.O. Ergin, 'Investigation of the physicochemical, nutritional properties and antioxidant activities of commercial and traditional pomegranate molasses samples', *Food and Health*, 6(3), 177-185, 2020.
[36]. *Nar eksisi standardi*, TS 12720 / Nisan 2001.
[37]. Y. Yilmaz, I.Celik and F. Isik, 'Mineral composition and total phenolic content of pomegranate molasses', *Journal of Food, Agriculture & Environment* Vol.5 (3&4) : 102-104, 2007.

BIOGRAPHY

Rabia Serpil Gunhan was born in Konya, Turkey on April 4, 1971. She received the engineering degree in food engineering from the "Hacettepe" University, Ankara, Turkey, in 1996. She received the M.Sc and Ph.D. degree in the department of food hygiene and technology of veterinary faculty, "Selcuk" University, in 2006 and 2014, respectively. She is academic at food technology department of vocational high school, Konya Technical University, Konya, Turkey. Her research interests food technology and functional food.

ICENS 6TH INTERNATIONAL CONFERENCE ON ENGINEERING AND NATURAL SCIENCE
October 21-25 2020 Belgrade

Wireless Capsule Localization Inside the Human Small Intestine Using a Permanent Cube-Shaped Magnet with Analytical Magnetic Model

Muzaffer Kanaan[1], Memduh Suveren [2]

Abstract

Wireless Capsule Endoscopy (WCE) is a non-invasive technique used to visualize the digestive system in the human body. Many gastrointestinal (GI) system diseases such as Crohn's disease, tumor, bleeding, and polyps can be easily diagnosed with WCE. In recent years, the tendency to WCE method has been increasing especially in order to eliminate the disadvantages of traditional colonoscopy (being painful, risk of infection, completely dependent on operator skill, psychologically disturbing the patient). Here, together with the diagnosis made with the WCE technique, determining the location of the disease detected in the intestine is of great importance for the medical specialist. Therefore, this study focused on determining the position of WCE in the intestine. In this study, a cube-shaped magnet was used together with the wireless capsule, and the predicted positions of the wireless capsule in the small intestine were obtained using magnetic sensors placed on the human body model and the LM-ABC optimization algorithms. As a result, 5D (3D position, 2D orientation) localization procedure was performed with the analytical magnetic model of the cube magnet.

Keywords: Wireless Capsule Endoscopy, In-body Localization, LM algorithm, ABC algorithm

1. INTRODUCTION

Wireless capsule endoscopy is a painless and non-invasive diagnostic technique used in the digestive system, especially to view the small intestine [1]. WCE is especially used to visualize sections of the small intestine that are difficult to access with conventional endoscopy techniques. In this imaging method, a wireless capsule which has camera, battery, processor and wireless transmitter is swallowed [2]. The capsule moves passively with peristaltic contractions of the intestine in the GI tract, and the camera inside the capsule takes pictures and transmits the images to the outside via a wireless transmitter. These images taken are then analyzed by the specialist for the diagnosis and treatment of diseases. The aim of this technique, which is currently used today, is not only to diagnose but also to provide treatment. This is possible with active capsule endoscopy [3]. Active capsule endoscopy is basically manipulating the wireless capsule inside the body and changing capsule positions and angles from the outside by the specialist. The most important problem for active capsule endoscopy is that the position and orientation of the capsule should known precisely.

There are many studies on capsule localization in the literature. These are generally in the form of positioning with electromagnetic waves (radio frequency, visible waves, X-ray, Gamma ray), magnetic localization and other techniques (MRI, ultrasound) [4]. Although X-ray and Gamma ray techniques promise real-time and precise results, the biggest disadvantage of these techniques is that they have harmful effects on human health [5]. MRI and Ultrasound methods require extra space in the capsule and power consumption, so these techniques are not used much. In positioning with radio waves, high frequency signals are subjected to significant attenuation as they pass through body tissues [6]. Different tissue types (skin, muscle and bone) all have frequency-dependent propagation characteristics and adversely affect the transmission of RF signals [7]. For this reason, positioning errors are relatively higher in RF positioning in the body, since there is no direct line of sight between the sensor and the antenna [8]. On the other hand, magnetic localization method is being

[1] *Erciyes University, Department of Mechatronic Engineering, 38038, Melikgazi/Kayseri, Turkey.* mkanaan@erciyes.edu.tr

[2] *Corresponding author: Erciyes University, Department of Mechatronic Engineering, 38038, Melikgazi/Kayseri, Turkey.* msuveren@erciyes.edu.tr

studied because it does not require a direct line of sight and low-frequency static magnetic signals pass through body tissues without interaction as they pass through the air [9, 10].

Magnetic flux density generated by a permanent magnet or a current-controlled coil is used for magnetic localization. The position and angle of the magnet or coil can be calculated by means of previously known magnetic flux equations and hall effect sensors that measure these fluxes. Various magnetic flux equations are used in the literature such as Dipole model, finite difference method, Biot-Savart method and charge model. Then, optimization algorithms are used in solving the magnetic flux equations. In this study, the charge model equations of a cube-shaped permanent magnet were obtained and positioning studies were carried out using Artificial Bee Colony (ABC) and Levenberg-Marquardt (LM) optimization algorithms. The LM method, frequently used in positioning algorithms, is a combination of two minimization methods: the gradient descent method and the Gauss-Newton method [11]. ABC algorithm is an optimization algorithm based on a certain intelligent behavior of honeybee swarms in nature [12]. These two algorithms have been used together in this study to eliminate the disadvantages of each other and to make more precise positioning as in the previous study [13].

In this study, we gave information about the simulation environment in Section 2, obtained the analytical model for the magnetic localization algorithm in Section 3, and discussed the results in Section 4.

2. SIMULATION ENVIRONMENT

In simulations, it is aimed to obtain 5D (3D position and 2D angle) parameters of the magnetic capsule. It is assumed that a permanent cube-shaped magnet is placed at the back of the capsule to localize the capsule. Here, while the magnetic capsule moves inside the body, especially in the small intestine, the videos and images it sends to the external environment are matched with the location in the intestine. In order to see more realistic results, capsule locations were determined according to the real human intestine, not randomly. For this, 3-D voxel model data of the human body developed under the Visible Human Project [14] as shown Figure 1 was used.

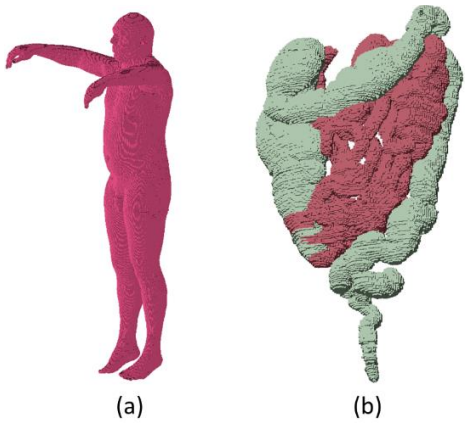

Figure 1. 3-D voxel models of the human body: a) The full body model, b) The intestine model

In the simulations, real magnet positions and angles were obtained for 80 different capsule locations in the small intestine. The magnet positions were homogeneously distributed in the area of 195x115x290mm. Here, the orientation of the capsule was determined to remain within the intestine. In addition, 9 sensors that measure magnetic flux, were placed on the body. Sensors were placed on the body at equal intervals and contacted the body. Thus, the actual sensor positions were taken over the body model, such as the capsule positions. These sensor and capsule locations are shown in Figure 2.

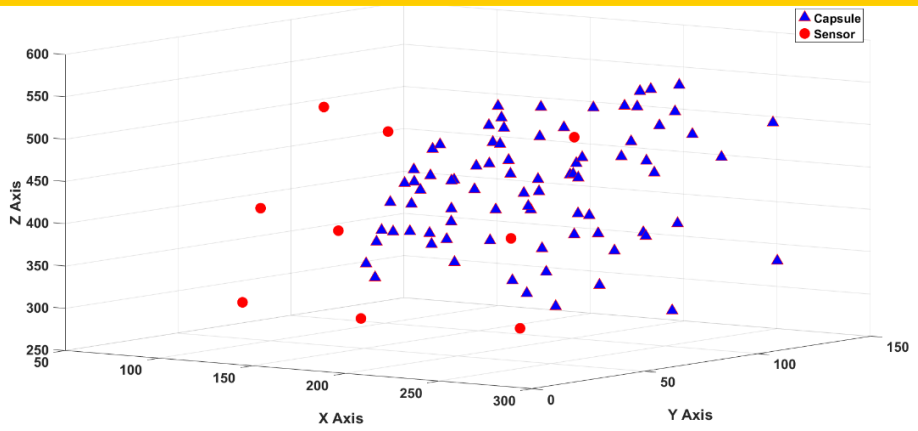

Figure 2. Sensor and Capsule positions in the body (mm)

The cube-shaped magnet structure shown in Figure 3 was used in the simulations. Each side length of the magnet is determined as 4mm. Thus, there will be no problem in capsule endoscopy since the magnet will not take up much space behind the capsule. The magnet also provides uniform magnetization in the z-axis direction and the **M** value is set as 830.000 (A/m) for the neodymium permanent magnet (NdFe35).

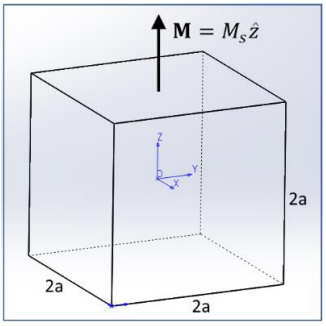

Figure 3. Cube Shaped Magnet

3. LOCALIZATION ALGORITHM

The localization algorithm consists of 3 parts: Analytical model, ABC optimization algorithm and LM algorithm. The working scheme of the localization algorithm is given in Figure 4.

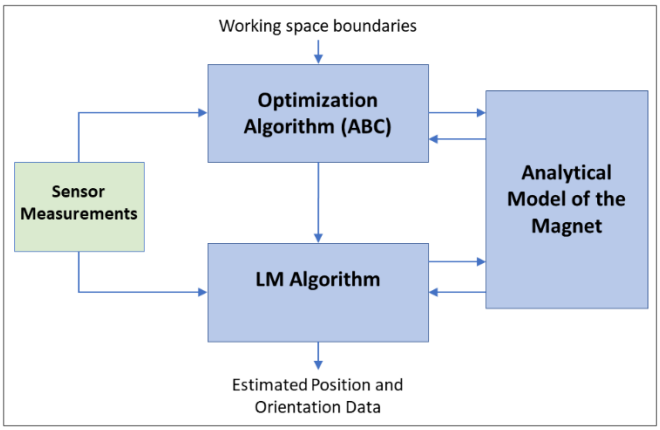

Figure 4. Working Scheme of the Localization Algorithm

The magnetic flux data calculated from the sensors on the body are given as an input to both the ABC algorithm and the LM algorithm. Here, the ABC algorithm generates the initial position parameters required for the LM algorithm. Both algorithms use the analytical magnetic model of the cube magnet to estimate the position and orientation parameters of the capsule.

3.1. Analytical Model of the Cube-Shaped Magnet

In magnetically positioned wireless capsule endoscopy, generally ring and quadrangular shaped magnets are used. While the magnetic fluxes of permanent magnets are obtained, the current model, charge model and finite difference method are mostly used in the literature. Here, magnetic flux equations of the magnet are created using the charge model. In this model, a magnet is reduced to a distribution of equivalent ‘‘magnetic charge’’. The charge distribution is used as a source term in the magnetostatic field equations, and the fields are obtained using standard methods [15]. The general magnetic flux equation given in Equation 1 is used to calculate the magnetic flux with the charge model.

$$\mathbf{B}(\mathbf{x}) = \frac{\mu_0}{4\pi}\int_V \frac{\rho_m(\mathbf{x}')(\mathbf{x}-\mathbf{x}')}{|\mathbf{x}-\mathbf{x}'|^3}dv' + \frac{\mu_0}{4\pi}\iint_S \frac{\sigma_m(\mathbf{x}')(\mathbf{x}-\mathbf{x}')}{|\mathbf{x}-\mathbf{x}'|^3}ds' \tag{1}$$

Here, the magnetic flux equation consists of two integrals containing volume (ρ_m) and surface (σ_m) charge density. Here, the volume charge density will be 0 in empty space, the surface charge density changes as in Equation 2 depending on the coordinates of the magnet given in Figure 3.

$$\rho_m = -\nabla\cdot\mathbf{M} = 0$$
$$\sigma_m = \mathbf{M}\cdot\hat{\mathbf{n}} = \begin{cases} M_s & (z=z_2) \\ -M_s & (z=z_1) \end{cases} \tag{2}$$

In Cartesian coordinates the integral form of the magnetic flux is found as in Equation 3 using Equations 1 and 2 [15].

$$\mathbf{B}(x,y,z) = \frac{\mu_0 M_s}{4\pi}\left(\int_{y_1}^{y_2}\int_{x_1}^{x_2}\frac{((x-x')\hat{\mathbf{x}}+(y-y')\hat{\mathbf{y}}+(z-z_2)\hat{\mathbf{z}})}{((x-x')^2+(y-y')^2+(z-z_2)^2)^{3/2}}dx'dy' - \int_{y_1}^{y_2}\int_{x_1}^{x_2}\frac{((x-x')\hat{\mathbf{x}}+(y-y')\hat{\mathbf{y}}+(z-z_1)\hat{\mathbf{z}})}{((x-x')^2+(y-y')^2+(z-z_1)^2)^{3/2}}dx'dy'\right) \tag{3}$$

At Equation 3; The expressions (*x, y, z*) represent the coordinates of the point where the flux value is calculated, and (x', y', z_1, z_2) represent the coordinates (boundaries) of the magnet. Since **B**(*x,y,z*) equation is vectorial, the x, y and z components are calculated separately.

$$\mathbf{B}_x(x,y,z) = \frac{\mu_0 M_s}{4\pi}\sum_{k=1}^{2}(-1)^k\int_{y_1}^{y_2}\int_{x_1}^{x_2}\frac{(x-x')dx'dy'}{((x-x')^2+(y-y')^2+(z-z_k)^2)^{3/2}}$$
$$= \frac{\mu_0 M_s}{4\pi}\sum_{k=1}^{2}\sum_{m=1}^{2}(-1)^{k+m}\int_{y_1}^{y_2}\frac{dy'}{((x-x_m)^2+(y-y')^2+(z-z_k)^2)^{1/2}} \tag{4}$$
$$= \frac{\mu_0 M_s}{4\pi}\sum_{k=1}^{2}\sum_{m=1}^{2}(-1)^{k+m}\ln\left(\frac{(y-y_1)+((x-x_m)^2+(y-y_1)^2+(z-z_k)^2)^{1/2}}{(y-y_2)+((x-x_m)^2+(y-y_2)^2+(z-z_k)^2)^{1/2}}\right)$$

$$\mathbf{B}_y(x,y,z) = \frac{\mu_0 M_s}{4\pi}\sum_{k=1}^{2}(-1)^k\int_{y_1}^{y_2}\int_{x_1}^{x_2}\frac{(y-y')dx'dy'}{((x-x')^2+(y-y')^2+(z-z_k)^2)^{3/2}}$$
$$= \frac{\mu_0 M_s}{4\pi}\sum_{k=1}^{2}\sum_{m=1}^{2}(-1)^{k+m}\int_{x_1}^{x_2}\frac{dx'}{((x-x')^2+(y-y_m)^2+(z-z_k)^2)^{1/2}} \tag{5}$$
$$= \frac{\mu_0 M_s}{4\pi}\sum_{k=1}^{2}\sum_{m=1}^{2}(-1)^{k+m}\ln\left(\frac{(x-x_1)+((x-x_1)^2+(y-y_m)^2+(z-z_k)^2)^{1/2}}{(x-x_2)+((x-x_2)^2+(y-y_m)^2+(z-z_k)^2)^{1/2}}\right)$$

$$\mathbf{B}_z(x,y,z)=\frac{\mu_0 M_s}{4\pi}\sum_{k=1}^{2}(-1)^k\int_{y_1}^{y_2}\int_{x_1}^{x_2}\frac{(z-z_k)dx'dy'}{((x-x')^2+(y-y')^2+(z-z_k)^2)^{3/2}}$$

$$=\frac{\mu_0 M_s}{4\pi}\sum_{k=1}^{2}(-1)^k\int_{y_1}^{y_2}\int_{x-x_1}^{x-x_2}\frac{(z-z_k)d\alpha dy'}{(\alpha^2+(y-y')^2+(z-z_k)^2)^{3/2}},\qquad \alpha=x-x'$$

$$=\frac{\mu_0 M_s}{4\pi}\sum_{k=1}^{2}\sum_{n=1}^{2}(-1)^{k+n+1}(z-z_k)(x-x_n)\int_{y_1}^{y_2}\frac{dy'}{\left[(y-y')^2+(z-z_k)^2\right]\left((y-y')^2+(x-x_n)^2+(z-z_k)^2\right)^{1/2}} \tag{6}$$

$$=\frac{\mu_0 M_s}{4\pi}\sum_{k=1}^{2}\sum_{n=1}^{2}\sum_{m=1}^{2}(-1)^{k+n+m}\arctan\left[\frac{(x-x_n)(y-y_m)}{(z-z_k)}\frac{1}{\left((x-x_n)^2+(y-y_m)^2+(z-z_k)\right)^{1/2}}\right]$$

$$\mathbf{B}(x,y,z)=B_x(x,y,z)\hat{\mathbf{x}}+B_y(x,y,z)\hat{\mathbf{y}}+B_z(x,y,z)\hat{\mathbf{z}} \tag{6b}$$

The magnet boundaries specified in Equations 4, 5 and 6 will be as follows, as shown in Figure 3.

$$(x_1,y_1,z_1)=-a,\ (x_2,y_2,z_2)=a$$

The magnetic flux equations obtained are defined according to the magnet's own local coordinate system. However, calculations need to be made in the global coordinate system in which the magnet and sensors are located together as shown in Figure 5. For this, when calculating the magnetic flux value of any point in space, this point must be reduced to the local coordinate of the magnet with transformation matrices.

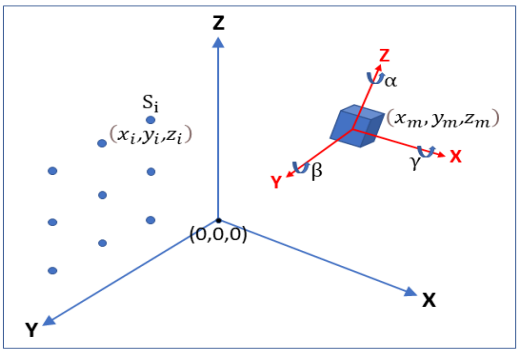

Figure 5. Global and Local Coordinate System of the Magnet

When Figure 5 is examined, Si represents the sensor on the body and (x_i, y_i, z_i) are the sensor location, (x_m, y_m, z_m) represents the magnet (capsule) position, and (γ,β,α) represents the magnet angles. The rotation matrix (**R**) calculated between the two coordinate systems is as in Equation 7.

$$\mathbf{R}=\begin{bmatrix}\cos(\alpha).\cos(\beta) & \cos(\alpha).\sin(\beta).\sin(\gamma)-\sin(\alpha).\cos(\gamma) & \cos(\alpha).\sin(\beta).\cos(\gamma)+\sin(\alpha).\sin(\gamma)\\ \sin(\alpha).\cos(\beta) & \sin(\alpha).\sin(\beta).\sin(\gamma)+\cos(\alpha).\cos(\gamma) & \sin(\alpha).\sin(\beta).\cos(\gamma)-\cos(\alpha).\sin(\gamma)\\ -\sin(\beta) & \cos(\beta).\sin(\gamma) & \cos(\beta).\cos(\gamma)\end{bmatrix} \tag{7}$$

In order to find the unknown positions and angles of the magnet ($x_m, y_m, z_m, \gamma, \beta, \alpha$), known sensor positions and magnetic flux values measured by sensors are used. As a result, the 6 unknown parameters of the magnet are calculated by Equation 8.

$$\begin{aligned}(B_{Xi},B_{Yi},B_{Zi})&=\mathbf{B}(x_{iL},y_{iL},z_{iL}).\mathbf{R}\\(x_{iL},y_{iL},z_{iL})&=\left[(x_i,y_i,z_i)-(x_m,y_m,z_m)\right].\mathbf{R}^{-1}\end{aligned} \tag{8}$$

where (x_{iL}, y_{iL}, z_{iL}) are the position of the ith sensor with respect to local coordinate system, **B** is the analytical magnetic flux vector at the Equation 6b and (B_{Xi}, B_{Yi}, B_{Zi}) are the measured magnetic flux value of the ith sensor. In the equation here, flux values and sensor coordinates measured by the sensors are known, and it is aimed to obtain magnet positions and angles. Since there are 6 unknowns in total, a minimum of 6 sensor data

is required. As a result, optimization algorithms are used to calculate magnet position and orientation parameters which are unknown in the equation. The optimization algorithm tries to predict the magnet positions and angles that will provide the magnetic flux values calculated by the sensors. For this, the cost function given in Equation 9 is used in the optimization algorithm.

$$\varepsilon = \sum_{i=1}^{N} \left[(B_{xi} - \hat{B}_{xi})^2 + (B_{yi} - \hat{B}_{yi})^2 + (B_{zi} - \hat{B}_{zi})^2 \right] \tag{9}$$

where (B_{xi}, B_{yi}, B_{zi}) are the known calculated magnetic flux value of the ith sensor, $(\hat{B}_{xi}, \hat{B}_{yi}, \hat{B}_{zi})$ are the estimated magnetic flux value by optimization algorithm, *N* is the number of the sensor and ε is the error. The optimization algorithm aims to minimize this error value, ideally to make it 0.

3.2. LM Algorithm and ABC Optimization Algorithm

Artificial Bee Colony algorithm is an algorithm based on swarm intelligence such as Ant Colony Optimization, Particle Swarm Optimization, Artificial Fish Swarm Algorithm etc. The ABC algorithm is the adaptation of the intelligent behaviors of bees while finding nectar in nature to optimization algorithms [12]. Although the ABC algorithm provides satisfactory results when used alone, it is relatively slow in terms of computation time [16], like other swarm intelligence based algorithms. Therefore, the ABC algorithm is not used to find the exact magnet positions and angles, but to create an initial value for the LM algorithm.

Levenberg-Marquardt algorithm is the most widely used method in the literature to solve nonlinear least squares problems. LM algorithm basically uses Gradient-descent and Gauss-Newton methods in a single algorithm [11]. This enables the LM algorithm to provide both fast and precise solutions in the calculation of nonlinear equations. The disadvantage of the LM algorithm is that it requires precise initial values to produce solutions. If the initial values are unrealistic, the algorithm performance decreases significantly. For this reason, ABC and LM algorithms are used together in this study to complement each other.

Finally, performance analysis of the magnet position and angle values estimated by ABC-LM algorithms is made. For this purpose, the equations given in Equations 10 and 11 are used.

$$E_P = \sqrt{(x_m - \hat{x}_m)^2 + (y_m - \hat{y}_m)^2 + (z_m - \hat{z}_m)^2} \tag{10}$$

$$E_O = \cos^{-1}(\vec{V}_{real}(\gamma, \beta, \alpha) \cdot \vec{V}_{est}(\hat{\gamma}, \hat{\beta}, \hat{\alpha})) \tag{11}$$

where $(x_m, y_m, z_m, \gamma, \beta, \alpha)$ are the known real location parameters of the magnet, $(\hat{x}_m, \hat{y}_m, \hat{z}_m, \hat{\gamma}, \hat{\beta}, \hat{\alpha})$ are the estimated location parameters, E_P is the position estimation error and E_O is the orientation estimation error.

4. RESULTS

While estimating 5D position and angle of the wireless capsule, the simulation conditions given in Section 2 and localization algorithm given in Section 3 were used. ABC and LM algorithms were used together in all simulations and the parameters outside the population were kept constant. Since ABC and LM algorithms give different results in each iteration in the same run, the algorithms were run 10 times in each scenario and the averaged results were obtained. In simulations, wireless capsule localization process was performed for 5 different population numbers of ABC algorithm and the results obtained for 80 different points were averaged. These comparative results are given in Table 1.

Table 1. Comparison of capsule positioning performance depending on ABC population size

Population size of the ABC Algorithm	Mean Position Error (mm)	Max. Position Error (mm)	Mean Orientation Error (˚)	Max. Orientation Error (˚)	Time per Calculation (sn)
10	1,679	17,780	2,688	48,241	0,263
20	1,126	12,041	1,823	36,938	0,449
30	0,769	10,949	1,227	21,998	0,616
40	0,630	5,716	1,037	17,261	0,800
50	0,596	6,547	0,962	15,236	1,018

When the table is examined, it is seen that as the population number increases, position and angle errors decrease, and the calculation time increases. It is seen that the result is less than 1 second in all scenarios, also the average position error and the average angle error are below 1.7 mm and 2.7˚, respectively. The results of position error and angle error for 30 population size scenario are given in Figure 6 and Figure 7.

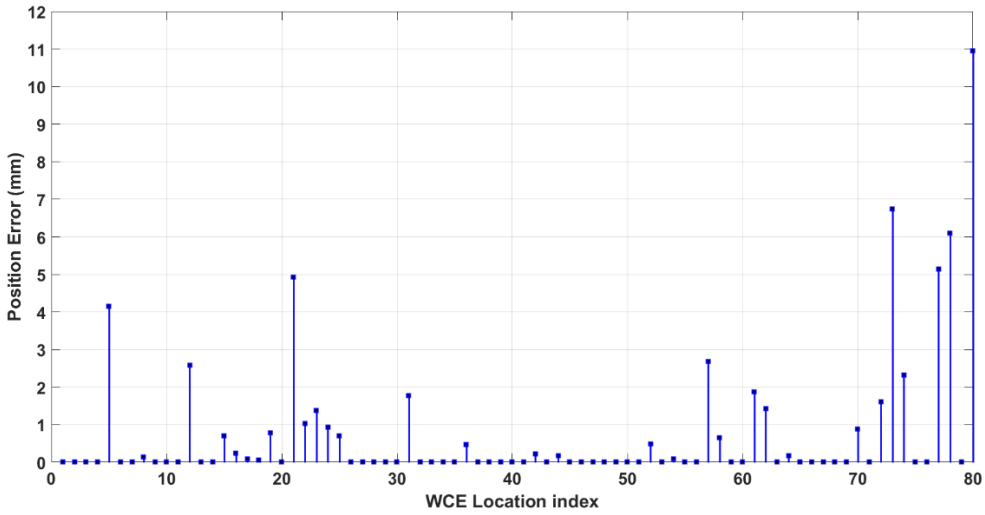

Figure 6. Position Error for ABC with 30 populations

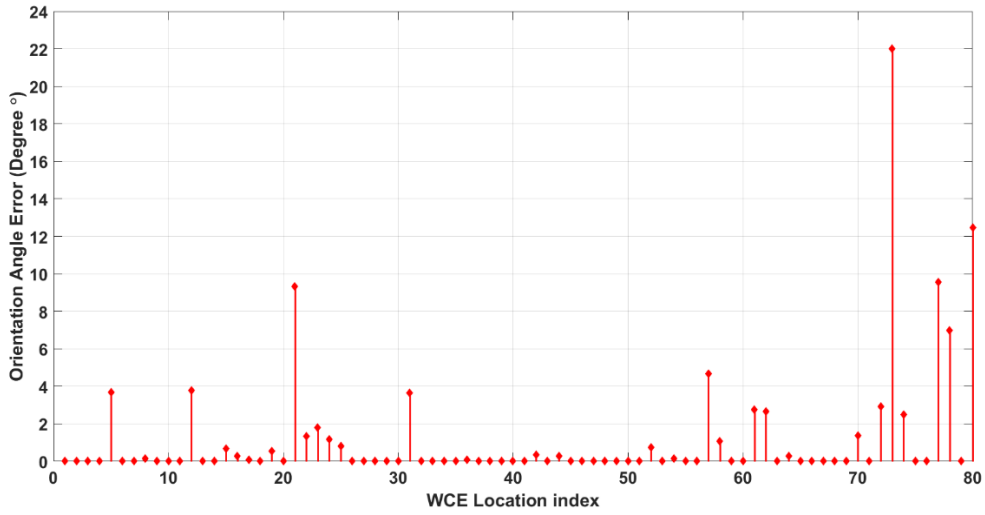

Figure 7. Orientation Error for ABC with 30 populations

When the figures obtained for 30 populations are examined, the position error of 71 out of 80 capsule locations (89%) is less than 2 mm. Similarly, the orientation angle error of 67 out of 80 capsule locations (84%) is less than 2˚. Also, analysis for each point was completed in about 0.6 seconds for 30 population scenario. These errors will come to much lower levels in offline working conditions and higher population values. However, in this study, a low number of populations were used in order to prepare for real-time simulations. These results pave the way for solving precise WCE localization problems in real time.

5. CONCLUSIONS

In this paper, we discussed the problem of localization of the wireless capsule in the small intestine using analytical model of the cube shaped magnet. In the estimation of capsule positions and angles, the results for different population scenarios were investigated by using both ABC and LM optimization algorithms. Our

results show that the mean position error value is below 1.68 mm and these results are obtained in a maximum of 1 second. Results can pave the way for more accurate localization in the wireless capsule endoscopy field.

ACKNOWLEDGMENT

This study was supported by the Erciyes University Scientific Research Projects Unit under grant number FDK-2018-7833.

REFERENCES

[1] P. Swain, G. J. Iddan, G. Meron, and A. Glukhovsky, "Wireless capsule endoscopy of the small bowel: development, testing, and first human trials," in *Biomonitoring and Endoscopy Technologies*, 2001, pp. 19-24.
[2] J. L. Toennies, G. Tortora, M. Simi, P. Valdastri, and R. J. Webster, "Swallowable medical devices for diagnosis and surgery: the state of the art," *Proceedings of the Institution of Mechanical Engineers, Part C: Journal of Mechanical Engineering Science*, vol. 224, pp. 1397-1414, 2010.
[3] G. Ciuti, A. Menciassi, and P. Dario, "Capsule endoscopy: from current achievements to open challenges," *IEEE reviews in biomedical engineering*, vol. 4, pp. 59-72, 2011.
[4] T. D. Than, G. Alici, H. Zhou, and W. Li, "A review of localization systems for robotic endoscopic capsules," *IEEE Transactions on Biomedical Engineering*, vol. 59, pp. 2387-2399, 2012.
[5] R. Kuth, J. Reinschke, and R. Rockelein, "Method for determining the position and orientation of an endoscopy capsule guided through an examination object by using a navigating magnetic field generated by means of a navigation device," ed: Google Patents, 2007.
[6] K. Yu, G. Fang, and E. Dutkiewicz, "Position and orientation accuracy analysis for wireless endoscope magnetic field based localization system design," in *2010 IEEE Wireless Communication and Networking Conference*, 2010, pp. 1-6.
[7] M. Kanaan and M. Suveren, "A novel frequency-dependent path loss model for ultra wideband implant body area networks," *Measurement*, vol. 68, pp. 117-127, 2015.
[8] M. Suveren, "Ultra Wide Band (UWB) Wireless Systems in Implant Body Area Networks and Modelling of the Distance Measurement Error," MSc Master Thesis, Mechatronic Engineering, Erciyes University, Kayseri, 2015.
[9] S. M. Aziz, M. Grcic, and T. Vaithianathan, "A real-time tracking system for an endoscopic capsule using multiple magnetic sensors," *Smart Sensors and Sensing Technology*, pp. 201-218, 2008.
[10] N. Atuegwu and R. Galloway, "Volumetric characterization of the Aurora magnetic tracker system for image-guided transorbital endoscopic procedures," *Physics in medicine and biology*, vol. 53, p. 4355, 2008.
[11] H. Gavin, "The Levenberg-Marquardt method for nonlinear least squares curve-fitting problems. 2011," *Availble Online from: http://people. duke. edu/~ hpgavin/ce281/lm. pdf..(Accessed 16 April 2019)*, 2016.
[12] D. Karaboga and B. Basturk, "A powerful and efficient algorithm for numerical function optimization: artificial bee colony (ABC) algorithm," *Journal of global optimization*, vol. 39, pp. 459-471, 2007.
[13] M. Suveren and M. Kanaan, "On the Use of Human Body Models in Wireless Capsule Endoscopy Localization based on Ultra Wide Band Signaling," in *5th International Conference on Engineering and Natural Sciences (ICENS)*, Prague, 2019.
[14] M. J. Ackerman, " Viewpoint: The Visible Human Project, Journal Biocommunication, 18,2, p. 14.," 1991.
[15] E. P. Furlani, *Permanent magnet and electromechanical devices: materials, analysis, and applications*: Academic press, 2001.
[16] M. Suveren and M. Kanaan, "5D Magnetic Localization for Wireless Capsule Endoscopy Using the Levenberg-Marquardt Method and Artificial Bee Colony Algorithm," in *2019 IEEE 30th International Symposium on Personal, Indoor and Mobile Radio Communications (PIMRC Workshops)*, 2019, pp. 1-6.

ICENS 6TH INTERNATIONAL CONFERENCE ON ENGINEERING AND NATURAL SCIENCE
October 21-25 2020 Belgrade

Structural Rehabilitation of a Damaged Retaining Wall: Structural approach and modeling

Baris Gunes[1], Cihan Oser[2], Baris Sayin[3]

Abstract

Retaining walls are rigid structures built to support the natural or back filling soils at different elevations. Although these type of walls are generally composed of reinforced concrete walls or gravity stone walls, geosynthetic reinforced wall systems are also frequently preferred in recent years. Geosynthetic reinforced walls are defined as a composite wall system constructed by mechanically compacting the geosynthetic reinforcement material placed between the back filling soil layers behind the wall. The quality of the backfill behind the wall and the presence of water are very important in geosynthetic reinforced walls as in general of retaining structures. Applications that are not compatible with static calculations may cause the wall to be exposed to loads higher than the design loads due to the inability to remove the water. As a result of this situation, it is possible to encounter visible damage to the structure. In the presented study, the structural rehabilitation of a high geosynthetic reinforced wall constructed in two stages is described. Damages occurred on the examined wall due to the reasons mentioned above and thus the necessity of repair / strengthening emerged. In this context, a new RC retaining wall with piles and buttresses was designed in front of the lower level of the wall. The new wall has been modeled in Midas GEN software, and the segments of the new wall, foundation and buttresses were modelled with "Plate" elements, and piles were modelled with "Frame" elements. p-y, t-z and Q-z springs were calculated according to the soil structure to reflect the interaction between pile-soil. The nonlinear load-displacement behavior of the springs was applied to the pile points in the analysis model. The strength and bearing strength of the walls, buttresses, foundations and piles were checked by nonlinear analysis. The presented study is expected to be a useful tool in terms of determining the method to be applied in the design of retaining walls under earthquake and service loads and the parameters to be taken into account for the rehabilitation of an existing retaining structure.

Keywords: Retaining wall hazards, Structural rehabilitation, Structural modeling technique

1. INTRODUCTION

Retaining systems are constructed to support back soil during excavation and construction sequence. The structures are widely used as a part of numerous structural designing activities. A proper design of a retaining system must prevent the failure and avoid damage to existing nearby structures [1]. Retaining structures can be displaced too much due to reasons such as incorrect determination of soil parameters, not properly modeling the soil environment, designing horizontal and vertical retaining elements without sufficient strength [2]. However, geosynthetically reinforced walls are preferred, especially because they can reach to heights that known retaining structures cannot reach and they show sufficient performance under high earthquake loads. Retaining walls built with MSE technology in the US in the last 40 years have found a great application area as an alternative to reinforced concrete and earth retaining walls. The geosynthetic reinforcements (geotextile or geogrid) are used in the filling to compensate the horizontal ground loads that the filling material exerts on the wall edges as tensile force. The filling material that is reinforced with geosynthetic reinforcements prevents sliding surfaces and allows very steep fill slopes [3].

[1] *Istanbul University-Cerrahpasa, Department of Civil Engineering, 34320, Istanbul, Turkey. bgunes@istanbul.edu.tr*

[2] *Istanbul University-Cerrahpasa, Department of Civil Engineering, 34320, Istanbul, Turkey. oser@istanbul.edu.tr*

[3] *Corresponding author: Istanbul University-Cerrahpasa, Department of Civil Engineering, 34320, Istanbul, Turkey. barsayin@istanbul.edu.tr*

In the literature, various approaches are presented based on experimental and numerical studies regarding retaining walls. Xu et al. [4] presented a numerical modeling study on the bearing capacity of two-tiered reinforced soil retaining walls. In this scope, numerical simulations are performed using the finite element limit analysis method. Liu et al. [5] studied experimentally the seismic performance of soilbags-built retaining wall model. Chen et al. [6] proposed a new capillary barrier concept to form a back-filled retaining wall to reduce water infiltration under rainfall. Xu et al. [7] developed a new method for rotational stability analysis of reinforced soil retaining walls based on the log-spiral failure mechanism. The proposed method is validated against the results from different pseudo-static methods. Wang et al. [8] conducted to a model tests and the numerical simulations to obtain the wall face horizontal displacement, vertical and horizontal soil pressures, and geogrid strains to understand the structural behavior of geogrid reinforced soil retaining walls with a deformation buffer zone under static loads. Liu et al. [9] presented a field study of constructing retaining walls using soilbags that are formed by filling the excavated clayey soils into woven bags. Li et al. [10] proposed an analytical approach for the seismic stability analysis of gravity retaining wall.

In the study, construction methods to rehabilitate and to increase the stability of a geosynthetic reinforced structure is presented. The existing wall was constructed as two stepped in vertical direction. Initially, a new RC retaining wall with piles and buttresses was designed in front of the lower part of the wall at the first phase. Secondly, the increment at the stability of the retaining system and the displacement of the current wall was determined by using finite element analysis software.

2. MODELLING

The material information used in the modeling of the retaining wall examined is given in Table 1. Midas Gen v2020 software [11] was used for structural analysis. In determining soil parameters, Soil Data and Geotechnical Evaluation reports were taken as basis [12, 13]. Accordingly, the unit weight of the backfill filling is 22 and 20 kN/m^3 for the upper and lower parts, respectively, and the shear strength angle (ϕ) is 27°. The loads acting on the structure are determined as dead loads, static and dynamic soil pressures and hydrostatic loads. For the calculation of soil pressures, the seismic parameters of the building were determined at first (Table 2).

Table 1. Materials

Material	Class	Code
Concrete for RC	C35/37	TS-EN-206, 2014
Concrete for only concrete	C14/16	TS-EN-206, 2014
Steel class	B420C	TS708, 2010

Table 2. Seismic parameters for the structure

Parameter	Value
Spectral acceleration coefficient for short period (S_S)	0.967g
Spectral acceleration coefficient for 1 sec. period (S_1)	0.272g
Local soil class	ZC
Local soil impact factors for short period zone, F_S	1.2
Local soil impact factors for period=1.0 sec., F_1	1.5
S_{DS}	1.16
S_{D1}	0.41

The behavior coefficient (r) of the retaining structure was taken as 1.50. Following the earthquake parameters, static and dynamic soil pressures affecting the structure were calculated. Accordingly, the unit volume weight of the backfilling soil is 22 kN/m^3, the saturated unit weight is 23 kN/m^3, and the shear strength angle is 27°. The soil has been determined as an impermeable soil. Surcharge load was applied as 95 kN/m^2 (90 kN/m^2 backfill + 5 kN/m^2 live load, other etc.) Active static and dynamic pressure coefficients were found to be 0.376 and 1.028, respectively. Soil pressures are calculated based on the values. The load combinations used in the design are based on AASHTO [14]. Load combinations are presented in Table 3.

Table 3. Load combinations

Str1_EH(yn)_a	1.25DC + 1.50EH(a) + 1.50ES(a) + 1.00WA
Str1_EH(yn)_b	0.90DC + 1.50EH(a) + 1.50ES(a) + 1.00WA
Ext1_EQ(yn)_a	1.00DC+1.00EH(a)+1.00ES(a)+1.00EH(q)+1.00ES(q)
Srv1_EH(yn)_a	1.00DC + 1.00EH(a) + 1.00ES(a) + 1.00WA

In the analysis model, wall, strut and foundation elements are modeled as "Plate" and pile elements as "Frame". The analysis model is given in Figure 1. In Figure 2, soil, surcharge and water pressures affecting the structure are shown. According to TBDY-2018, Q-Z, t-z and p-y springs must be defined respectively for bearing capacity of piles, friction load capacity of piles and pile lateral bearing capacity to reflect the soil-pile-structure interaction. The soil environment in which the piles are located was modeled in Pileaxl and Pilelat software and the relevant spring values were obtained. The calculations were made with the assumption that the piles would be inserted into the existing claystone layer up to 5 diameters. In Figure 3, the behavior of the soil and pile sections, Q-Z, t-z and p-y arcs are shown, respectively.

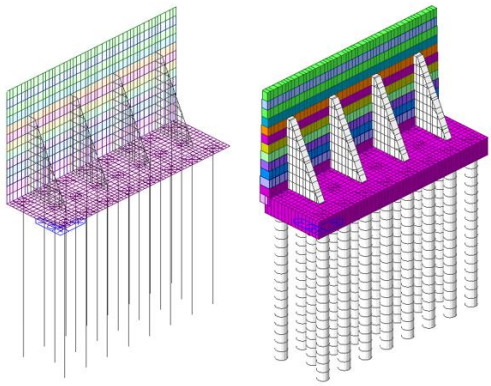

Figure 1. 3D model

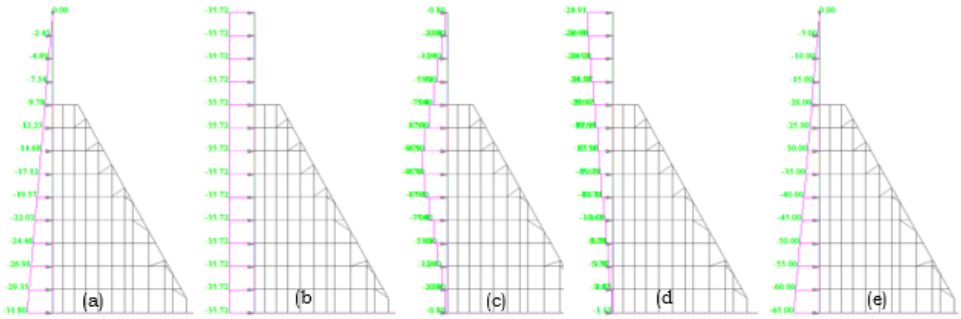

Figure 2. (a,b) Active static ground and surcharge pressure, (c,d) Active dynamic ground and surcharge pressure, (e) Hydrostatic pressure (kN/m^2

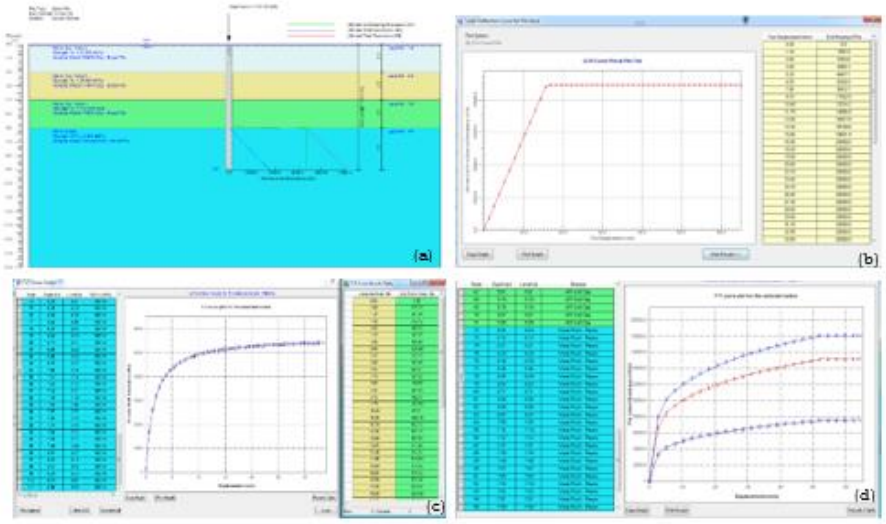

Figure 5. (a) The section of soil and pile, (b) Q-Z spring stiffness at pile tip, (c) T-z friction spring stiffness in the claystone-quartzite part of the pile, (d) P-y lateral spring stiffness determined along the height in the stiff clay and claystone-quartzite part of the pile

Environmental friction resistance is accepted for cohesive soils. However, here the α coefficient was taken as 0 for the clayey part in the piles that were socketed in a very rigid layer according to the environment. According to TBDY-2018 Section 16C, the group effect on p-y springs was calculated and applied to the model. Some views of Q-Z, t-z and p-y arcs are given in Figure 4.

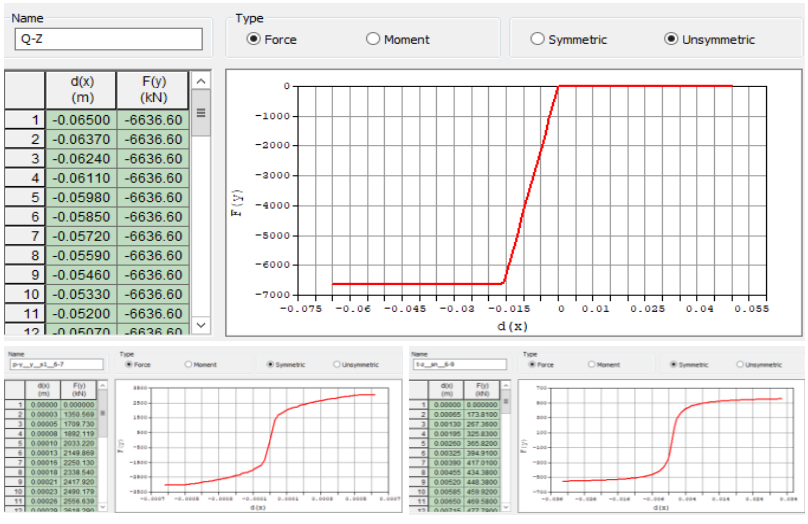

Figure 4. Sample view from Q-Z, p-y and t-z arcs defined in the static analysis model

3.RESULTS AND DISCUSSION

3.1 Analysis results

In this section, static analysis results, internal effects and displacements are given. Some of the internal effects provided in the structural elements are presented in Figures 5 to 8.

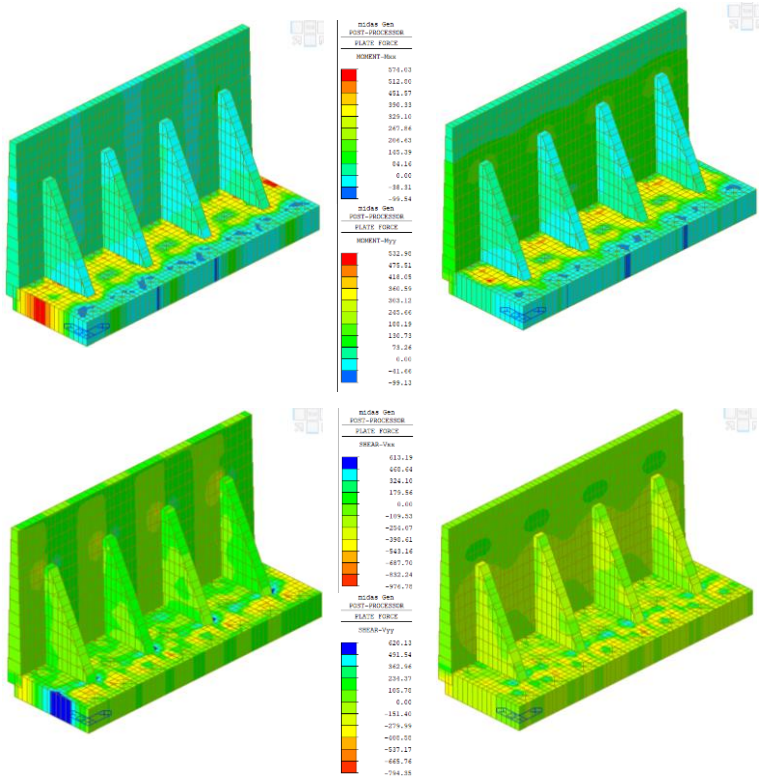

Figure 5. Mxx and Myy moments provided in Str1a loading (up), Vxx and Vyy forces provided in Str1a loading (down) (kN/m)

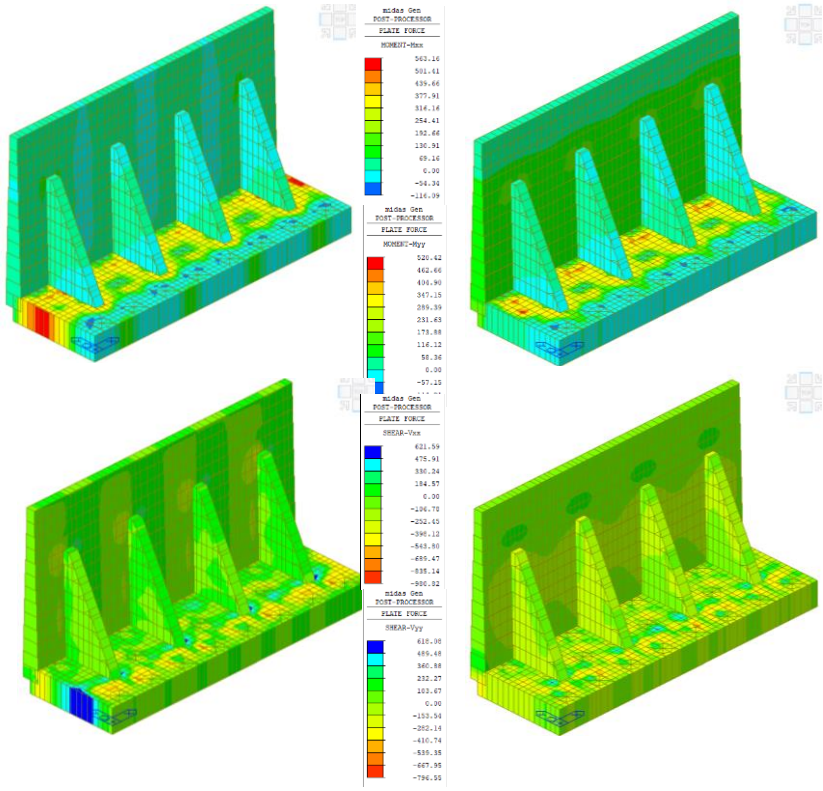

Figure 6. (a) Mxx and Myy moments provided in Ext1a loading (up) kNm/m), Vxx and Vyy forces provided in Ext1a loading (down) (kN/m)

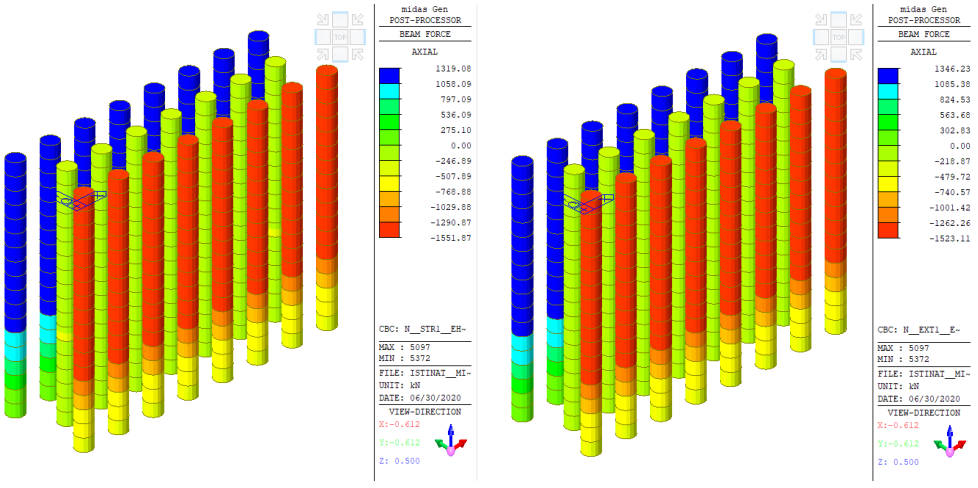

Figure 7. Axial force provided in Str1a ve Ext1a loadings for piles (kN)

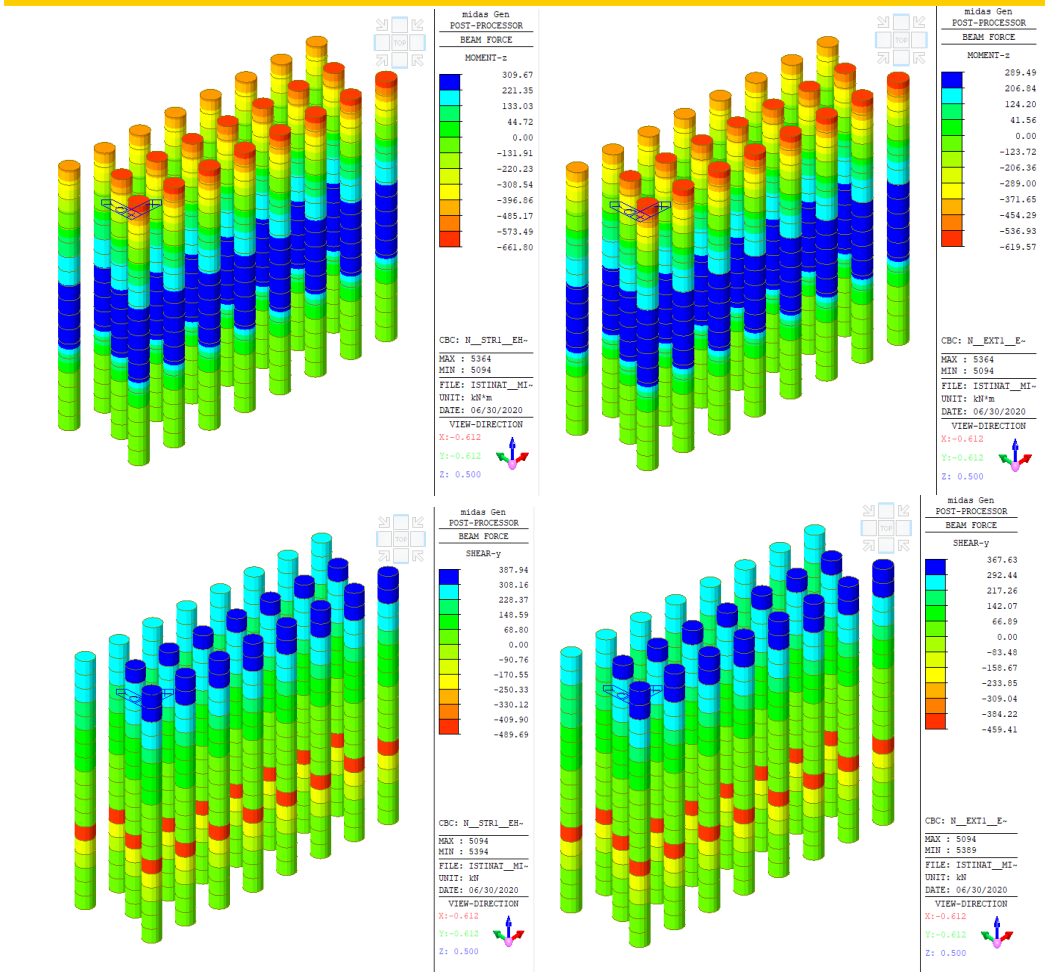

Figure 8. (a) Moment provided in Str1a ve Ext1a loadings for piles (kNm) (up), Shear force provided in Str1a loading for piles (kN) (down)

The displacements under service and earthquake loadings are shown in Figure 9. Displacements were obtained as 19.11 and 26.07 mm, respectively.

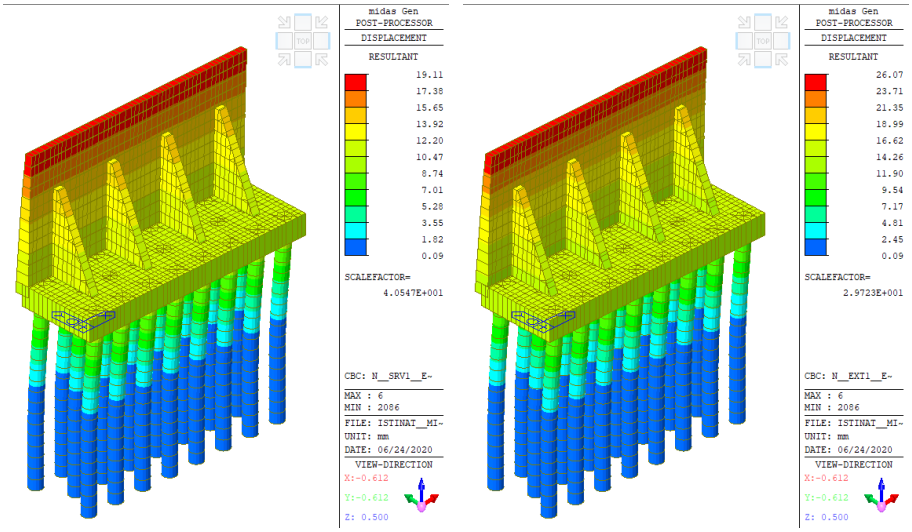

Figure 9. The displacements provided in service(left) ve earthquake (right) (mm)

3.2 Design

In this section, rebar properties, bending and shear checkings, and pile carrying capacity are presented. Ø20/15 vertical and Ø20/15 lateral rebars are used in the walls and struts. Basically, there are Ø20/15 rebars in both directions, top and bottom. Within the scope of bending checking, shear wall, buttress and foundation bending effect / capacity ratios and checkings were carried out. Wall and strut are presented in Figure 10 and foundation impact / capacity ratios are presented in Figure 11.

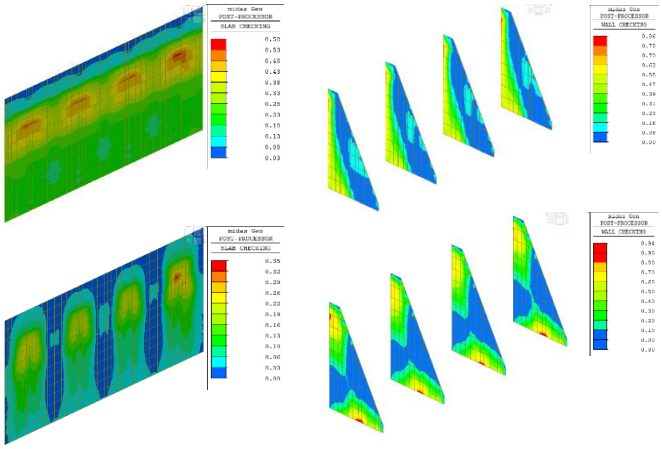

Figure 10. Demand/capacity ratios. Vertical (left-top) and lateral (left-down) for shear wall, Vertical (right-top) and lateral (right-down) for strut

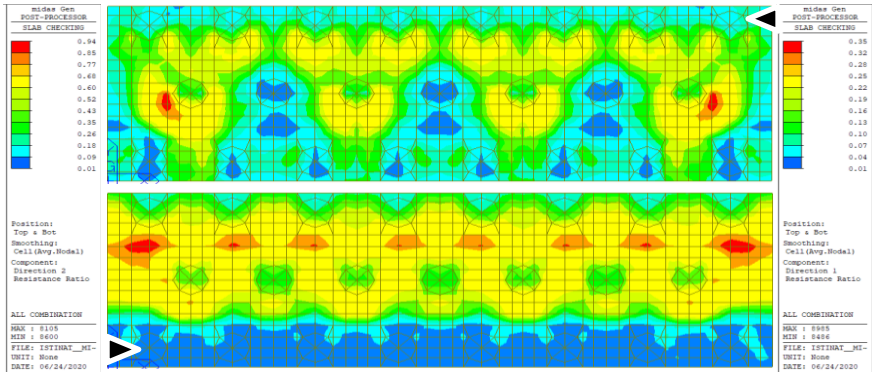

Figure 11. Demand/capacity ratios for long direction (up) and short direction (down) in the foundation

Shear checkings were carried out based on the ACI 318-08 code for the shear wall, buttress and foundation elements. Shear rebar was added as half of the concrete shear capacity is less than the shear force exposed as a result of the shear checkings in shear wall and strut. 18 Ø26 longitudinal rebar and Ø14 spiral stirrups were used on the piles. Stirrup spacing is 8 cm. Figure 12 shows the demand/capacity ratios of the piles.

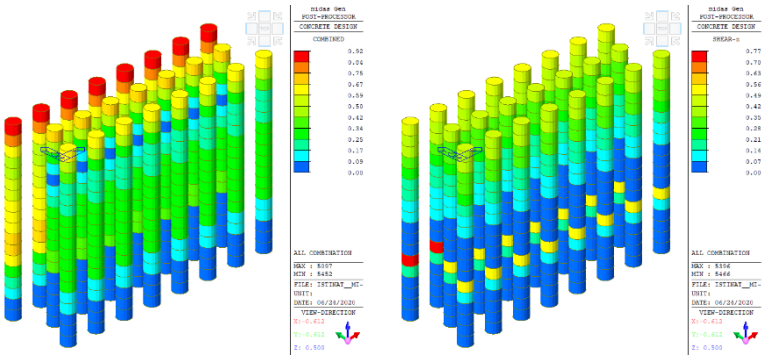

Figure 12. Demand/capacity ratios in bending (up) and shear (down) for the piles

Figure 13 shows the pile bearing capacity calculation. The obtained pile bearing capacities were reduced by dividing the perimeter friction pressure, friction tensile and end resistance into 1.5, 1.6 and 2.0 strength coefficients, respectively. For pile bearing capacity investigations, the highest pressure and tensile forces in earthquake and non-earthquake conditions were obtained, respectively, 1523 and 1346 kN, while the factored capacities of the piles were determined as 5646 and 2209 kN, respectively.

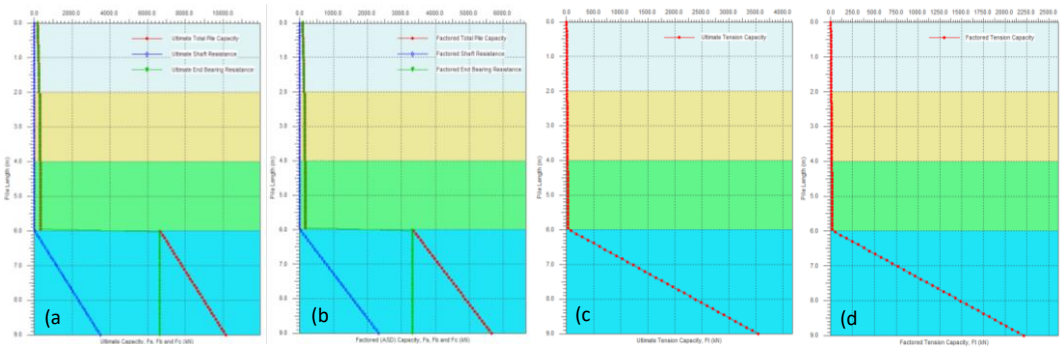

Figure 13. Ultimate and factored load-bearing capacity of the pile. (a,b) in compressive, (c,d) in tension

4. CONCLUSIONS

In this study, the design method of a retaining wall planned to be contructed in front of an existing wall in order to rehabilitate a partially damaged two-stage geosynthetic reinforced retaining structure is presented. In the design, it is accepted that the first level geowall has collapsed. With the soil parameters determined in line with this acceptance, a retaining wall was designed to ensure the structural safety of the part behind the wall. As a result of the analysis, the geometric properties, foundation width/thickness, height/thickness of the walls and buttresses of the retaining structure to be formed were determined. Rebar diameter, placement and spacing of the structural elements that make up the retaining structure have been established. The structural safety of the retaining wall was ensured by checking the diameter of the piles, rebars and bearing strength. The structural safety and stability of the system behind the wall has been established with the newly designed retaining wall.

REFERENCES

[1]. E. Saez, G.S. Pardo, C. Ledezma, Seismic response of a pile-supported excavation on Santiago gravel, Soil Dynamics and Earthquake Engineering, 76 (2015) 2–12.
[2]. Oser C., Sayin B. (2020) Geotechnical assessment and rehabilitation of retaining structures collapsed partially due to environmental effects, Engineering Failure Analysis, 119, 1-19.
[3]. Retaining walls (2020) Web site: https://www.movea.com.tr/istinat-duvarlari-ve-tipleri-nelerdir/ (Accessed on November 2020)
[4]. Bearing capacity and failure mechanisms of two-tiered reinforced soil retaining walls under footing load PengXu, Kianoosh Hatami, JingJing Bao, Ting Li, Computers and Geotechnics Volume 128, December 2020, 103833
[5]. Li S-H, Jia F., Chen X-L, Li L-J (2020) Experimental study on seismic response of soilbags-built retaining wall, Geotextiles and Geomembranes, 48, 5, 603-613.
[6]. Chen Y., Gao Y., Ng C.W.W. (2020) A new capillary barrier system for retaining wall backfilled with fine-grained soil, Computers and Geotechnics, 118, 103324
[7]. Xu P., Hatami K., Jiang G. (2020) Seismic rotational stability analysis of reinforced soil retaining walls, Computers and Geotechnics, 118, 103297
[8]. Wang H., Yang G., Wang Z., Liu W. (2020) Static structural behavior of geogrid reinforced soil retaining walls with a deformation buffer zone, Geotextiles and Geomembranes, 48, 374-379.
[9]. Liu S., Fan K., Xu S. (2019) Field study of a retaining wall constructed with clay-filled soilbags, Geotextiles and Geomembranes, 47, 1, 87-94.
[10]. Li X., Zhao S., He S., Yan Q., Lei X. (2019) Seismic stability analysis of gravity retaining wall supporting c–φ soil with cracks, Soils and Foundations, 59, 4, 1103-1111.
[11]. Midas Gen, (2018). Integrated Solution System for Building and General Structures. MIDAS Information Technology Co.
[12]. Soil report (2020) Geoloji Muhendislik Co.
[13]. Cinicioglu O. (2020) Geotechnical Assessment Report
[14]. AASHTO, 2017, LRFD Bridge Design Specifications, American Assosication of State Highway and Transportation Officials, Washington.

ICENS 6TH INTERNATIONAL CONFERENCE ON ENGINEERING AND NATURAL SCIENCE
October 21-25 2020 Belgrade

Structural Rehabilitation of a Damaged Retaining Wall: Geotechnical approach and modeling

Cihan Oser[1], Baris Gunes[2], Baris Sayin[3]

Abstract

Retaining walls are rigid structures built to support the natural or back filling soils at different elevations. Although the type of walls is generally composed of RC walls or gravity stone walls, geosynthetic reinforced wall systems are also frequently preferred in recent years. Geosynthetic reinforced walls are defined as a composite wall system constructed by mechanically compacting the geosynthetic reinforcement material placed between the back filling soil layers behind the wall. In this presented study, applications that are designed to strengthen and to increase the stability of a damaged high geosynthetic reinforced wall that was built in two stages are described. Within the scope of the study, a new RC retaining wall with piles and buttresses was designed in front of the lower part of the existing geosynthetic reinforced wall. Plaxis 2D and 3D finite element analysis software were used to determine the increment at the stability of the existing retaining system and to calculate the displacements of the current wall. Eleven-earthquake records were studied in accordance with Turkish Earthquake Building Code-2018 in order to calculate the stability, the displacements, and the internal forces of the piles under the foundation of newly designed reinforced concrete retaining wall. This study is expected to be a useful tool to reveal the parameters that should be taken into consideration in the seismic performance of the retaining walls that are going to be constructed to strengthen an existing retaining structure.

Keywords: Retaining walls, Seismic performance analysis, Finite element analysis, Turkish Earthquake Building Code-2018

1. INTRODUCTION

Retaining walls are rigid structures that are constructed for supporting the backfill or natural soil laterally at different levels on the two sides of the wall. In other words, these walls have the function of supporting the back soil against lateral movements [1]. Geosynthetic reinforced walls, which are a type of retaining walls, are defined as a composite wall system constructed by mechanically compressing the geosynthetic reinforcement material placed between the layers of backfill behind the wall. However, besides determining the structural safety conditions of such existing retaining structures, it may also be required to rehabilitate the walls for today's conditions.

Many studies have been conducted to determine the behavior of retaining walls within the scope of numerical analysis. McCombie et al. (2012) built and tested five full-scale dry stone walls until collapsed. It was concluded that the walls were ductile even though their components were brittle [2]. Fukumoto et al. (2014) studied the shape effect of the blocks in a dry-stone masonry retaining wall using numerical simulations and 3-D discrete elements method [3]. Casolo (2000) proposed a computational model for evaluating the dynamical response and the damage of large scale masonry walls subjected to out-of-plane seismic actions [4]. Nimbalkar and Choudhury (2007) presented a study about the design weight of the walls required under passive earth pressure conditions by using the pseudo-dynamic seismic forces acting both on the soil and the wall [5].

[1] *Istanbul University-Cerrahpasa, Department of Civil Engineering, 34320, Istanbul, Turkey. oser@istanbul.edu.tr*

[2] *Istanbul University-Cerrahpasa, Department of Civil Engineering, 34320, Istanbul, Turkey. bgunes@istanbul.edu.tr*

[3] *Corresponding author: Istanbul University-Cerrahpasa, Department of Civil Engineering, 34320, Istanbul, Turkey. barsayin@istanbul.edu.tr*

Villemus et al. (2007) studied the stability of retaining structures using experimental results and data obtained from the field. In this scope, a model was developed for calculating the stability of dry stone retaining walls. The data obtained from laboratory test results were used in a model based on the equilibrium of the forces at failure to quantify the interface friction. The model, that considered the possibility of the internal failure of the wall, was taking the irregularity of the geometry of the stones and their arrangement into account [6].

In the present research, it is aimed to rehabilitate, to strengthen and to increase the stability of a damaged geosynthetic reinforced wall. The existing geosynthetic reinforced wall was constructed as two staged in vertical direction. Within the scope of rehabilitation and strengthening, a new reinforced concrete retaining wall with piles and buttresses was designed in front of the lower part of the existing geosynthetic reinforced wall at the first phase. Secondly, the increment at the stability of the existing retaining system and the displacement of the current wall was determined by using Plaxis 2D and 3D finite element analysis software. Therefore, the structural parameters such as the stability of the entire retaining system, the displacements and the internal forces of the piles under the foundation of the newly designed reinforced concrete retaining wall were obtained.

2. THE RETAINING SYSTEM AND ANALYSES

It is planned to construct a new reinforced concrete retaining wall in order to rehabilitate an existing geosynthetic reinforced wall that is standing in front of a building. Within the scope of this study, numerical analyzes were performed to determine the structural safety level of the retaining system before and after the construction of the new reinforced concrete retaining wall. Plan view of the designed retaining wall is shown in Figure 1. Geotechnical site characterization was made by determining the current condition of the existing geosynthetic reinforced wall and investigating the soil profile. Then, the performance of the retaining system that is designed to build has been determined by using Plaxis 2D and 3D finite element analysis software under static and dynamic loading conditions. Soil investigation Report for the related site, Geotechnical Evaluation Report and also application project of the retaining wall were used in geotechnical analyses [7-9]. In this context, 2D and 3D analysis for static conditions, 2D and 3D pseudo-static analysis for DD-3 earthquake level, and 2D nonlinear time-history analysis for DD-2 earthquake level were performed. Hardening Soil Small Strain (HS-Small) model was preferred to use for the soil profile in the analysis. Properties of structural elements are given in Table 1 that are used in 2D and 3D analysis. The finite element model, construction stages, and the analyses and the controls for each stages are presented in Figure 2.

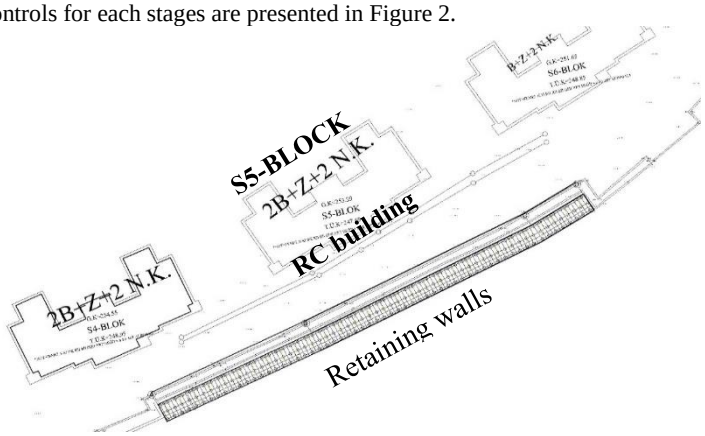

Figure 1. Plan view

Table 1. Definition of structural elements used in the analysis

Geotechnical analysis	Structural elements					
	Bored Piles	Foundation of RC retaining wall	Console of RC retaining wall	Buttresses of RC retaining wall	Infrastructure (pipe)	Geogrid
2D	Embedded beam	Plate	Plate	Elastic soil	Plate	Geogrid
3D	Embedded beam	Plate	Plate	Plate	Plate	Geogrid

2.1 Two Dimensional (2D) Finite Elements Analysis

The finite element analysis model that is consisted of the building, existing geosynthetic reinforced wall, newly designed reinforced concrete retaining wall with piles and buttresses is shown in Figure 2. The calculation stages and analysis methods are also given in the figure.

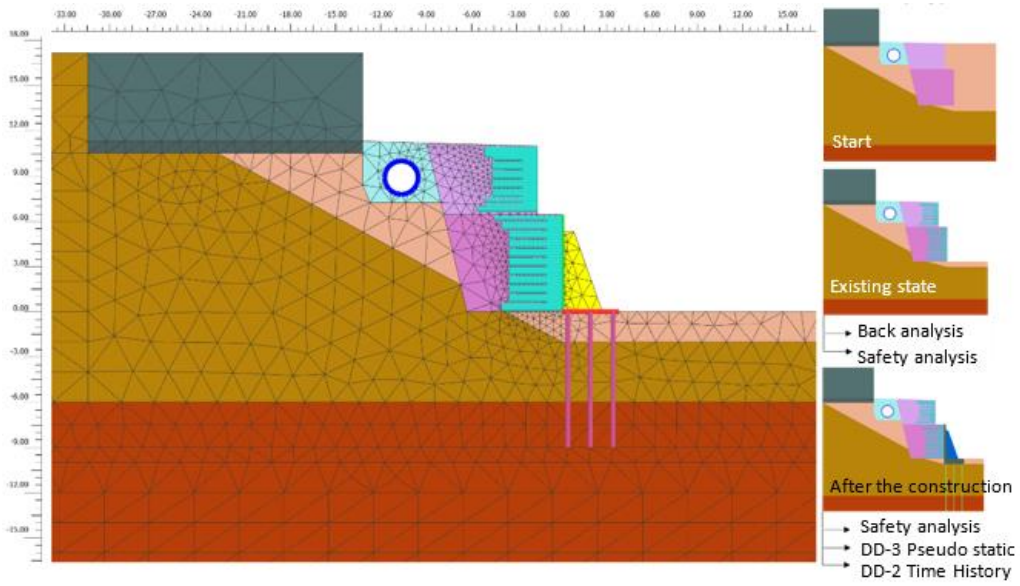

Figure 2. Finite elements analysis model (left), schematic presentation of calculation stages and analysis methods (right)

2.1.1 Back analysis for existing state

Back analysis were performed both for before and after the construction of new reinforced concrete retaining wall depending on the results of field observations and measurements. Lateral deformations and the safety analysis results obtained by the back analysis are given in Figures 3 and 4. The analysis results were obtained close to failure as expected. It was seen that, calculated lateral displacements (15 cm) were very close to the measurement results especially at top and bottom levels. Besides, it was observed that the geosynthetic reinforcements at the lower part of the wall reached their maximum capacity.

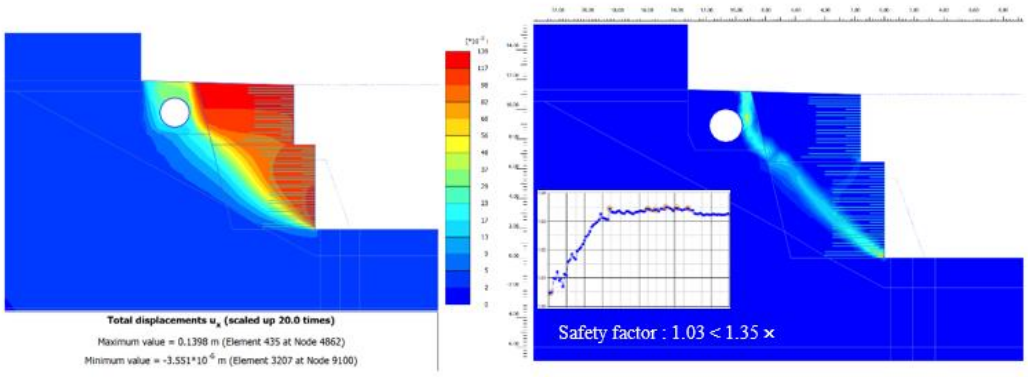

Figure 3. Lateral displacements for current state (before the construction of new designed wall) (left), Safety analysis for current state (right)

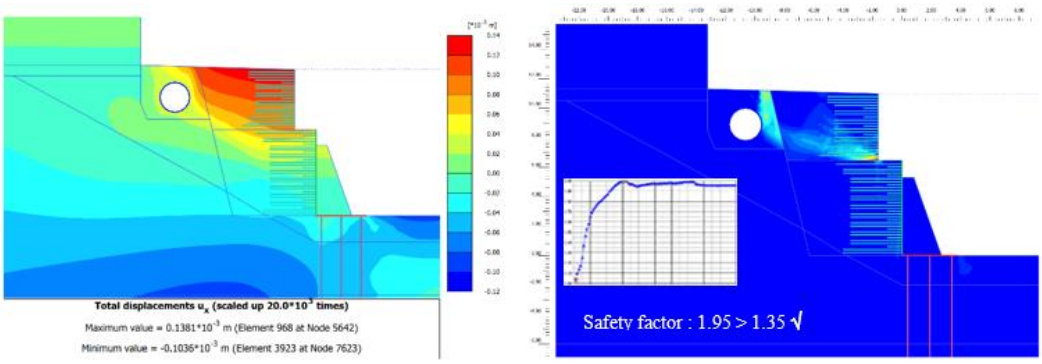

Figure 4. Lateral displacements after the construction of new designed wall (left), Safety analysis result after the construction of new designed wall (right)

2.1.2 Pseudo-Static analysis after the construction of new RC retaining wall for DD-3 earthquake level

Pseudo-static analysis were performed for the new designed RC retaining wall for the earthquake level DD-3 described in TBEC-2018 [10]. Lateral displacements and safety analysis results are given in Figure 5.

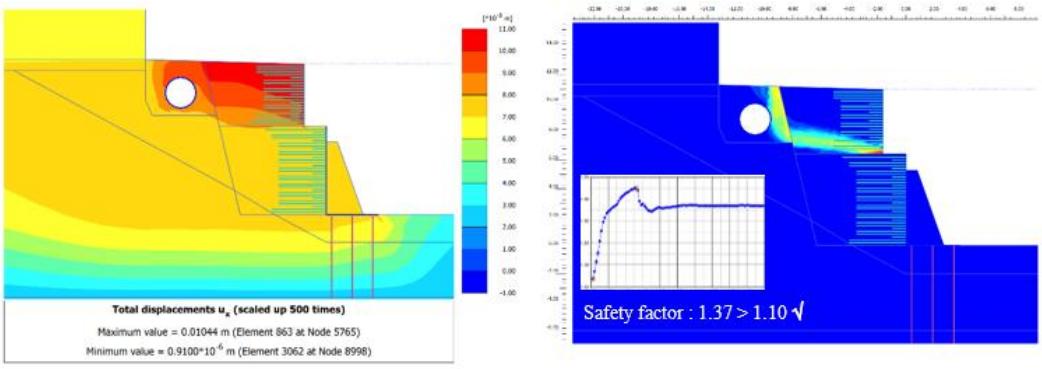

Figure 5. Lateral displacements after pseudo-static analysis for DD-3 earthquake level (left), Safety results of pseudo-static analysis for DD-3 earthquake level (right)

2.1.3 Time-History Analysis for the retaining system for DD-2 earthquake level

Database of "The Pacific Earthquake Engineering Research Center (PEER)" was used when selecting the earthquake records [11]. The selected earthquake records are given in Table 2. Separate filters were used for a large number of strike-slip faults and a small number of normal-slip faults affecting the studied area. Selected earthquake records were matched to design spectrum for ZC soil class at DD-2 earthquake level as mentioned in TBEC-2018 [10]. In this context, attention has been paid to keep the characteristic properties of earthquakes not to be disturbed. Although the average values of the records after the 1.5 second period remained below the design spectrum, compatible records with the design spectrum were used in short period intervals, which are dominant oscillation period of the retaining wall.

Additionally, the shear wave velocity (Vs) of the soil profile where the earthquake records will be acted on the model was taken as Vs=650 m/s. In this case, if the site specific design spectrum is determined, a smaller spectrum than the one recommended for ZC soil will be obtained. Therefore, the design spectrum used in the

study has been kept on the safe side (Figure 6). Lateral and vertical displacements obtained from E01 earthquake record which is one of the 11 selected earthquake are given in Figure 7.

Table 2. Parameters for selected earthquakes

Earthquake #	RSN #	Location	Fault	Mw	R_{jb} (km)	R_{rup} (km)	V_s30 (m/s)	PGA, max. compenent (g)	Scale factor
E01	33	Parkfield	SS	6.19	15.96	15.96	528	0.273	1.65
E02	145	Coyote Lake	SS	5.74	6.13	6.13	561	0.246	1.83
E03	243	Mammoth Lakes-04	SS	5.70	12.75	14.38	537	0.301	1.50
E04	265	Victoria-Mexico	SS	6.33	13.80	14.37	471	0.632	0.71
E05	459	Morgan Hill	SS	6.19	9.85	9.87	663	0.223	2.02
E06	587	New Zealand-02	N	6.60	16.09	16.09	551	0.241	1.87
E07	1111	Kobe, Japan	SS	6.90	7.08	7.08	609	0.464	0.97
E08	1135	Kozani, Greece-04	N	5.10	9.40	10.29	511	0.268	1.68
E09	1161	Kocaeli, Turkey	SS	7.51	7.57	10.92	792	0.261	1.72
E10	1618	Duzce, Turkey	SS	7.14	8.03	8.03	638	0.160	2.81
E11	1787	Hector, Mine	SS	7.13	10.35	11.66	726	0.328	1.37

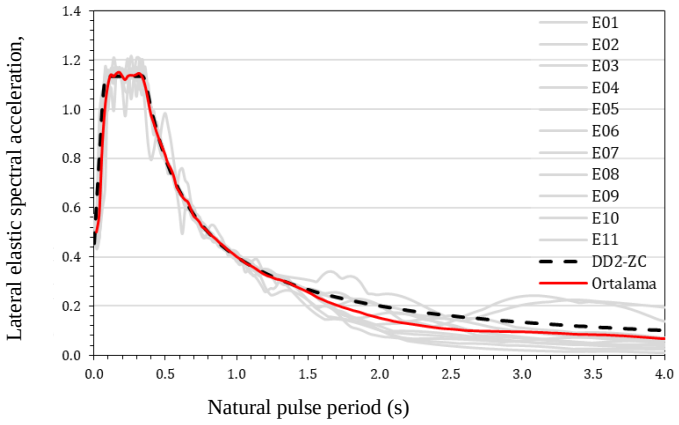

Figure 6. Parameters after matching the selected earthquake records (DD-2, Soil class: ZC)

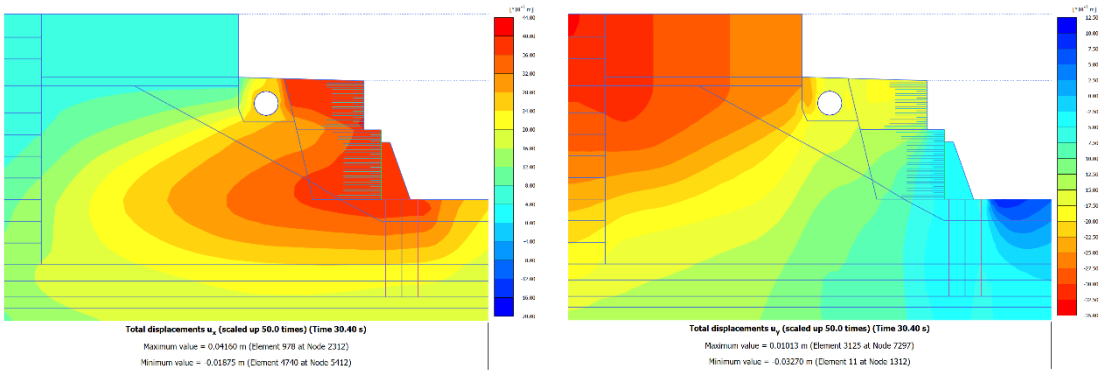

Figure 7. Lateral displacements (left), vertical displacements (right) for E01 earthquake

2.2 Three Dimensional Finite Element Analysis

Three dimensional (3D) finite elements analysis was carried out in order to take the lay-out of the piles and buttresses into account and to determine the performance of the retaining system. In 3D analysis, same soil parameters were used as used in 2D analysis. 2D and 3D analyses results both for static and pseudo-static loading conditions for DD-2 earthquake level were compared, and the accuracy of the approach was confirmed. 3D analysis results are given in Figures 8, 9 and 10.

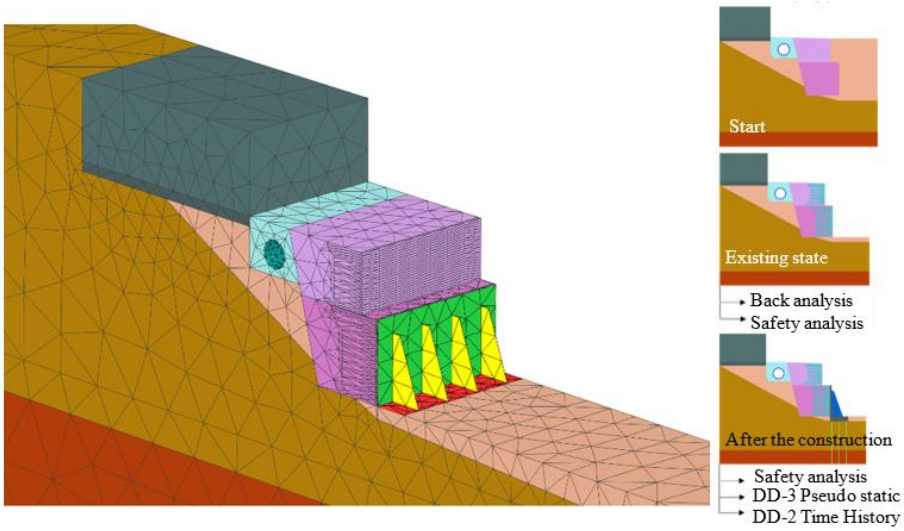

Figure 8. 3D analysis model (left), construction stages and analysis models (right)

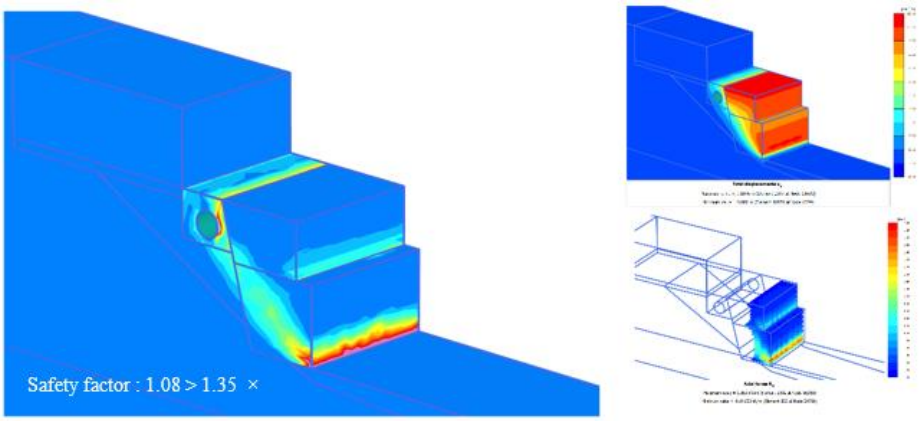

Figure 9. Safety analysis for initial phase (left), lateral displacements at the initial phase (right-top), axial forces on the geosynthetic reinforcements for the initial phase (right-down)

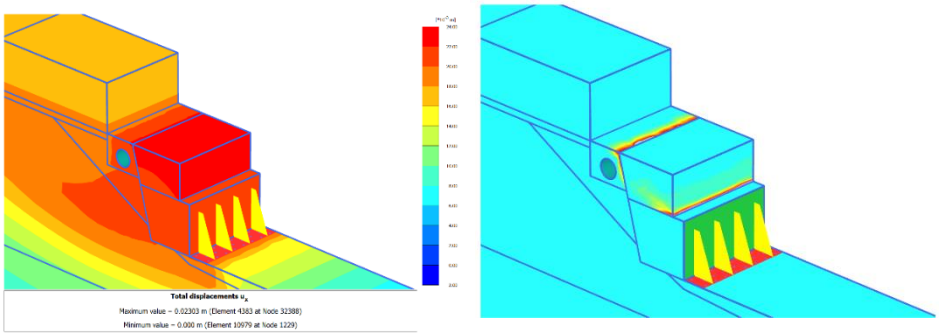

Figure 10. Lateral displacements after pseudo-static analyis for DD-3 earthquake level (left), safety analysis results for pseudo-static loading conditions for DD-3 earthquake level (right)

3. RESULTS AND DISCUSSION

After performing back analysis, it was determined that the real site conditions can be simulated by using finite elements analysis. In the analysis, 15 cm lateral displacement was calculated in the lower part of the geosynthetic reinforced wall and first four line of geosynthetic reinforcement in the lower part had reached their ultimate bearing capacity. The control of the design under the dynamic loading conditions has been provided by 2D time history analysis. Comparison of 2D and 3D analysis results are given in Table 3, and settlement values calculated from 2D time history analysis are given in Table 4. Maximum moments and forces at the piles are given in Table 5.

Table 3. Comparison of 2D and 3D analysis results

Analysis		Relative settlement in S5 block (mm)	Relative settlement in wall foundation (mm)	Maximum lateral displacement in top/bottom geowall (mm)	Maximum pile moment (kNm)	Safety factor
Back analysis	2D			135/125		1.03
	3D			105/103		1.08
Static analysis after the construction	2D					1.95
	3D					2.01
DD-3 pseudo-static	2D	1.4	0.0	10/8	180	1.37
	3D	4.3	0.0	23/21	179	1.48

Table 4. Settlements calculated by 2D time-history analysis

Record	S5 Block relative settlement (mm)	Relative settlement in wall foundation (mm)	Maximum lateral displacement in retaining wall (mm)	Maximum lateral displacement in top geowall (mm)
E01	6.4	1.56	39	41
E02	10.4	3.09	71	71
E03	13.7	3.28	73	77
E04	7.0	2.50	63	67
E05	10.3	1.78	46	48
E06	11.5	1.92	49	52
E07	8.4	3.57	75	79
E08	8.6	1.95	61	63
E09	6.1	1.44	42	45
E10	7.1	2.70	67	69
E11	7.8	4.20	87	89
Average	**8.85**	**2.54**	**61.2**	**63.7**

Table 5. Maximum moments and forces at the piles calculated by 2D time-history analysis for the selected earthquakes

Record	Moment (kNm)	Axial force (kN)	Shear force (kN)
E01	501	550	271
E02	484	565	253
E03	517	474	274
E04	516	556	256
E05	450	435	222
E06	472	675	240
E07	510	607	243
E08	474	585	241
E09	516	447	246
E10	502	552	261
E11	514	609	243
Average	**496**	**550**	**250**

As the results of the analysis, it was determined that, the differential settlements in the foundation of S5-Block and the related retaining wall did not exceed the acceptable limits in any loading conditions. In dynamic analysis, it was seen that, lateral displacements of the unsupported upper part of the geosynthetic wall and the new designed wall do not exceed the $80S_{DS}$ (mm) limit value as mentioned in TBEC-2018 [10]. Sufficient safety factors against failure were obtained both for static and dynamic loading conditions. On the other hand, after the construction of the new designed retaining wall, the unsupported upper part of the geosynthetic reinforced wall is prone to local collapse and its displacements must be monitored during its service time by providing drainage conditions.

4. CONCLUSIONS

In the presented study, the suitability of a new designed reinforced concrete retaining wall planned to be constructed in front of an existing building was examined. The new reinforced concrete retaining wall is going to be constructed for rehabilitation of an existing geosynthetic reinforced wall. Results of 2D and 3D analysis and geotechnical evaluations are summarized below:

- Settlement values of the foundation of existing building and foundation of the new designed retaining wall were calculated within the acceptable limits.
- Lateral displacements of the new designed retaining wall and the unsupported upper part of the geosynthetic reinforced wall did not exceed the limit values mentioned in TBEC-2018.
- After the construction of the new designed retaining wall, the unsupported upper part of the geosynthetic reinforced wall is prone to local collapse and its displacements must be monitored during its service time by providing drainage conditions.
- Considering the displacements of the existing retaining structure, it is seen that it is necessary to carry out the rehabilitation applications designed within the scope of the study.

REFERENCES

[1]. Duzgun M. (2001) Istinat duvarlari statik ve dinamik analiz: Depreme dayanikli betonarme istinat duvarlarinin tasarimi, DEU Muhendislik Fakultesi yayini, 290, Izmir, Turkey (in Turkish).
[2]. McCombie P.F., Mundell C., Heath A., Walker P. (2012) Drystone retaining walls: Ductile engineering structures with tensile strength, Engineering Structures, 45, 238-243.
[3]. Fukumoto Y., Yoshida J., Sakaguchi H., Murakami A. (2014) The effects of block shape on the seismic behavior of dry-stone masonry retaining walls: A numerical investigation by discrete element modeling Soils and Foundations 54, 6, 1117-1126.
[4]. Casolo S. (2000) Modelling the out-of-plane seismic behaviour of masonry walls by rigid elements, Earthquake Engineering & Structural Mechanics, 29, 12, 1797-1813.
[5]. Nimbalkar S., Choudhury D. (2007) Sliding stability and seismic design of retaining wall by pseudo-dynamic method for passive case Soil Dynamics and Earthquake Engineering, 27, 6, 497-505.
[6]. Villemus B., Morel J.C., Boutin C. (2007) Experimental assessment of dry stone retaining wall stability on a rigid foundation Engineering Structures, 29, 9, 2124-2132
[7]. Soil report (2020) Geoloji Muhendislik Co.

[8]. Cinicioglu O. (2020) Geotechnical Assessment Report
[9]. Tilki E. (2020) Retaining structure project
[10]. TBEC (2018). Turkey Building Earthquake Code: Rules for design of buildings under earthquake effect, Official Gazzette, 18.03.2018, 30364.
[11]. PEER Earthquake records, The Pacific Earthquake Engineering Research Center, "NGA-West2" (https://ngawest2.berkeley.edu/site).

ICENS 6TH INTERNATIONAL CONFERENCE ON ENGINEERING AND NATURAL SCIENCE
October 21-25 2020 Belgrade

Numerical approach for seismic assessment of an existing historical masonry school building

Baris Gunes[1], Baris Sayin[2]

Abstract

The study presents to determine the seismic performance of an existing hictorical masonry school building. Within the scope of the study, the C block of the building which consists of three blocks, was examined. In this scope, initially, field investigations including material and damage situations is performed regarding the examined building. After that, the mechanical properties of the masonry structural members are determined according to the relevant codes. The soil characteristics are obtained from the soil classification map prepared by the Istanbul Metropolitan Municipality, and seismic parameters are determined considering the location of the building and regional seismic risk map. In the next step, the structural model is prepared to represent the existing state of the structure by Midas Gen software, and the performance analysis is performed using the linear elastic analysis method. The response spectrum analysis method was chosen to consider the contributions of different modes. As a result of the school building being a historical structure, the seismic performance assessment was based on "Guidelines for the Management of Earthquake Risks in Historical Buildings of 2017". The importance level and performance target of the building was decided by the local administration. Earthquake loads are calculated according to Turkey Building Earthquake Code 2018 and was considered in the structural model. As a result of analysis, it is determined that the current status of C block not provided "Controlled Damage" performance level for DD-2 Earthquake Ground Motion Level for an earthquake with a 10% probability of exceedance in 50 years". The strength and displacements of the masonry walls in this block were obtained beyond the limit values given for the target performance level.

Keywords: Historical masonry school buildings, Seismic performance, Linear analysis

1. INTRODUCTION

Masonry structures have a wide range of uses. Many buildings have been built using the masonry system throughout history. In these buildings, masonry elements such as stone, brick, marble and adobe were used. It is very important to determine the structural safety of the historical masonry building stock against earthquakes and other effects. Repair and strengthening work is carried out in order to transfer the structures to future generations while preserving their structural integrity.

Numerical studies can be found in literature related to the determination of the seismic performance of existing masonry structures. Giordano et al. [1] investigated the applicability of various numerical techniques for the analysis of masonry structures and compared the calculated results with experimental test data obtained from a full-scale masonry sample. Using three different software, the effectiveness of different modeling techniques has been evaluated, and it has been proven which software gives more efficient and practical results. Betti and Vignoli [2] performed static and dynamic nonlinear analysis of historic masonry structures and determined the seismic performance of a basilica type church under earthquake load with finite element methodology. According to the analysis results, strengthening suggestions were given according to the possible damage in the building and these suggestions were compared with each other. Akoz [3] evaluated the repair and strengthening of historical masonry structures in the study. A three dimensional finite element model of a historic masonry structure was prepared and its static and dynamic analysis were made. After that, the

[1] *Istanbul University-Cerrahpasa, Department of Civil Engineering, 34320, Avcilar/Istanbul, Turkey.* bgunes@istanbul.edu.tr

[2] *Corresponding author, Istanbul University-Cerrahpasa, Department of Civil Engineering, 34320, Avcilar/Istanbul, Turkey.* barsayin@istanbul.edu.tr

earthquake safety level of the building has been determined and suggestions are given about the method of strengthening. Kara [4] investigated the behavior of masonry structures under horizontal and vertical loads. After discussing the types of damage seen in masonry structures and their causes, the experimental methods used in determining the damage are given. Strengthening methods are specified based on these damages. As an example, the strengthening approach according to the current state of five masonry structures was determined according to the 2007 earthquake code. Roca et al. [5] presented classical and advanced methods for examining historical masonry structures. In addition to the basic difficulties encountered in evaluating historical buildings, approaches to modeling and analyzing such structures are discussed. The applicability of current methods used in analysis, limit analysis, simplified methods, finite element method, macro / micro modeling and discrete element methods to structures are discussed. Suggestions are presented for an accurate analysis of complex historical masonry structures. Ercan [6] mentioned the studies on the existing historical masonry structures. The material properties of masonry structures are explained, and the methods used for modeling and the loads affecting the structure are specified. The methods used for the evaluation of historical masonry structures are explained in detail. Modal Analysis was performed in sample two masonry structures. Dynamic data obtained by experimental and numerical methods were compared. Static and dynamic analyzes of the buildings were made and the security level of the buildings was determined.

In this study, the seismic performance of an existing masonry building is assessment based on field studies and numerical analysis. The analyses are carried out based on the conditions about the seismic performance levels presented in Seismic Risks Management Guide for Historical Structures, SRMGHS-2017 [7] and Turkish Building Earthquake Code, TBEC-2018 [8].

2. THE EXAMINED BUILDING

In order to determine the current condition of the building, initially, field study was carried out. In Figure 1, the exterior view and aerial photograph of the building are given. The building is currently used as a school building. The building was built as a ground floor and first typical storey. The load-bearing system of the building was formed by masonry structural elements. During field investigations, non-structural cracks, swelling and spalling were observed in some of the masonry walls and floor coverings of the building. The building is 17.1 m. in x direction. and 5.2 m. to 6.2 m. in the y direction. long. The building area has approximately 101 m^2. The building has masonry walls with vertical discontinuity.

Figure 1. The aerial photo and overview of the building

3. SEISMIC VULNERABILITY ASSESSMENT METHODOLOGY

3.1. Modelling and Analysis Approach

The seismic performance of the structure examined within the scope of the study was determined by finite element analysis using the linear method. Finite element method is an effective analysis method used to determine the performance of masonry structures. Midas Gen software, which is a general purpose finite element software, was used in numerical analysis. In the finite element model, "plate" elements are used to model the masonry walls, and "frame" elements are used to model columns and beams. Pressure and shear stress on masonry walls were controlled by using the analysis model prepared to determine the performance level of the masonry structure and some additional calculation tools. In 3D finite element model prepared for this purpose, the critical section with door and window openings on each floor was determined, and the "Plate"

elements in this section were defined as "wall". As a result of the analyzes, the compressive and shear stresses on the wall were calculated based on the axial and shear forces provided on the walls in the critical section. Next, the compressive and shear stresses provided in the masonry walls were compared with the allowed stresses according to the masonry wall type. It was checked whether the obtained compressive and shear stresses exceed the limit stresses. The finite element analysis model of the structure and critical sections defined for masonry walls are shown in Figure 2.

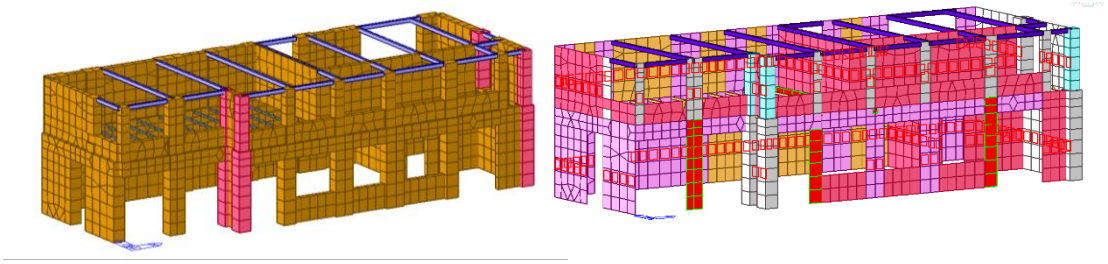

Figure 2. Three dimensional finite element model (left), The view of critical section in the model (right)

3.2. Seismic Assessment Criteria

In international literature and standards, there are many analysis methods and criteria for determining the earthquake performance of historical masonry structures. Seismic Risks Management Guide for Historical Structures, SRMGHS-2017 and Turkish Building Earthquake Code, TBEC-2018 are used together in determining the earthquake performance of historical buildings in Turkey. In TBEC-2018, there are some rules regarding the design of new buildings and evaluation of the earthquake safety of existing buildings. The rules given for wooden and masonry buildings in this regulation can also be used for historical buildings as a guide. However, some insolvencies arise based on the performance levels in TBEC 2018 for historical buildings. It is recommended to take TBEC-2018 as a basis for earthquake effects in SRMGHS-2017. However, special performance levels for historical buildings are defined in SRMGHS-2017. Therefore, TBEC-2018 is taken as basis in determining the earthquake loads affecting the historical building. SRMGHS-2017 is used to determine the performance criteria and level of the building.

SRMGHS-2017 [7] is used in the determination of the target performance level of the structure. In SRMGHS-2017, three earthquake ground motion levels (DD- 1, DD-2 and DD-3) are defined to evaluate the structural system safety of historic buildings. The return period of these earthquakes is defined as 2475, 475 and 72 years, respectively. In the same guide, three different structural performance levels (Limited Damage, Controlled Damage and Prevention of Collapse) are defined. “Limited Damage (LD)” performance level corresponds to the damage level where limited damages are allowed in the structural members (nonlinear behaviour is limited). “Controlled Damage (CD)” performance level corresponds to the state that mostly repairable damages are allowed in the structural members. “Prevention of Collapse (PC)” performance level corresponds to the state that high-level and excessive damages are allowed in the structural members, but the partial or total collapse is prevented (SRMGHS, 2017). For historic buildings, different building performance targets are anticipated for different earthquake levels in SRMGHS- 2017. Limit states of the target performance levels on the pushover curve defined in this guide is presented in Figure 3.

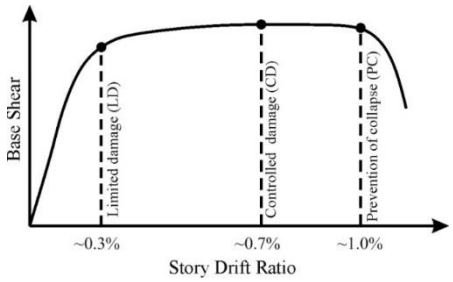

Figure 3. Pushover curve and limit states [7]

Building performance targets are classified in SRMGHS-2017 depending on the state of usage, importance and function of the building (Table 1). While the targeted vulnerability remains low for a worldwide and multi-

visitor heritage structure, relatively severe damage can be accepted for a locally important historic building that can only be visited from outside without entering it [7]. As can be seen, there are different performance targets for the historical building with the same importance class and the same earthquake level in Table 1. This is related to the level of performance demanded from the building. There are analysis methods and limit values that can be used for different performance levels in SRMGHS-2017, and the information are presented in Table 2.

Table 1. Building performance targets anticipated for different earthquake levels [7]

Buildings with local importance	Buildings with national importance	Buildings with global importance (heritage structures)
DD-3 (50/50%, 72 years) Controlled damage level (CD)	DD-3 (50/50%, 72 years) Limited damage level (LD)	DD-2 (50/10%, 475 years) Limited damage level (LD)
DD-3 (50/50%, 72 years) Prevention of collapse damage level (PC)	DD-2 (50/10%, 475 years) Controlled damage level (CD)	DD-1 (50/2%, 2475 years) Limited damage level (LD)
DD-2 (50/10%, 475 years) Prevention of collapse damage level (PC)	DD-1 (50/2%, 2475 year) Prevention of collapse damage level (PC)	DD-1 (50/2%, 2475 years) Controlled damage level (CD)

Table 2. Analysis methods and provisions for performance levels [7]

Performance level	Analysis method	Limit / Provision
Limited damage	Linear	Obtained results under vertical loads + unreduced seismic loads (Ra=1) do not exceed material strength values. Obtained storey drift ratios under unreduced seismic loads do not exceed 0.3% limit.
Controlled damage	Linear	Obtained results under vertical loads + reduced seismic loads (Ra≤3) do not exceed material strength values. Obtained storey drift ratios under unreduced seismic loads do not exceed 0.7% limit.
	Nonlinear	Obtained results under vertical loads + reduced seismic loads (Ra≤3) do not exceed material strength values. Obtained storey drift ratios under unreduced seismic loads do not exceed 0.7% limit.
Prevention of collapse	Linear	Obtained results under vertical loads + reduced seismic loads (Ra≤3) can exceed material strength values with a permissible ratio (~1.5 times). Obtained storey drift ratios under unreduced seismic loads do not exceed 1% limit.
	Nonlinear	Obtained storey drift ratios do not exceed 1% limit. Strain capacities of materials can be exceeded with a permissible ratio (~1.2 times).

3.3. Analysis Parameters

In Table 3, performance analysis parameters of the building are given according to SRMGHS-2017. Linear Analysis method was used in the performance analysis of the structure. Response Spectrum Analysis, which takes the contributions of different modes into consideration, is used in this method. The earthquake load reduction coefficient Ra determined according to SRMGHS-2017 was used in the acceleration spectrum. In accordance with Article 4.8.4 of TBEC-2018, the condition that the earthquake forces calculated with the relevant method are equal to or greater than 80% of the forces calculated by the equivalent earthquake load method.

Table 3. Performance analysis parameters

Parameter	Value / Class
Building importance factor	I=1
Ground motion level and performance target	Controlled damage for DD-2
Performance analysis method	Linear
Storey drift limit value	0.7% Controlled damage
Building information level and coefficient	Limited, 0.75
Seismic load reduction coefficient, Ra	Ra=3 for DD-2

3.4. Soil and earthquake parameters

The parameters was determined, considering the soil report [10] and Turkey Earthquake Hazard Maps Interactive Web Applications [11]. In accordance with TBEC-2018, lateral elastic acceleration spectrum corner periods (T_A and T_B) and spectrum curve were prepared by using soil and earthquake parameters. The ground class to be used in the analysis has been determined as "ZC" depending on the location of the building. In Table 4, soil and earthquake parameters determined based on the issues in TBEC-2018 are presented.

Table 4. Soil and earthquake parameters

Parameters	Value / Class
Local soil class	ZC
Earthquake ground motion level	DD-2
Spectral acceleration coefficients	DD-2, S_s = 0.886, S_1 = 0.247
found from the earthquake	DD-2, PGA = 0.364
Local soil impact coefficients	DD-2, Fs = 1.200, F_1 = 1.500
Spectral acceleration coefficients	DD-2, S_{DS} = 1.063, S_{D1} = 0.370

3.5. Materials

In Table 5, the mechanical properties of masonry walls determined on the basis of Seismic Risks Management Guide for Historical Structures (SRMGHS 2017) are given. The type and application method of masonry walls were determined by performing observational examinations on site. The masonry unit type of the masonry bearing elements in the structure was determined as solid block brick with lime mortar.

Table 5. Mechanical properties of the masonry walls

Definition	Abbreviation	Value / Class
Masonry unit	-	Solid block
Masonry unit group	-	Group I
Density, kN/m^3	-	18
Unit compressive strength, MPa	f_b	5.0
Mortar compressive strength, MPa	f_m	2.5
Characteristic compressive strength of wall, MPa	f_k	2.30
Initial shear strength of wall, MPa	f_{vk0}	0.15
Tensile strength of wall, MPa	f_t	0.225
Young modulus of wall, MPa	E_{wall}	2100
Shear modulus of wall, MPa	G_{wall}	350

4. RESULTS

Performance analysis was performed for the "Controlled Damage" performance target for DD-2 earthquake ground motion level based on SRMGHS-2017. In Figure 4, lateral displacements provided under x and y direction earthquakes in addition to vertical loads for earthquakes (DD-2 earthquake ground motion level) with a probability of exceeding 10% in 50 years are shown. In Table 6, relative storey drifts and target performance limit values are compared. As can be seen, for the ground motion level DD-2, the relative storey drifts provided in the current state of the building do not meet the "Controlled Damage" performance target.

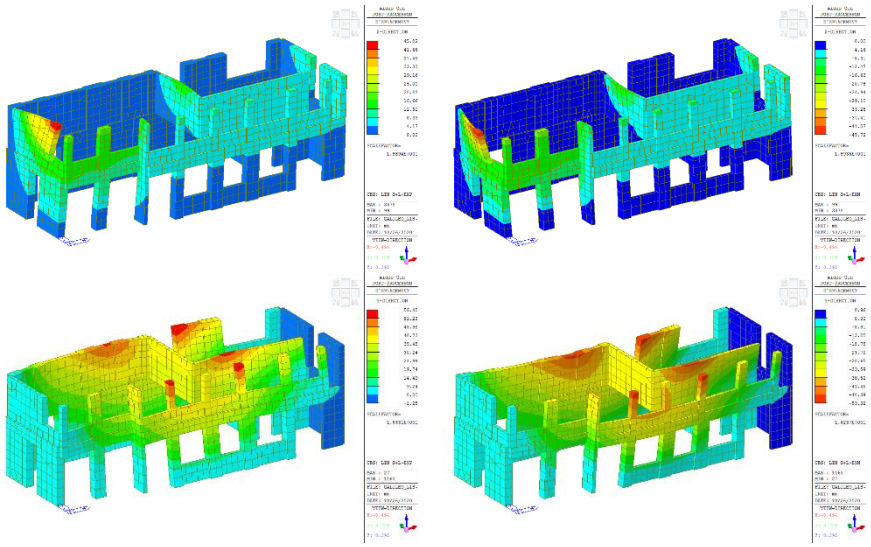

Figure 4. Lateral displacements under the earthquake effects. Direction x (up), Direction y (down)(DD-2, Ra=1)

Table 6. The checking of relative storey drift ratio (DD-2, Ra=1)

Storey	Displacement (mm)		Storey drift		Limit value	Result
	x	y	%	%	%	√ / ×
Ground	13.89	36.62	0.41	1.09	0.7 (CD)	×
First	29.59	20.62	1.29	0.90	0.7 (CD)	×

In Figure 5, in addition to the vertical loads for earthquakes (DD-2 earthquake ground motion level) with a probability of exceeding 10% in 50 years, shear forces provided under x and y-direction earthquakes are shown. Table 7 shows the ratio of shear force acting on masonry structural elements, which cannot meet the shear forces provided under the effects of earthquakes in x- and y-directions, to the storey shear force. As can be seen, the shear forces do not meet the "Controlled Damage" performance target for the DD-2 earthquake ground motion level.

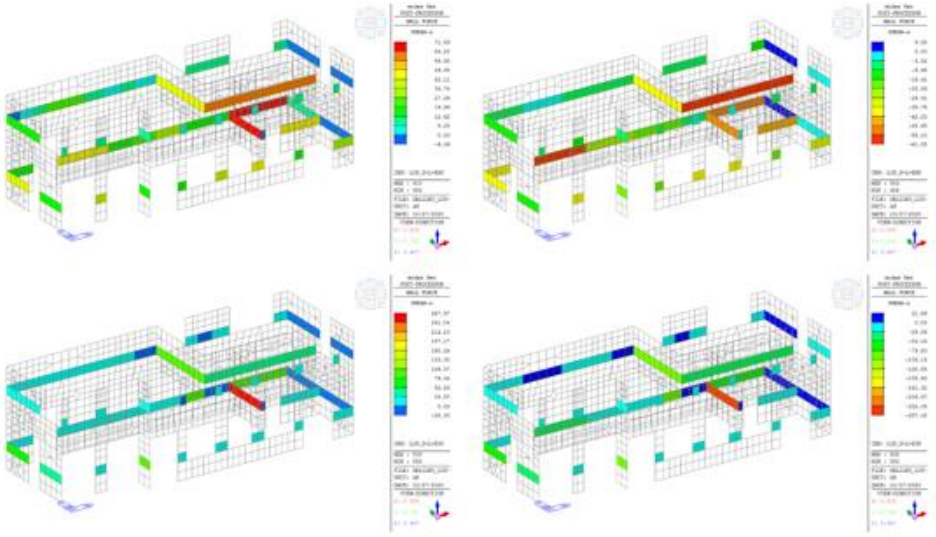

Figure 5. Shear forces under the earthquake effects. Direction x (up), Direction y (down)(DD-2, Ra=3)

Table 7. Performance assessment results (DD-2, Ra=3)

Storey	Vertical load-bearing members (Walls, columns) Checking of storey shear force (Ra=3) Masonry SRMGHS-2017	*% r	Target performance level (CD)
Ground	√	56.96	×
First	√	0.00	√

* The ratio of the total shear force of the walls that cannot meet the shear force caused by the earthquake to the floor shear force

5. CONCLUSIONS

The seismic performance of the structure was examined in the study. The structure was modeled in a finite element program to represent the current situation and performance analyzes were carried out within the framework of the criteria determined in SRMGHS-2017. In DD-2 Earthquake, the results obtained from the analysis and evaluations for the "Controlled Damage" performance target are summarized below.

The axial forces provided in the vertical bearing elements of the structure are below the axial force capacity of the elements. Strength level of the structure is sufficient in terms of vertical loads.

The ratio of the total shear force acting on the vertical bearing elements, which cannot meet the shear forces occurring under the effect of vertical and earthquake loads to the shear force is above the limit value.

The relative storey drifts provided in the structure are above the allowed limit for the target performance level.

In conclusion, structure's seismic performance against DD-2 earthquake (10% probability of being exceeded in 50 years/return period 475 years) is not assessed for the "Controlled Damage" performance level.

REFERENCES

[1]. Giordano A., Mele E., De Luca A. (2002) Modelling of historical masonry structures: comparison of different approaches through a case study, Engineering Structures, 24(8), pp. 1057–1069.
[2]. Betti M., Vignoli A. (2008) Assessment of seismic resistance of a basilica-type church under earthquake loading: Modelling and analysis', Advances in Engineering Software, 39(4), pp. 258–283. doi: 10.1016/j.advengsoft.2007.01.004.
[3]. Akoz H. (2008) Deprem Etkisi Altindaki Yigma yapilarin Onarim ve Guclendirilmesi, Yuksek Lisans Tezi, Istanbul Teknik Universitesi, Fen Bilimleri Enstitusu.
[4]. Kara H.G. (2009) Yigma yapilarin Tasiyici Sistemleri, Guvenliginin Incelenmesi, Onarimi ve Guclendirmesi. Yuksek Lisans Tezi, Istanbul Teknik Universitesi, Fen Bilimleri Enstitusu.
[5]. Roca P. Cervera M., Gariup G., Pela' L. (2010) Structural analysis of masonry historical constructions. Classical and advanced approaches, Archives of Computational Methods in Engineering, 17(3), 299–325.
[6]. Ercan E. (2010) Yigma yapilarin Guvenliklerinin Analitik ve Deneysel Yontemlerle Belirlenmesi. PhD thesis, Science Institute, Ege University doi: 10.1007/s11831-010-9046-1.
[7]. SRMGHS. (2017). Seismic Risks Management Guide for Historical Structures. General Directorate of Foundations, Ankara.
[8]. TBEC (2018) Turkey Building Earthquake Code: Rules for design of buildings under earthquake effect, Official Gazzette, 18.03.2018, 30364.

ICENS 6TH INTERNATIONAL CONFERENCE ON ENGINEERING AND NATURAL SCIENCE
October 21-25 2020 Belgrade

Seismic assessment of existing low-rise RC buildings: A Case study

Baris Gunes [1], Baris Sayin [2*]

Abstract

Modern and safe structures can be built depending on the developing materials and construction technologies. However, this is not possible for existing structures. Considering the losses occurring in time due to different reasons in the construction quality and material strength of the existing buildings during the construction period, it is necessary to determine the structural safety of these structures. This situation becomes even more critical, especially in areas prone to earthquake risk. It is a necessity to determine the earthquake safety of the existing structures in these areas with advanced analysis methods and to take the necessary repair / strengthening measures. The presented study covers the determination of the earthquake performance of an existing RC structure built as a residential building with advanced analysis methods based on the current regulations. In this scope, firstly, the existing building's structural system, geometry, layout and material properties were determined by site surveys and lab studies to evaluate its seismic performance level. Secondly, the building was modelled by Midas Gen finite element software. In the analysis model, fiber hinges were assigned to the columns, and lumped hinges were assigned to the beams. In the last stage, the numerical simulations of the building is performed by modal analysis and pushover analysis to determine the seismic performance levels of before- and after- the excavation according to the current Turkish Building Earthquake Code (TBEC 2018). The maximum and minimum strain values formed in the column and beam cross-sections were calculated by the curvature values obtained from the related members' assigned hinges. It is concluded that the case study will present an approach for the determination of the seismic performance of existing RC buildings.

Keywords: RC buildings, Seismic Performance, TBEC 2018

1. INTRODUCTION

Buildings constructed with reinforced concrete structural system constitute an important part of the existing buildings. It is a known fact that a meaningful part of the existing RC buildings in Turkey do not receive sufficient engineering services and do not have the necessary material strength. Therefore, it is necessary to first determine the seismic performance of the existing buildings, and then apply repair / strengthening or reconstruction options.

A number of researches have been conducted on studied the seismic performance of existing RC buildings. Sobaih and Nazif [1] specified an essential step for the required strategy to evaluate the seismic performance of existing RC buildings on the national level. Mosleh et al. [2] investigated the application and methodology for the seismic assessment of existing two buildings. The seismic capacity was determined for the earthquakes with different return periods, and the seismic demands. Cherifi et al. [3] estimated the seismic strength level of the existing buildings. To this end, capacity curves are obtained for the RC buildings using the pushover method. Halder and Paul [4] researched the seismic performance of a low-rise RC building. Chaulagain et al. [5] studied the performance of an existing building. with four different three-story RC building. A pushover and a nonlinear dynamic time history analyses were also performed. Wahyuni [6] studied the evaluation of of

[1] *Istanbul University-Cerrahpasa, Department of Civil Engineering, Structural Division, 34320, Avcilar/Istanbul, Turkey. bgunes@istanbul.edu.tr*

[2*] *Corresponding author, Istanbul University-Cerrahpasa, Department of Civil Engineering, Structural Division, 34320, Avcilar/Istanbul, Turkey. barsayin@istanbul.edu.tr*

RC buildings subjected to seismic effects. The study was conducted based on a case study using numerical approach. Melani et al. [7] presented the seismic assessment of low-rise RC buildings. Three frames were analysed with capacity design approach.

In this study, the seismic performance of an existing RC building is assessment based on field studies, laboratory tests and numerical analysis. Analyses of finite element model of the examined building are done with Midas Gen software [8]. Performance analyses are performed based on Turkish Building Earthquake Code, TBEC-2018 [9].

2. THE EXAMINED BUILDING

Field investigations were initially conducted to determine the seismic performance of the building. Front views of the building are given in Figure 1. The building consists of two basement storey, ground storey, 3 typical storey and an attic. The building is 13.8 m. long in the x-direction and 10.5 m. in the y-direction. During the studies, it was determined that there were non-structural cracks in some wall surfaces of the building. In addition, humidity, swelling and spillage were determined on the walls and columns.

Figure 1. Facade views of building

3. SEISMIC VULNERABILITY ASSESSMENT METHODOLOGY

3.1 Laboratory

Concrete compressive strength was determined in accordance with the principles stated in Turkish Building Earthquake Code, TBEC-2018 [9]. To determine the concrete compressive strength, concrete samples were taken from a total of 18 vertical load-bearing elements [10]. In the calculations made using concrete compressive strength data, the compressive strength of unconfined concrete was determined as 14.08 N/mm2. Table 1 shows the values obtained based on the test results.

Table 1. The evaluation of concrete compressive strength

$f_{c,cube,av.}$	$^{*}\sigma$	$f_{c,cube} = f_{c,cube,av} - \sigma$	$f_{c,cyl} = 0.85 \cdot f_{c,cube}$	$f_{c,cyl,nc} = 0.85 \cdot f_{c,cube,nc}$
19.48	5.34	14.14	16.56	14.08

* All units*: MPa,* σ: *standard deviation, nc: non-confined*

With regard to the determination of rebar, the study has been carried out in line with the principles specified in TBEC-2018. There are two different methods in the code in order to determine the rebars of the load-bearing members in the building. The first method is the undamaged reinforcement detection method. The second method is the observational reinforcement detection method by stripping the cover. The undamaged rebar method was made with a PS200S ferroscan. The rebar determination process was performed from 18 vertical load-bearing elements. Accordingly, it was observed that 10Ø16 longitudinal rebar and Ø10/20 stirrup were used in a column. In the second method, visual rebar checks are made by removing the cover of the load-bearing elements. Cover stripping process was performed from two vertical bearing elements from the second basement floor of the building. At the end of the stripping process, longitudinal rebars of Ø16 and stirrups of Ø8/20 were determined on the columns. In addition, it has been stated that there is corrosion in the rebars of the load-bearing elements stripped of the cover. As a result of the determination of undamaged and damaged methods, it has been determined that longitudinal rebars and stirrups used in columns and shear walls are non-ribbed rebar

(S220) [14]. It has been determined that longitudinal rebars of Ø16 and stirrups of Ø8/20 and Ø10/20 are used in columns and curtains.

3.2 Soil and Seismic Properties

Ground and earthquake parameters used in static analysis are defined in Table 2. Soil parameters to be used in the analysis are determined [11]. The parameters obtained were checked by comparing them with the "Vs (0-30 m) Average Shear Wave Velocity Map" [12].

Table 2. The characteristic properties of the soil

Parameter	Soil Layer
Soil class *	ZC
Modulus of subgrade reaction (vertical) (kN/m^3)	25000
Allowable bearing value, σ_z (kg/cm^2)	1.60
* According to TBEC-2018 [9]	

Four different ground motion levels have been defined in TBEC-2018. The levels were used for performance targets. Elastic acceleration spectrum characteristic values have been selected according to the soil class. According to the values, the spectrum curve was drawn depending on the local soil impact coefficients given in TBEC 2018. Earthquake map spectral acceleration coefficient (S_s and S_1) is determined based on Turkey Earthquake Hazard Maps [13]. The location of the building is marked on the map and it is designated as S_s and S_1 for an earthquake with a return period of 475 years. Subsequently, the local soil impact coefficients (F_s and F_1) were calculated based on the determined spectral acceleration coefficients and local soil class information. Spectral acceleration coefficients are obtained by multiplying the map spectral acceleration coefficients with the local ground effect coefficients as described in TBEC 2018 using the following equations:

$$S_{DS} = S_S\, F_S = 1.318 \times 1.20 = 1.58$$
$$S_{D1} = S_1\, F_1 = 0.356 \times 1.50 = 0.53 \quad (1)$$

Accordingly, the lateral elastic spectral acceleration values [S_{ae} (T)] and the horizontal elastic acceleration spectrum corner periods (T_A and T_B) were calculated based on the above calculated values and the criteria given in the regulation (Figure 2) and the lateral elastic acceleration spectrum was formed.

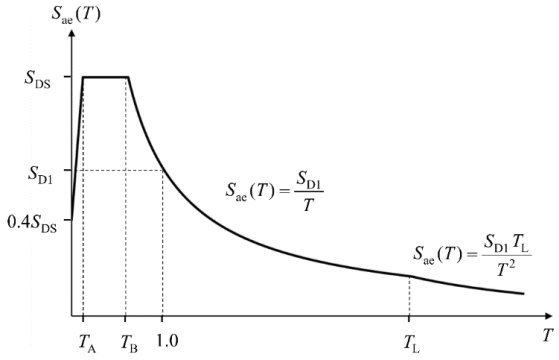

Figure 2. Criteria presented for the calculation of spectral acceleration values and elastic spectrum in the code

3.3 Seismic Assessment Criteria

The performance analysis of the building is carried out considering the criteria presented in TBEC (2018). The section damage limits and regions used in the strain-based evaluation defined in the code are given in Figure 3. Three damage levels and limits are defined for the ductile members. These are Limited Damage (SH), Controlled Damage (CD) and Pre-Collapse Damage (PC) levels and their limits. Limited Damage Level corresponds to a limited plastic behaviour of a section. Controlled Damage Level corresponds to a permissible plastic behaviour of a section. Pre-Collapse Damage Level corresponds to a high-level plastic behaviour of a section. This approach is not valid for the brittle members. The structural members whose critical sections' damage level does not reach LD are assumed to be in the Limited Damage (LD) Region. The structural members

whose critical sections' damage level is between LD and CD are assumed to be in the Significant Damage (SD) Region. The structural members whose critical sections' damage level is between CD and PC are assumed to be in the Advanced Damage (AD) Region. The structural members whose critical sections' damage level reaches PC are assumed to be in the Collapse (CR) Region. Effective stiffnesses of the cracked sections are used on the reinforced concrete members with distributed plastic hinges under bending effects.

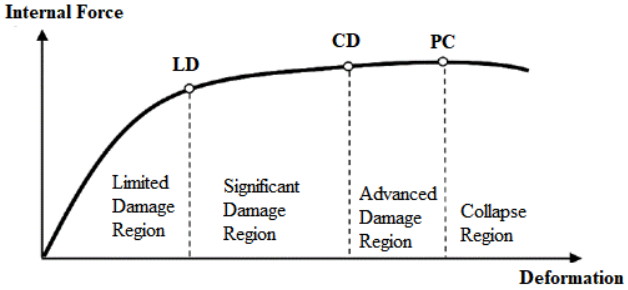

Figure 3. Section damage regions [9]

The performance level of the reinforced concrete buildings is determined according to the criteria presented by Sect. 15.8.4. The related criteria are summarized below;

Buildings that meet the following conditions are considered to ensure the Controlled Damage (CD) Performance Level provided that the brittle damaged elements are strengthened, if any:

(a) Maximum 35% of beams (except for secondary beams that are not part of the main structural system) and vertical structural members that are defined in item (b) below on any floor could be in Advanced Damage (AD) Region under the applied seismic effects of one direction.
(b) The total contribution of the vertical structural members in the Advanced Damage (AD) Region to the total story shear on each floor must be below 20%. This limit could be increased to 40% at the top floor.
(c) Rest of the structural members must be in the Limited Damage (LD) or Significant Damage (SD) Regions. However, if both of top and bottom sections of the vertical members exceed significant damage (SD) limit, the ratio of total shear forces carried by these members to the total story shear on any floor should not exceed 30%.

3.4 Modelling and Analysis Approach

The examined building was modeled by the finite element software and seismic performance analysis of the building was performed. Three dimensional static analysis model of the building is given in Figure 4. In the analyses, distributed (fiber) plastic hinges are assigned to the all structural members. The material strength values are not reduced by material coefficients, and the capacity of structural members are calculated by the actual material strength values. (TBEC 2018, Section 15.2.12-b). The building information level is assumed as "limited information level". Accordingly, the building information level coefficient is considered as "0.75" in the calculations. In order to determine the performance level of the building, nonlinear static pushover analysis method presented in Section 15.6 of TBEC (2018) is selected. In line with the selected method (nonlinear static pushover analysis method), the seismic load reduction factor [Ra(T)] is not applied to the design response spectrum, and the structural system behaviour and overstrength factors (R and D) are not used. The performance analysis of the examined building considering its purpose of use has been performed according to the Section 15 of Turkish Building Earthquake Code which was published by Disaster and Emergency Management Presidency on 19.03.2018 (30364 numbered official journal). The building must meet the "Controlled Damage Performance Target" conditions against the earthquake (earthquake ground motion level: DD-2) having 10% probability of exceedance in 50 years (475 years return period). The evaluation approach is determined as the strain-based evaluation/design. The damage assessment of the structural members is done considering the criteria presented in Section 15.8.4 of TBEC 2018 in order to ensure controlled damage performance level in existing buildings.

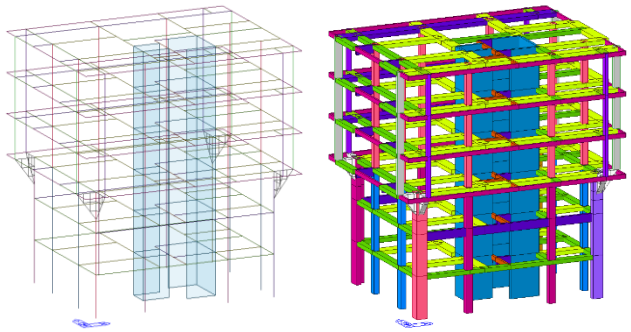

Figure 4. Three dimensional finite element model

4. RESULTS

Base shear - top displacement and demand spectrum - capacity diagrams for the earthquake (DD-2 ground motion level) with a probability of exceeding 10% in 50 years obtained as a result of the analysis are presented in Figure 5.

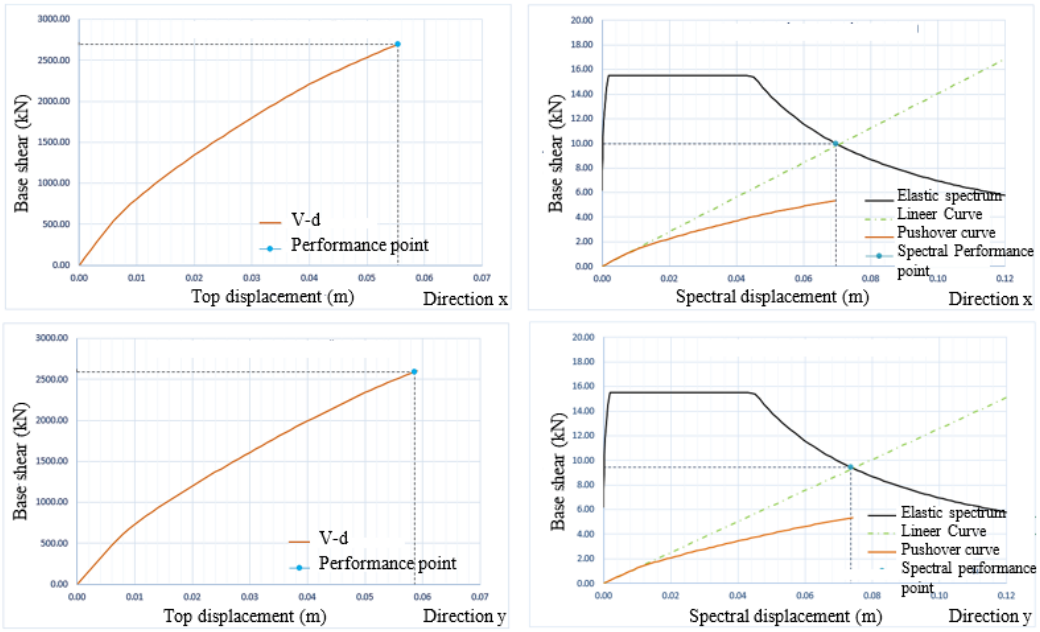

Figure 5. Base shear-top displacement and demand-capacity relationships. Direction-x (top), Direction-y (down)

The lateral displacements of the building at performance points under the effects of earthquakes are shown in Figure 6. At the performance point of the building, the deformations provided in the fibers of the column sections numbered 423 and 419 are given in Figure 7 as an example. The results obtained from the analysis for all storeys and the performance evaluations of the building are given in Tables 3 and 4 for vertical and lateral load-bearing elements, respectively.

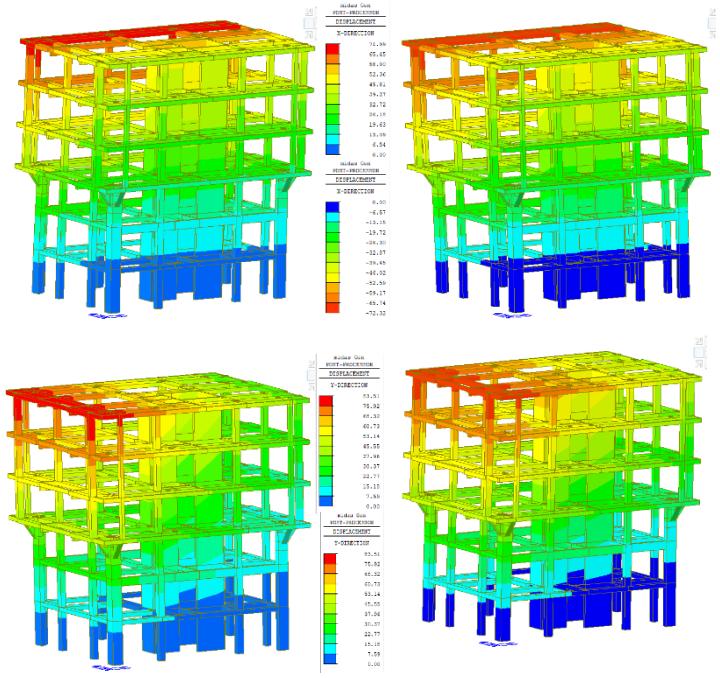

Figure 6. Lateral displacements under the earthquake loading. Direction-x (up), Direction-y (down)

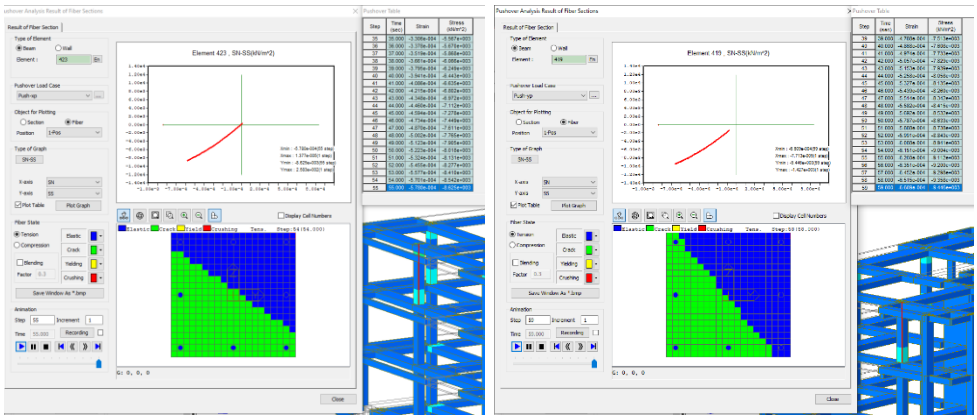

Figure 7. Deformations in the fibers of two column sections at the performance point

Table 3. Performance assessment results for column and walls

Storey	Strain check		Brittle failure check	Target Performance Level (Controlled Damage, KH)
	RC	RC	RC	
B2	×	√	×	×
B1	√	√	×	×
Ground	√	√	×	×
First	√	√	×	×
Second	√	√	√	√
Third	√	√	√	√

Table 4. Performance assessment results for beams

Storey	Strain check	Brittle failure check	Target Performance Level (Controlled Damage, KH)
	RC	RC	
B2	√	×	×
B1	√	×	×
Ground	√	×	×
First	√	×	×
Second	√	×	×
Third	√	×	×

5. CONCLUSIONS

In this study, an existing RC building was analyzed based on the criteria determined in TBEC-2018 and the seismic performance of the building was determined. The results obtained from the analysis and evaluations are summarized below.

The building fulfills the condition specified in Article 15.8.4 (a) of TBEC-2018 for "Controlled Damage" performance level. RC main beams in the building are in the "Limited Damage", "Significant Damage" or "Advanced Damage" zone. The ratio of reinforced concrete main beams in the "Advanced Damage" zone is below the limit value. There is no reinforced concrete main beam in the "collapse" zone.

The building does not meet the condition specified in Article 15.8.4 (b) of TBEC-2018 for "Controlled Damage" performance level. The reinforced concrete vertical bearing elements in the building are in the "Limited Damage", "Significant Damage" or "Advanced Damage" zone. The total contribution of the reinforced concrete vertical bearing elements in the "Advanced Damage" zone to the shear force carried by the vertical bearing elements at that storey is above the limit value. There is no reinforced concrete vertical load-bearing element in the "collapse" zone.

The building fulfills the condition specified in Article 15.8.4 (c) of TBEC-2018 for "Controlled Damage" performance level. In the building, there are no reinforced concrete vertical bearing elements whose "Distinct Damage Limit" is exceeded in both the upper and lower sections.

The building does not meet the friability condition specified in Article 15.8.4 of TBEC-2018 for the "Controlled Damage" performance level. The building consists of reinforced concrete elements damaged as "brittle".

Consequently, the building does not provide the "Controlled Damage" performance level for an earthquake (DD-2 Earthquake Ground Motion Level) with a probability of exceedance of 10% (recurrence period 475 years) in 50 years specified in TBEC-2018.

REFERENCES

[1]. Sobaih M.E., Nazif M.A. (2012) A proposed methodology for seismic risk evaluation of existing reinforced school buildings. HBRC Journal, 8(3), 204-11.
[2]. Mosleh A., Rodrigues H., Varum H., Costa A., Arede A. (2016) Seismic behavior of RC building structures designed according to current codes. Structures, 7, 1-13.
[3]. Cherifi F., Farsi M-N., Kaci S., Belaidi O., Taouchei-Kheloui F. (2015) Seismic Vulnerability of Reinforced Concrete Structures in Tizi-Ouzou City (Algeria), Procedia Engineering, 114, 838-45.
[4]. Halder L., Paul S. (2016) Seismic damage evaluation of gravity load designed low rise RC building using nonlinear static method, Procedia Engineering, 144, 1373-80.
[5]. Chaulagain H., Rodrigues H., Jara J., Spacone E., Varum H. (2013). Seismic response of current RC buildings in Nepal: A comparative analysis of different design/construction, Engineering Structures, 49, 284-94.
[6]. Wahyuni E. (2015) Seismic vulnerability evaluation of existing R.C. buildings. Procedia Earth and Planetary Science, 14, 76-82.
[7]. Melani A., Khare R.K., Dhakal R.P., Mander J.B. (2016) Seismic risk assessment of low rise RC frame structure, Structures, 5, 13-22.
[8]. Midas Gen (2018) Integrated Solution System for Building and General Structures," in MIDAS Information Technology Co.

[9]. TBEC (2018) Turkey Building Earthquake Code: Rules for design of buildings under earthquake effect, Official Gazzette, 18.03.2018, 30364.
[10]. Technical Report (2019) Concrete and rebar test, Report no. KR1900/10, Bensu laboratory Co.
[11]. Soil Report (2019) Esta Zemin Sondaj Insaat Muhendislik Mimarlik Co.
[12]. IBB (2009) Soil Classification Map: Istanbul Metropolitan Municipality Istanbul European Side Micro-Zoning Study [Online] Available at:ibb.gov.tr/trTR/SubSites/DepremSite/PublishingImages/2009.11.11.01.Avs30 Map_A3_150000 .pdf.
[13]. AFAD Turkey Earthquake Risk Map Interactive Web Application. [Online] Available at: https://tdth.afad.gov.tr/ TDTH/main.xhtml, 2019.
[14]. TS708 (2010) Celik ve Betonarme Icin Donati Celigi. Turk Standardlari Enstitusu, Ankara.

ICENS

6TH INTERNATIONAL CONFERENCE ON ENGINEERING AND NATURAL SCIENCES

www.icens.eu